Metal-optic and Plasmonic Semiconductor-based Nanolasers

Amit Lakhani
Ming C. Wu, Ed.
Xiang Zhang, Ed.
Eli Yablonovitch, Ed.

Electrical Engineering and Computer Sciences
University of California at Berkeley

May 7, 2012

Metal-optic and Plasmonic Semiconductor-based Nanolasers

by

Amit Manmohan Lakhani

A dissertation submitted in partial satisfaction
of the requirements for the degree of

Doctor of Philosophy

in

Engineering - Electrical Engineeing and Computer Sciences

in the

Graduate Division

of the

University of California, Berkeley

Committee in charge:

Professor Ming C. Wu, Chair
Professor Xiang Zhang
Professor Eli Yablonovitch

Spring 2012

Metal-optic and Plasmonic Semiconductor-based Nanolasers

Abstract

Metal-optic and Plasmonic Semiconductor-based Nanolasers

by

Amit Manmohan Lakhani

Doctor of Philosophy in Engineering - Electrical Engineeing and Computer Sciences

University of California, Berkeley

Professor Ming C. Wu, Chair

Over the past few decades, semiconductor lasers have relentlessly followed the path towards miniaturization. Smaller lasers are more energy efficient, are cheaper to make, and open up new applications in sensing and displays, among many other things. Yet, up until recently, there was a fundamental problem with making lasers smaller: purely semiconductor lasers couldn't be made smaller than the diffraction limit of light.

In recent years, however, metal-based lasers have been demonstrated in the nanoscale that have shattered the diffraction limit. As optical materials, metals can be used to either reflect light (metal-optics) or convert light to electrical currents (plasmonics). In both cases, metals have provided ways to squeeze light beyond the diffraction limit. In this dissertation, I experimentally demonstrated one nanolaser based on plasmonic transduction and another laser based on metal-optic reflection.

To create coherent plasmons, I designed a nanolaser based on a plasmonic bandgap defect state inside a surface plasmonic crystal. In a one-dimensional periodic semiconductor beam, I was able to confine surface plasmons by interrupting the periodicity of the crystal. These confined surface plasmons then underwent laser oscillations in effective mode volumes as small as 0.007 cubic wavelengths. At this electromagnetic volume, energy was squeezed 10 times smaller than those possible in similar photonic crystals that do not utilize metal. This demonstration should pave the way for achieving engineered nanolasers with deep-subwavelength mode volumes and enable plasmonic crystals to become attractive platforms for designing plasmons.

After achieving large reductions in electromagnetic mode volumes, I switched to a metal-optics-based nanolaser design to further reduce the physical volumes of small light sources. The semiconductor nanopatch laser achieved laser oscillations with subwavelength-scale physical dimensions (0.019 cubic wavelengths) and effective mode volumes (0.0017 cubic wavelengths). The ultra-small laser volume is achieved with the presence of nanoscale metal patches which suppress electromagnetic radiation into free-space and convert a leaky cavity into a highly-confined subwavelength optical resonator. The nanopatch laser, with its world-

1

record-breaking small physical volume, has exciting implications for data storage, biological sensing, on-chip optical communication, and beyond.

To my parents, who sacrificed much to get me here...

Contents

List of Figures

xi

xiii

List of Tables

Acknowledgements

I would like to thank my advisor, Prof. Ming Wu, for all of his support and encouragement throughout my graduate school career. It is truly remarkable that he was able to sense when I was struggling and help me along, and it is equally remarkable that he knew when to cut me loose and let me use my own creativity and confidence to solve challenging problems. He has truly set an example for me to become an effective and caring leader.

I also want to thank Prof. Kyoungsik Yu, Dr. Erwin Lau, and Dr. Myung-Ki Kim for working with me on the many different papers that we published together. I could not have asked for better people to work with. I would like to give a special thanks to Prof. Eli Yablonivitch, Prof. Ivan Kaminow, and Prof. Xiang Zhang for being on my qualifying exam and dissertation committees. Their work has inspired me to dream big and never give up. I also want to thank everyone in our group who have become my friends and helped me to learn all of skills I have today: Prof. Aaron Ohta, Dr. Steven Neale, Dr. Ming-chun (Jason) Tien, Dr. Arash Jamshidi, Dr. Justin Valley, Hsan-yin (Tony) Hsu, Tae Joon Seok, John Wyrwas, Karen Grutter, Anthony Yeh, Shao Ning Pei, Michael Eggleston, Alex Grine, Ryan Going, Dr. Niels Quack, and Dr. Byung-wook Yoo. Finally, I want to acknowledge the entire optoelectronic group at Berkeley EECS for being the best colleagues and friends I would have ever worked with. Specifically, I want to thank Roger Chen, Frank Rao, Dr. Chris Chase, Wilson Ko, James Ferrara, Forrest Sedgewick, Matthias Kuntz, Vadim Karagodsky, Thai Tran, Devang Parekh, Nikhil Kumar, Matteo Staffaroni, Sapan Agarwal, and Owen Miller.

I spent so much time struggling, enjoying, and persevering in the Nanolab. I want to thank everyone in the community who helped me on my way and who shared the good and bad times with me. I specifically want to thank Jay Morford, Joe Donnelly, Evan Stateler, David Lo, Bob Hamilton, Bill Flounders, and the rest of the Nanolab staff for the excellent work they do to make the cleanroom an example for all other universities.

Without funding, I would never have achieved my doctorate. I would like to thank the NSF Graduate Fellowship, DARPA NACHOS, Samsung, CIAN NSF-ERC, and E3S for their generous support.

Finally, I want to thank my mom, dad, brother, sister, extended family, friends, and Sarah for all of the love, advice, and support they have given me through the good and bad times. You never gave up on me, and I won't give up on you. I love you all.

Chapter 1

Introduction

In many ways, the field of electrical engineering has been driven by our desire to control and manipulate electrons for useful purposes. As charged particles, electrons interact with each other heavily, and can be controlled by electric and magnetic fields easily via the Lorentz force law. In basic RLC circuits, the manipulation of current flow has resulted in myriad advances in human endeavor. Then, in the 1950's, the transistor was invented [1]. With one transistor, we enabled amplifiers. With a collection of a few transistors, we enabled rudimentary digital logic. This device which nonlinearly controlled electron flow, therefore, enabled computation. Today, we are able to manipulate charge with a *billion* transistors. The field of electrical engineering has created some of the most complicated and useful matter in the history of humanity. Today, almost every person in the United States carries millions of transistors and at least a few radios in a single cell phone. The ability of humans to control the flow of electrons indeed has had massive implications for the quality of human life.

As our ability to manipulate charge has increased, however, the ability to manipulate photons has been slower to emerge. Photons have no charge, and are thus not affected by electric and magnetic fields. For precisely this reason, however, they are exceedingly useful to communicate information. Without the risk of getting corrupted by stray electromagnetic fields, a photon is an ideal communicator. Furthermore, the photon is one of the most fundamental and powerful ways to probe matter and sense chemicals. All materials absorb and emit light differently and thus are able to be identified through photon interactions. This quantum light-matter interaction, first proposed by Planck [2] and Einstein [3], serves as the basis for every attempt to use light to our advantage.

Thus, there is ample motivation to control photons and to costlessly convert them to and from electrons. Besides computation and communication, capturing and/or measuring the properties of light is useful for photography [4], spectroscopy, photovoltaics [5], etc. Light-based sensing via fluorescence [6] and Raman spectroscopy [7] has led to major advances in biology, among many other fields. Recently, using light for quantum cryptography [8] and

quantum computation [9] may one day completely change communication and computation. Nonlinear light-matter interactions can convert photons to different frequencies [10], impart mechanical force on matter [11], and even shape and sculpt materials.

With all of these possibilities, the challenge for engineers is to find the most efficient way of accomplishing all of these tasks. In computation, efficiency was introduced by integrating millions of transistors onto a single, unifying platform. Can we achieve better photonic designs and functionality with the same integration techniques used for computation [12]? If so, how will we marry electrons and photons onto a single platform capable of harnessing the power of both?

In this marriage, however, one finds that there is a major problem with relying on photons for communication and electrons for computation. By using two fundamentally different particles to perform these basic tasks, methods must be developed to convert light to electrons (optical-electrical, or OE conversion), and electrons to light (electrical-optical, or EO conversion) . Together, this OEO conversion imposes major costs on information technology [13].

The penalties induced by OEO conversion has already affected the way that we engineer information technology. On current computer chips, you will not find transistors relaying information via photons. They are connected simply by an electrical wire, for a photonic link is a much more complicated technology. Yet, as we advance in our design of transistors via Moore's Law [14], the major engineering difficulties will arise due precisely to the fact that we use electrons to communicate instead of photons. According to Miller, by using lossy electrons to communicate, we may come to a point where we are consuming all 150 W of available computing power just to connect various cores on one computer chip, let alone actually performing useful computation [15].

In photonic communication links, we run into the same issues with photonic design complexity. Even with the large advantages enjoyed by communicating via photons in these links, using photons for logic is currently not feasible. Thus, we expensively convert them to electrons for the computation. There is no other option for routing photons.

Therefore, there is a major dichotomy in electronic and photonic technologies. Transistors and electron manipulation is trivially cheap thanks to standardization and Moore's Law. Photonics and OEO conversion, on the other hand, is still not standardized and is costly to design and implement as a result. The diversity of photonics, in many ways has been a blessing and a curse for wide-spread adoption. Surely, there is much to gain by integrating photonics onto single platforms.

Like transistors, the integration of photonic devices into photonic integrated circuits (PIC's) can reduce energy, fabrication, and development by orders of magnitude. Yet, in order to make these circuits, the individual circuit elements must be designed and optimized. Light emitters, light waveguides, and photodetectors would be the basic building blocks for PICs. For true functionality, however, light modulators, attenuators, (de)multiplexers, and amplifiers will also be needed (among other things) [13].

An ideal photonic source would be able to use every property of light to transmit information efficiently and probe matter precisely. Thus, controlling the frequency, polarization,

and speed at which light is modulated would give us ultimate control. Such a device was invented on May 16, 1960 when Ted Maiman operated the first laser (*l*ight *a*mplification by *s*timulated *e*mission of *r*adiation) and demonstrated unprecedented control over light [16].

Since its invention, many different types of novel, interesting, and useful coherent light sources have been developed for countless applications. The invention of semiconductor double heterostructures further propelled laser technology by allowing the creation of electrically injected lasers based on semiconductor materials [17]. Such lasers have been used in many applications including telecommunications, multimedia, sensing, etc. Even with the remarkable success of lasers in many areas of human life, their usage has barely scratched the surface of potential applications.

In order to improve the energy consumption, modulation speed, and functionality of lasers on PIC's, the size of the devices must decrease [18]. Therefore, nanocavity lasers have attracted immense interest in many scientific communities due to their many potential applications in physics [19–21], imaging [22], sensing [23–26], data storage [27], optical interconnects [15, 28, 29], etc. For example, nanolasers capable of transmitting information with 1 fJ/bit of energy at high data rates (using wavelength division multiplexing) will have huge implications for how information is communicated in microprocessor technology [15].

The march to the creation of nanolasers has spanned many decades. Starting with the invention of the double heterostructure laser [17], the field has progressed in creating microcavity lasers such as vertical-cavity surface-emitting lasers (VCSELs) [30, 31], microdisks [32, 33], and photonic crystals [34–37]. These cavities have succeeded in shrinking electromagnetic mode volumes down to diffraction limits.

Efforts to squeeze electromagnetic mode volumes down to sub-diffraction limits require metal. The demonstration of nanolasers that utilize metal-optics and plasmonics has created a revolution in nanophotonics. A wide variety of fields including data storage, photolithography, integrated photonics, and biosensing stand to benefit immensely from a subwavelength source of light [38].

Using plasmonics to squeeze "large" photons into "small" plasmons can create subwavelength light sources [39–44]. Laser oscillations have even been observed at room temperature [43]. The ultimate goal of plasmon lasers will be to demonstrate a device that confines light into a volume of $(\lambda_{sp}/2)^3$ in a commensurately small physical volume V_{phys} as well. Yet to date, most plasmon based lasers confine light in only one or two dimensions. We believe that research into mitigating metal loss and designing nanocavities with low radiation rates in *small volumes* will both be critical for future applications.

In order to minimize metal loss, many groups have decided to use metal as a reflector instead of a plasmonic material [38, 45–50]. As metal is introduced to a small semiconductor cavity, a large amount of radiation can be blocked. Using metal, a seemingly undesirable purely dielectric cavity can be converted into a nanoscale laser. As the metal comes closer to the cavity, however, ohmic losses also increase. In Chapter 3, I will discuss the tradeoffs between radiation and metal losses in engineering these nanocavities with small V_{phys} [51].

Many semiconductor nanolasers have been demonstrated that operate at room temperature [43, 46, 48–50], are electrically driven [38, 39, 48, 49], and operate in continuous-wave

[48, 49]. Yet the physical volume of a laser, V_{phys}, is quite possibly the most important feature of the nanolaser since the fundamental size limit of these devices will ultimately illuminate what applications we can hope to enable with future development.

In this dissertation, I will explore the implications of using metal for nanolasers. In Chapter 2, a brief introduction to to metal-optics and gain materials will be given. In Chapter 3, I will dive deeper into the various design considerations necessary to make successful nanolasers and also present examples of plasmonic and metal-optics cavity designs that have not yet been realized. In Chapters 4 and 5, I will present experimental demonstrations of nanolasers that utilize plasmonics (Chapter 4) and metal-optics (Chapter 5). In Chapter 4, I will present the plasmonic crystal defect nanolaser [44]. The laser design is the first to attempt to confine surface plasmons in all three dimensions to a subwavelength electromagnetic mode volume. Furthermore, the laser is integrated into a plasmonic crystal capable of serving as a platform for complete nanophotonic circuit integration. Finally, in Chapter 5, I will demonstrate the nanopatch laser [45, 47]. The laser design has world-record-setting small physical volume, and therefore represents a significant step towards realizing super-efficient coherent light sources.

Chapter 2

Light-Matter Interactions for Semiconductor Nanolasers

Light-matter interactions in metals and various gain materials are the basis for building successful nanolasers. The difference between successful and unsuccessful nanolaser designs ofter rely on the materials with which these devices were made.

To understand how these materials will help or hinder nanolaser design, I will first introduce how metals behave in the presence of light. It is well known that metals tend to reflect incident light (this is the reason they are shiny) and repel any sort of electric field that is parallel to its surface. The transduction of light into surface plasmon polaritons (SPPs), however, is less commonly seen. Thus, I will go over basic properties of these SPPs to understand how they might help with nanolaser design.

Finally, I will review the basic concepts of how optical frequency gain can be achieved by materials. First, I will review how light is absorbed by materials. Next, I will explain how materials emit light via spontaneous and stimulated emission. Finally, I will show examples of gain materials that will merit consideration for nanolaser operation.

2.1 Metal-Optics

2.1.1 Optical Properties of Metals

At low frequencies, metals have a very large negative permittivity ϵ_m (essentially negative infinity). At optical frequencies, the behavior of metal changes qualitatively. At visible

frequencies, the electrons in the metal approach a regime where $|\epsilon_m|$ approaches zero, so that the response of free electrons becomes very limited (Fig. 2.1). Many rich and interesting phenomena happen as this so-called plasma frequency is reached.

Firstly, bulk electron motion can be excited so that electrons are oscillating as a nearly-free plasma. Broadly speaking, these electron oscillations can occur in (1) the bulk of the metal material, or (2) at the surface of a metal/dielectric interface. To understand the response of the bulk electron plasma inside a metal, the Drude model of metal permittivity can be used. After knowing the permittivity of the metal, its response to an electric field of any frequency is known. To derive the permittivity of a metal , ϵ_m, I first assumed that the electron gas is not bound (although there can be collisions), and the electrons have some characteristic damping frequency. Then, the response of the electron gas in the metal to a time varying electric field can be derived using simple Newtonian mechanics:

$$m\ddot{\mathbf{x}} + m\gamma\dot{\mathbf{x}} = -q\mathbf{E}$$
$$x = \frac{q}{m(\omega^2 + i\omega\gamma)}E$$

where m is the effective mass of an electron in the metal lattice, x is the displacement of the electron, q is the unit of electric charge, E is the applied electric field, and γ is the damping frequency of the electron gas. I also assume $\mathbf{x} = xe^{-i\omega t}$ and $\mathbf{E} = Ee^{-i\omega t}$.

Knowing the displacement of the electron gas due to an electric field allows us to find the polarizability and dielectric constant of the metal:

$$\vec{P} = -nq\vec{x} = -nq\frac{q}{m(\omega^2 + i\gamma\omega)}\vec{E}$$
$$\vec{D} = \epsilon\vec{E} = \epsilon_0\vec{E} + \vec{P}$$
$$\vec{D} = \left[\epsilon_0 - \frac{nq^2}{m(\omega^2 + i\gamma\omega)}\right]\vec{E}$$
$$= \epsilon_0\left[1 - \frac{\omega_p^2}{\omega^2 + i\gamma\omega}\right]\vec{E} \text{ where } \omega_p^2 = \frac{nq^2}{\epsilon_0 m}$$

where $\vec{P}$ is the dipole moment per unit volume and n is the density of electrons in the metal and ω_p is called the plasma frequency of the electron gas.

The permittivity of the metal is then:

$$\epsilon_m = \left[1 - \frac{\omega_p^2}{\omega^2 + i\gamma\omega}\right] \tag{2.1}$$

Intuitively, the plasma frequency ω_p of an electron gas is the maximum frequency for which the plasma can respond to an oscillating electric field. Thus, below this frequency, electromagnetic waves incident on a metal surface are reflected, while the metal becomes transparent to any radiation above this frequency.

6
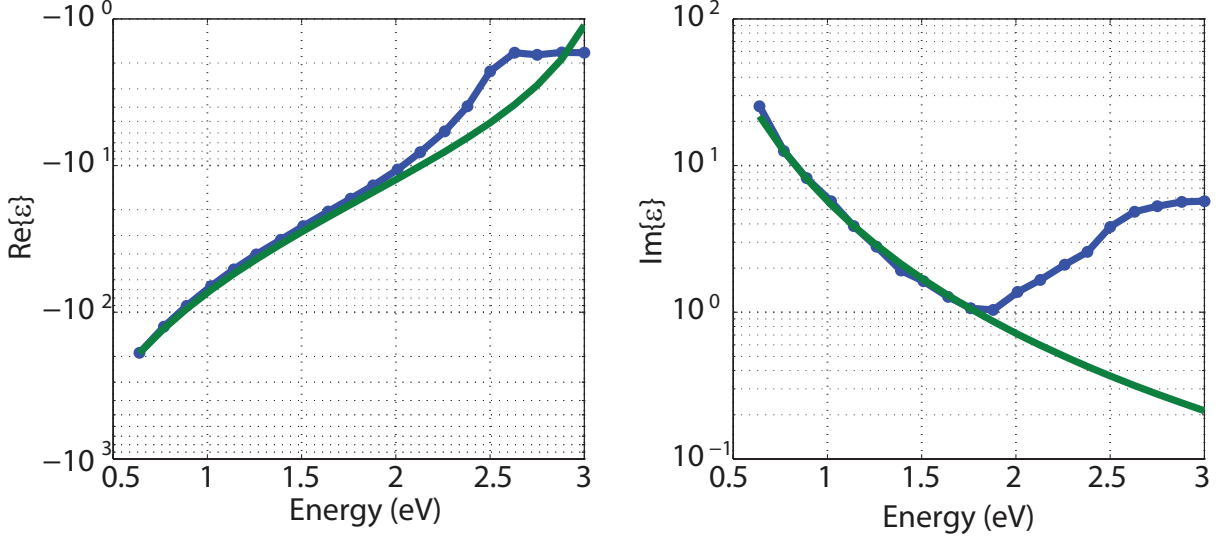
Figure 2.1. The real (left panel) and imaginary (right panel) dielectric response of gold. Blue lines represents experimental data [52] while green lines represent a fit with the Drude model.

It is important to note that as the dielectric constant of metal approaches 0, the Drude model breaks down (Fig. 2.1). Inside noble metals such as gold or silver, interband transitions begin to affect the response of electrons in the metal such that new models must be introduced. These transitions are essentially resonances within the metal due to bound charge. The Drude model can be modified by introducing the resonance(s):

$$m\ddot{x} + m\gamma\dot{x} + \omega_0^2 x = -qE$$
$$P = -nqx = \frac{nq^2}{m} \frac{E}{(\omega_0^2 - \omega^2 - i\gamma\omega)}$$

The permittivity a medium with multiple bound electron resonances, along with a free electron sea (which corresponds to $\omega_0 = 0$) is:

$$\epsilon(\omega) = 1 - \frac{f_1 \omega_p^2}{\omega^2 - i\gamma\omega} + \omega_p^2 \sum_j \frac{f_j}{\omega_j^2 - \omega^2 - i\gamma_j\omega} \tag{2.2}$$

where $\sum_j f_j = 1$ satisfies the oscillator sum rule. The first two terms of the permittivity are associated with the Drude model, and the sum over bound electron oscillators will contribute to the overall polarizability of the material. Although the full model can be used to describe gold at high energies, I will use the simple Drude model in this dissertation and neglect interband transitions since I will be focusing on developing nanolasers near $\hbar\omega = 0.8$ eV which is much below the first interband transition in both gold and silver (the two metals with the lowest collision frequency in nature).

From the Drude model, a large carrier density, n, and low effective mass, m, will enable very high oscillation frequencies before the free electron gas response starts to diminish.

7

The damping frequency, γ, for most metals is on the order of 100 THz. Thus, above this frequency, the damping term becomes less important as collisions are reduced in number. In Table 2.1, I summarize fitted parameters of ω_p, f_j, γ, and ω_j for gold, silver, copper, and aluminum. Materials such as gold and silver are exceptionally useful for designing metallic cavities due to their low loss.

Table 2.1. Summary of Lorentz-Drude parameters for various metals [52, 53].

Material					j			
		1	2	3	4	5	6
	ω_p	9.01					
	f_j	0.845	0.065	0.124	0.011	0.840	5.646
Ag	ω_j	0.000	0.816	4.481	8.185	9.083	20.29
	γ_j	0.048	3.886	0.452	0.065	0.916	2.419
	ω_p	14.98					
	f_j	0.523	0.227	0.050	0.166	0.030	-
Al	ω_j	0.000	0.162	1.544	1.808	3.473	-
	γ_j	0.047	0.333	0.312	1.351	3.473	-
	ω_p	10.03					
	f_j	0.760	0.024	0.010	0.071	0.601	4.384
Au	ω_j	0.000	0.415	0.830	2.969	4.304	13.32
	γ_j	0.043	0.221	0.405	0.870	0.094	2.014
	ω_p	10.83					
	f_j	0.575	0.061	0.104	0.723	0.638	-
Cu	ω_j	0.000	0.291	2.957	5.300	11.18	-
	γ_j	0.030	0.378	1.056	3.213	4.305	-

A more intuitive circuit-model theory of metal-optics has also been developed rigorously by Staffaroni and Yablonovitch [54]. For example, although I derived the the plasma frequency ω_p using Newtonian mechanics, circuit theory can also be used for the same derivation. Of course, the electron gas movement is nothing else but an optical frequency current, and so flows in the metal with some characteristic inductance L and capacitance C. The plasma frequency is then $\omega_p = \sqrt{1/LC}$. By realizing that the electron behavior below the

plasma frequency can be described by electrical circuits, highly intuitive designs of optical nanocavities, transmission lines, filters, and even transformers can be realized.

Understanding the usefulness of circuit models, I summarize the permittivity ϵ, the conductivity σ, and the resistivity ρ for a Drude metal:

$$\epsilon = 1 - \frac{\omega_p^2}{\omega^2 + i\gamma\omega}$$

$$= 1 + \frac{i\sigma}{\epsilon_0\omega}$$

$$\sigma = \epsilon_o\omega_p^2\frac{\omega}{\gamma\omega - i\omega^2}$$

$$\rho = \frac{1}{\epsilon_0\omega_p^2}(\gamma - i\omega)$$

Thus, the resistivity of the metal is complex. The real part of the resistivity is essentially ohmic loss due to electron scattering. The imaginary part of the resistivity, however, is reminiscent of an impedance $Z_L = i\omega L_{kinetic} = i\omega\frac{1}{\epsilon_0\omega_p^2}$ so that $L_{kinetic} = \frac{1}{\epsilon_o\omega_p^2}$. In metal-optics circuit theory, this kinetic inductance is present solely because of electron inertia. Magnetic inductance can also be present in this regime but scales adversely with size such that it becomes insignificant in extremely subwavelength optical circuitry. Magnetic inductance, however, can play a major role in shaping optical circuitry in the near-infrared regime, where $L_{kinetic} < L_{magnetic}$.

The bulk response of electrons in metals can occur in both at the macro- and nanoscale. The more interesting length scale for metal-optics is, of course, the nanometer scale. If metal is shaped at such small dimensions, these "bulk plasmons" can resonate at frequencies that depend on the size and shape of the metal. At the nanometer scale, however, such collective oscillations can be used in antenna phenomenon. The implications of nanoscale bulk plasmons for lasers has been demonstrated by Noginov et al. [40].

2.1.2   Single-Sided Surface Plasmons

Besides bulk plasmons, metals can also support surface plasmon polaritons (SPPs). Single-sided SPPs are waves that exist at the interface between a metal with a negative perimittivity ϵ_m and a dielectric with a positive permittivity ϵ_d. Because these waves are bound to this interface, they decay exponentially away from the interface. To find the analytical solution for this particular type of wave, I start with Maxwell's equations:

$$\nabla \cdot \vec{D} = \rho_{free} \tag{2.3}$$

$$\nabla \times \vec{E} = -\frac{\partial \vec{B}}{\partial t} \tag{2.4}$$

$$\nabla \cdot \vec{B} = 0 \tag{2.5}$$

$$\nabla \times \vec{H} = \vec{J}_{free} + \frac{\partial \vec{D}}{\partial t} \tag{2.6}$$

where $\vec{E}$ is the electric field vector, $\vec{D} = \epsilon \vec{E}$, $\vec{B}$ is the magnetic field vector, $\vec{H} = \frac{\vec{B}}{\mu}$, ρ_{free} is free charge, $\vec{J}_{free}$ is free current, and μ is the permeability of a material (usually $\mu = \mu_0 = 4\pi \times 10^{-7} N A^{-2}$). In the absence of external charge and current, I can combine equations 2.3 and 2.6 to obtain the Helmholtz wave equation:

$$\nabla \times \nabla \times \vec{E} = -\nabla \times \frac{\partial \vec{B}}{\partial t} = -\frac{\partial}{\partial t} \nabla \times \vec{B} \tag{2.7}$$

$$\nabla \times \nabla \times \vec{E} = -\mu_0 \frac{\partial \vec{D}}{\partial t} \tag{2.8}$$

$$\nabla^2 \vec{E} - \mu_0 \epsilon_0 \epsilon \frac{\partial^2 \vec{E}}{\partial t^2} = 0 \tag{2.9}$$

$$\nabla^2 \vec{E} - \frac{\epsilon}{c^2} \frac{\partial^2 \vec{E}}{\partial t^2} = 0 \tag{2.10}$$

where $\mu_0 \epsilon_0 = 1/c^2$ and we use the vector identity $\nabla \times \nabla \times \vec{E} \equiv \nabla(\nabla \cdot \vec{E}) - \nabla^2 \vec{E}$ and 2.3 to simplify 2.8 to 2.9.

By assuming a harmonic dependence on time where $\vec{E}(\vec{r}, t) = \vec{E}(\vec{r})e^{i\omega t}$, I simplify 2.10 further to obtain the Helmholtz equation:

$$\nabla^2 \vec{E} + k^2 \vec{E} = 0 \tag{2.11}$$

where $k = \omega n/c$ and $n = \sqrt{\epsilon}$ is the index of refraction.

Next, I must define the coordinate system in which the surface plasmon will propagate. The wave propagates along the x-direction in Fig. 2.2, decays evanescently in the z-direction, and is homogeneous along the y-direction.
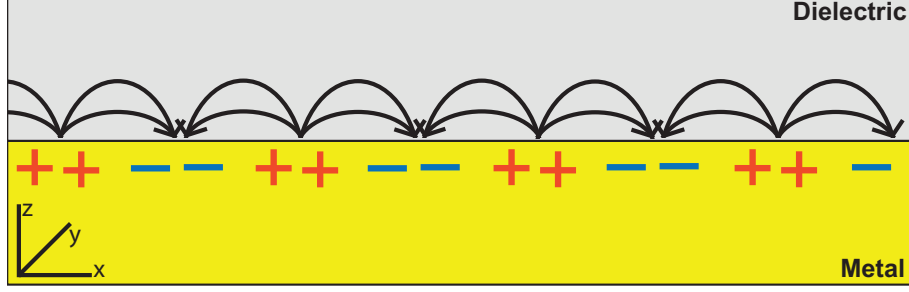
Figure 2.2. A surface plasmon wave propagating along the x-direction. The wave is homogeneous along the y-direction and decays evanescently in the z-direction

Thus, the electric and magnetic fields must take the form:

$$\vec{E}(x, y, z) = \begin{cases} \vec{E}(x, z)e^{i\beta x}e^{-k_1 z} & \text{if } z > 0, \\ \vec{E}(x, z)e^{i\beta x}e^{k_2 z} & \text{if } z < 0. \end{cases} \tag{2.12}$$

$$\vec{H}(x, y, z) = \begin{cases} \vec{H}(x, z)e^{i\beta x}e^{-k_1 z} & \text{if } z > 0, \\ \vec{H}(x, z)e^{i\beta x}e^{k_2 z} & \text{if } z < 0. \end{cases} \tag{2.13}$$

In order to find explicit equations for $\vec{E}$ and $\vec{H}$, I expand equations 2.4 and 2.6:

$$\frac{\partial E_z}{\partial y} - \frac{\partial E_y}{\partial z} = i\omega\mu_0 H_x \tag{2.14a}$$

$$\frac{\partial E_x}{\partial z} - \frac{\partial E_z}{\partial x} = i\omega\mu_0 H_y \tag{2.14b}$$

$$\frac{\partial E_y}{\partial x} - \frac{\partial E_x}{\partial y} = i\omega\mu_0 H_z \tag{2.14c}$$

$$\frac{\partial H_z}{\partial y} - \frac{\partial H_y}{\partial z} = -i\omega\epsilon_0\epsilon E_x \tag{2.14d}$$

$$\frac{\partial H_x}{\partial z} - \frac{\partial H_z}{\partial x} = -i\omega\epsilon_0\epsilon E_y \tag{2.14e}$$

$$\frac{\partial H_y}{\partial x} - \frac{\partial H_x}{\partial y} = -i\omega\epsilon_0\epsilon E_z \tag{2.14f}$$

and substitute in equations 2.12 and 2.13:

$$\frac{\partial E_y}{\partial z} = i\omega\mu_0 H_x \tag{2.15a}$$

$$\frac{\partial E_x}{\partial z} - i\beta E_z = i\omega\mu_0 H_y \tag{2.15b}$$

$$i\beta E_y = i\omega\mu_0 H_z \tag{2.15c}$$

$$\frac{\partial H_y}{\partial z} = -i\omega\epsilon_0\epsilon E_x \tag{2.15d}$$

$$\frac{\partial H_x}{\partial z} - i\beta H_z = -i\omega\epsilon_0\epsilon E_y \tag{2.15e}$$

$$i\beta H_y = -i\omega\epsilon_0\epsilon E_z \tag{2.15f}$$

These coupled equations are nothing but Maxwell's equations and lead to transverse magnetic (TM) and transverse electric (TE) polarized waves. In TM waves, $E_x, E_z,$ and H_y are nonzero, and in TE waves, $E_y, H_x,$ and H_z are nonzero. It can easily shown that for a wave that evanescently decays in the z-direction, no TE wave exists. Thus, I will focus on the TM wave. In this case, equations 2.14a, 2.14b, and 2.14f govern the solution so that the mode profiles for the surface plasmon are:

$$\left. \begin{aligned} H_y(z) &= A_2 e^{i\beta x} e^{-k_2 z} \\ E_x(z) &= iA_2 \frac{1}{\omega\epsilon_0\epsilon_2} k_2 e^{i\beta x} e^{-k_2 z} \\ E_z(z) &= -A_1 \frac{\beta}{\omega\epsilon_0\epsilon_2} e^{i\beta x} e^{-k_2 z} \end{aligned} \right\} z > 0 \qquad \left. \begin{aligned} H_y(z) &= A_1 e^{i\beta x} e^{k_1 z} \\ E_x(z) &= -iA_1 \frac{1}{\omega\epsilon_0\epsilon_1} k_1 e^{i\beta x} e^{k_1 z} \\ E_z(z) &= -A_1 \frac{\beta}{\omega\epsilon_0\epsilon_1} e^{i\beta x} e^{k_1 z} \end{aligned} \right\} z < 0 \quad (2.16)$$

Finally, I will use boundary conditions for the electric and magnetic fields $E_{1\parallel} = E_{2\parallel}$ and $H_{1\parallel} = H_{2\parallel}$ to find the dispersion $\beta(\omega)$ for SPPs. From equation 2.16, continuity in H_y dictates that $A_1 = A_2$, and continuity in E_x dictates that:

$$\frac{k_2}{\epsilon_2} = -\frac{k_1}{\epsilon_1} \tag{2.17}$$

The dispersion relation $\beta(\omega)$ can now be derived from 2.17 and the Helmholtz equation 2.11. By plugging in the mode profiles for H_z above and below the $z = 0$, we find two wavevector relations for that H_y must obey:

$$k_1^2 = \beta^2 - k_0^2 \epsilon_1 \tag{2.18a}$$
$$k_2^2 = \beta^2 - k_0^2 \epsilon_2 \tag{2.18b}$$

Substituting 2.17 into 2.18, the dispersion relation for a single-sided surface plasmon is:

$$\left(\frac{\epsilon_2}{\epsilon_1}\right)^2 k_1^2 = \beta^2 - k_o^2 \epsilon_2$$

$$\left(\frac{\epsilon_2}{\epsilon_1}\right)^2 \left[\beta^2 - k_0^2 \epsilon_1\right] = \beta^2 - k_o^2 \epsilon_2$$

$$\left[\left(\frac{\epsilon_2}{\epsilon_1}\right)^2 - 1\right]\beta^2 = k_0^2 \left[\left(\frac{\epsilon_2}{\epsilon_1}\right)^2 \epsilon_1 - \epsilon_2\right] \tag{2.19}$$

$$\beta^2 = k_0^2 \frac{\epsilon_2 (\epsilon_2 - \epsilon_1)}{\epsilon_1} \cdot \frac{\epsilon_1^2}{\epsilon_2^2 - \epsilon_1^2}$$

$$\beta = \frac{\omega}{c} \cdot \sqrt{\frac{\epsilon_1 \epsilon_2}{\epsilon_1 + \epsilon_2}}$$

Because the dispersion relation was derived without any assumptions about the nature of the relative dielectric constants ϵ_1 and ϵ_2, this relation holds for real and complex dielectric constants. The dispersion relation for a single-sided surface plasmon for dielectrics with three different refractive indices interfaced with silver is shown in Fig. 2.3, and $\lambda_{sp_0}(\omega)$ is displayed in Fig. 2.4. These dispersion curves include the resistance loss present in the silver. Thus, a single-sided surface plasmon can achieve a 28% reduction in wavelength with a silver/air interface plasmon and a 66% reduction in wavelength with a silver/semiconductor interface with $n = 3.5$ at their respective plasmon resonances!
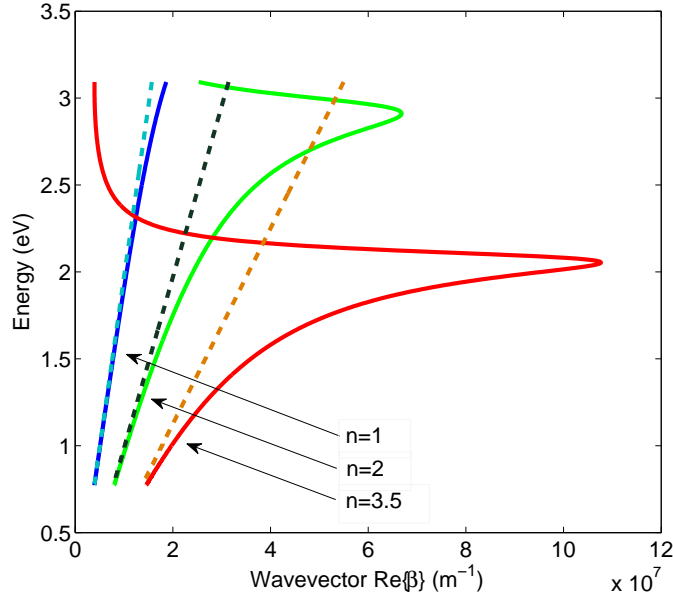
Figure 2.3. A plot of the dispersion relation for a single-sided surface plasmon between silver and three materials with different refractive indices. The straight lines represent the "light line" which consists of the wavevectors of photons in the respective dielectric medium.

13
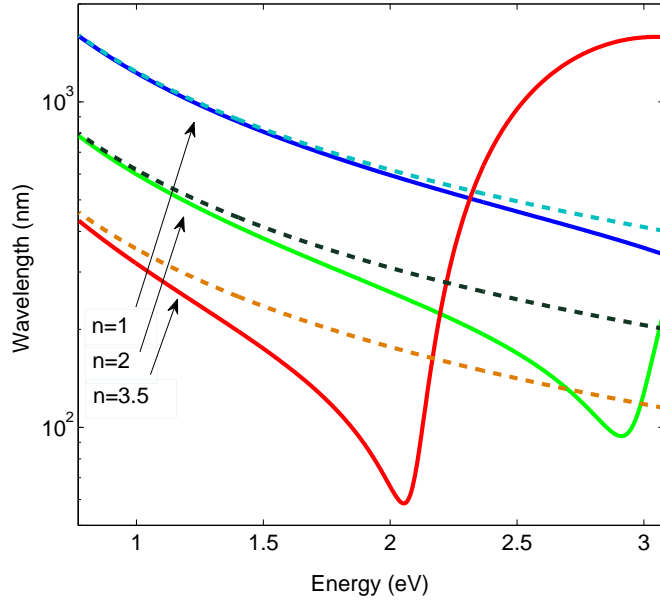
Figure 2.4. A plot to compare the wavelengths of photons and surface plasmons in media with three different refractive indices. The broken lines present the wavelength of a photon in a particular dielectric medium while the solid lines represent the wavelengths of surface plasmons at the interface of silver and a dielectric with index n.
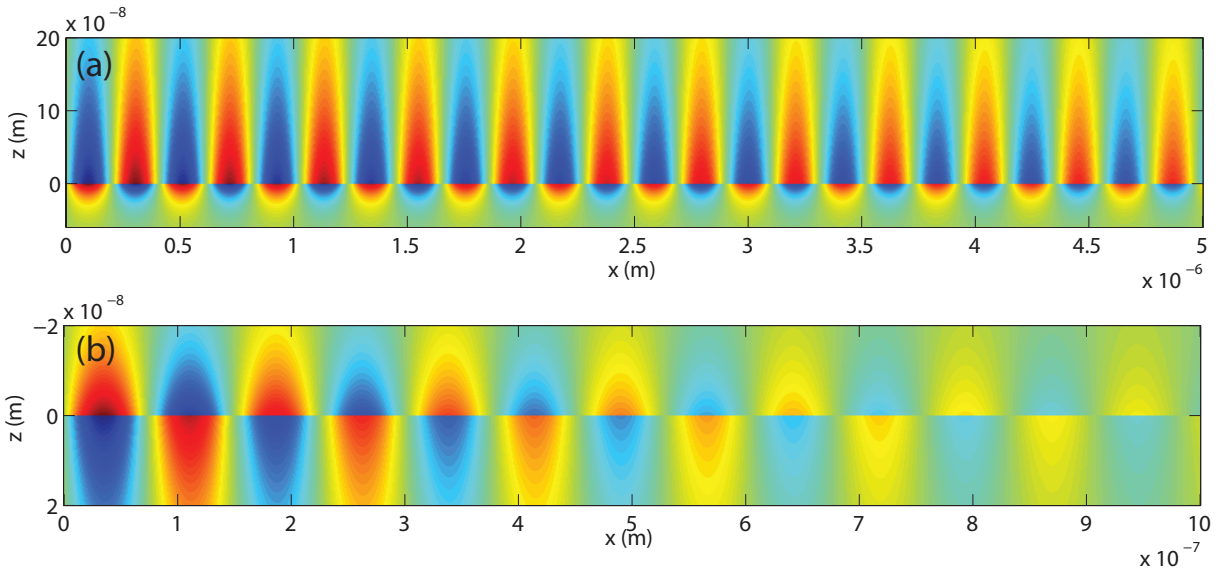
Figure 2.5. (a) A plot of $\Re(E_x)$ for a surface plasmon with energy $\hbar\omega = 0.8$ eV. (b) A plot of $\Re(E_x)$ for a surface plasmon with energy $\hbar\omega = 1.6$ eV. Note the difference in both x- and z- scales for the two energies. In both cases, the waves decay due to metal ohmic loss, but the wave at $\hbar\omega = 1.6$ eV decays much faster than the wave at 0.8 eV.

Yet even with these modest volume reductions, we find that there is a large penalty paid. In essence, a surface plasmon is simply the electromagnetic energy of a photon coupled to a electrical current in a metal. Mode profiles for $\Re(E_x)$ for single-sided surface plasmons at two different energies are shown in Fig. 2.5. The electrical current in the metal inevitably experiences ohmic resistance and therefore dissipates optical frequency energy as the plasmon travels across the metal/dielectric interface. The distance a surface plasmon can propagate before it loses $1/e$ of its energy is shown in Fig. 2.6. This propagation distance can be simply calculated as $l = 1/(2\beta'')$.
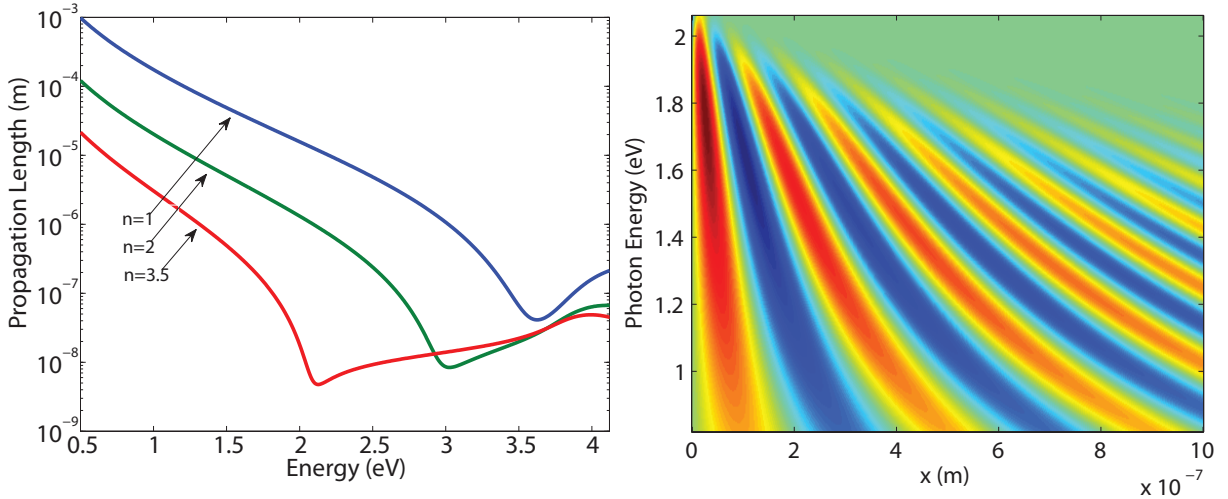
Figure 2.6. (a) A comparison of the propagation lengths of surface plasmons between silver and various dielectric materials with refractive indices shown in the figure. As the photon energy approaches the plasmon resonance, more and more energy is lost to metal ohmic loss. (b) A plot of $\Re(E_x(x,z)) = \Re(E_x(x,0))$ for various photon energies when the dielectric index of refraction is $n = 3.5$. The surface plasmon propagates much shorter distances at higher photon energies due to larger ohmic loss.

2.1.3 Multi-Sided Surface Plasmons

So far, we have found that single-sided surface plasmons have the potential to shrink photons by squeezing the energy into a much more compact surface oscillation. Yet, the amount that a photon can be squeezed was limited by the dielectric medium which interfaces with air. Even with a silver/semiconductor interface, optical frequency radiation can acheive a maximum wavelength reduction of 66% relative to a photon of the same energy. Furthermore, this reduction only comes when $\epsilon_1 = -\Re(\epsilon_2(\omega))$ so that the shrinking occurs in a narrow bandwidth.

By introducing a second metal film on top of a thin dielectric region, photons can be further squeezed into even smaller volumes. This metal-insulator-metal (MIM) multilayer system can be analyzed in the same way as a single-sided surface plasmon. A depiction of
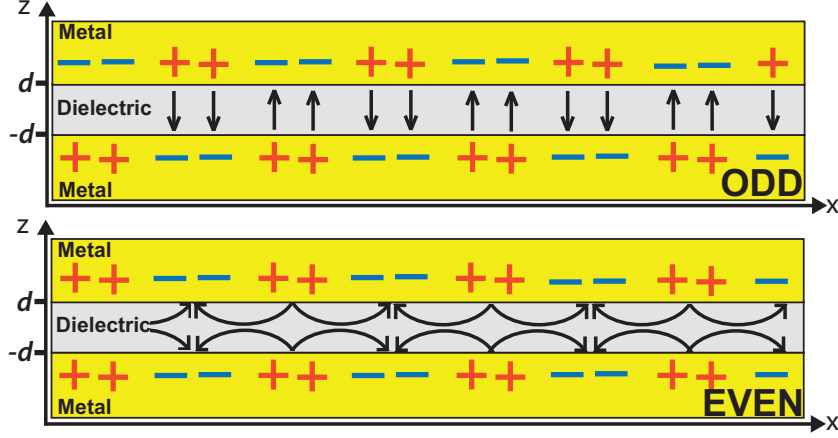
Figure 2.7. The two MIM "transmission line" plasmon modes are shown with charge configuration and field lines in the dielectric layer.

the MIM geometry is shown in Fig. 2.7. With two metal films, the charge oscillations can be symmetric (even) or anti-symmetric (odd) about the middle of the dielectric $z = 0$ interface.

To analyze the MIM plasmonic waveguide, we start again with the electric and magnetic field profiles. Plasmons only exist as TM waves, and so only H_y, E_x, and E_z exist. Furthermore, the wave travels in the x-direction and decays evanescently in as $z \to \pm\infty$.

$$
\left.\begin{aligned}
H_y(z) &= A e^{i\beta x} e^{-k_3 z} \\
E_x(z) &= iA \frac{1}{\omega\epsilon_0\epsilon_3} k_3 e^{i\beta x} e^{-k_3 z} \\
E_z(z) &= -A \frac{\beta}{\omega\epsilon_0\epsilon_3} e^{i\beta x} e^{-k_3 z}
\end{aligned}\right\} \quad z > d
$$

$$
\left.\begin{aligned}
H_y(z) &= B e^{i\beta x} e^{k_1 z} + C e^{i\beta x} e^{-k_1 z} \\
E_x(z) &= -iB \frac{1}{\omega\epsilon_0\epsilon_2} k_2 e^{i\beta x} e^{k_2 z} + -iC \frac{1}{\omega\epsilon_0\epsilon_2} k_2 e^{i\beta x} e^{-k_2 z} \\
E_z(z) &= -B \frac{\beta}{\omega\epsilon_0\epsilon_2} e^{i\beta x} e^{k_2 z} + C \frac{\beta}{\omega\epsilon_0\epsilon_2} e^{i\beta x} e^{-k_2 z}
\end{aligned}\right\} \quad -d < z < d \qquad (2.20)
$$

$$
\left.\begin{aligned}
H_y(z) &= D e^{i\beta x} e^{k_1 z} \\
E_x(z) &= -iD \frac{1}{\omega\epsilon_0\epsilon_1} k_1 e^{i\beta x} e^{k_1 z} \\
E_z(z) &= -D \frac{\beta}{\omega\epsilon_0\epsilon_1} e^{i\beta x} e^{k_1 z}
\end{aligned}\right\} \quad z < -d
$$

Using the boundary conditions that H_y and E_x are continuous at the $z = d$ and $z = -d$ interfaces:

16

$$Ae^{-k_3 d} = Be^{k_2 d} + Ce^{-k_2 d}$$

$$\frac{A}{\epsilon_3}k_3 e^{-k_3 d} = -\frac{B}{\epsilon_2}k_2 e^{k_2 d} + \frac{C}{\epsilon_2}k_2 e^{-k_2 d} \qquad \Bigg\} \; z = d \qquad (2.21)$$

$$De^{-k_1 d} = Be^{-k_2 d} + Ce^{k_2 d}$$

$$\frac{D}{\epsilon_1}k_1 e^{-k_1 d} = -\frac{B}{\epsilon_2}k_2 e^{-k_2 d} + \frac{C}{\epsilon_2}k_2 e^{k_2 d} \qquad \Bigg\} \; z = -d \qquad (2.22)$$

These boundary conditions coupled with momentum matching in each region ($k_i^2 = \beta^2 - k_0^2 \epsilon_i$), lead to a transcendental equation that defines the dispersion relation for a MIM geometry with arbitrary dielectric constants in each of the three regions:

$$e^{-4k_1 d} = \frac{k_2/\epsilon_2 + k_1/\epsilon_1}{k_2/\epsilon_2 - k_1/\epsilon_1}\frac{k_2/\epsilon_2 + k_3/\epsilon_3}{k_2/\epsilon_2 - k_3/\epsilon_3} \qquad (2.23)$$

This transcendental equation can be solved for a particular dielectric with refractive index $n = \sqrt{\epsilon_2}$ and thickness $2d$. In Fig. 2.8, the dispersion relation for a MIM surface plasmon for various thicknesses $2d$ for a dielectric medium of refractive index $n = 1$ is presented. In Fig. 2.9, the same dispersion for a dielectric with refractive index $n = 3.5$ is shown. The important thing to note here is that the wavevectors increase without limit as we make the dielectric thinner. Thus, by introducing a second metal layer, we can reduce the wavelength of optical frequency energy way beyond even a single-sided plasmon.
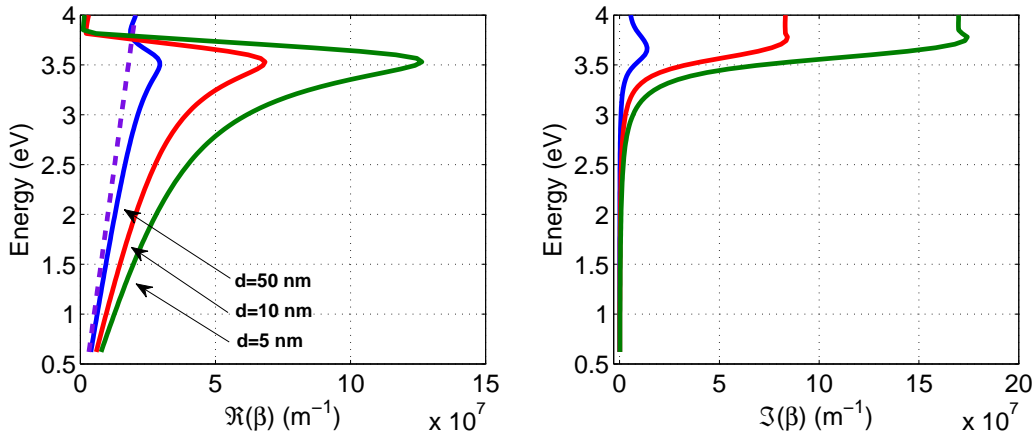
Figure 2.8. The real and imaginary component of the surface plasmon wavevector $\beta(\omega)$ for dielectric thicknesses of d=100 nm, d=20 nm, and d=10 nm for a dielectric with refractive index $n = 1$. The dotted line represents the light line $k = \omega n/c$.
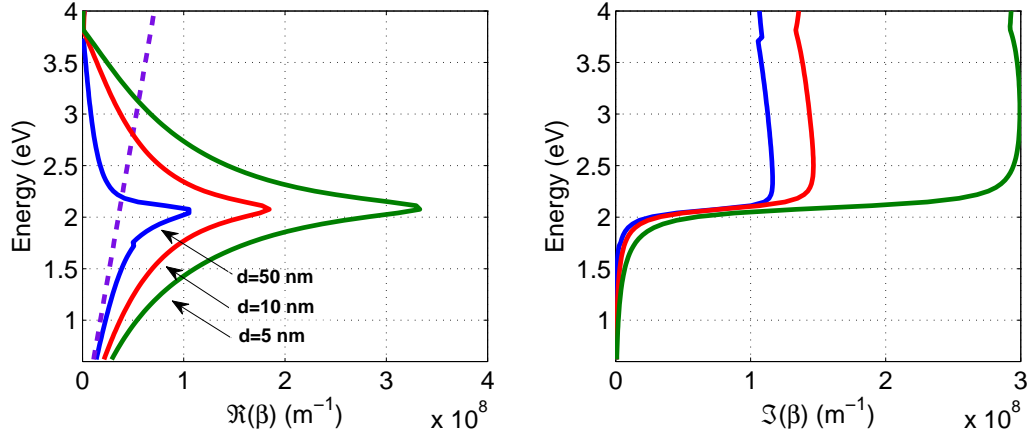
Figure 2.9. The real and imaginary component of the surface plasmon wavevector $\beta(\omega)$ for dielectric thicknesses of d=100 nm, d=20 nm, and d=10 nm for a dielectric with refractive index $n = 3.5$. The dotted line represents the light line $k = \omega n/c$.

Much like single-sided surface plasmons, however, the drawback of such tight confinement is the enormous loss that these waves incur in the metal layers as the dielectric region gets thinner. For a surface plasmon, the way to measure this loss is to find what the propagation length of the plasmon with respect to different dielectric thicknesses and photon energy. These propagation lengths are plotted in Fig. 2.10 for dielectrics with refractive indices of $n = 1$ and $n = 3.5$ and various thicknesses. Also, the mode profiles for MIM surface plasmons are displayed in Fig. 2.11 for photon energies of $\hbar\omega = 0.8$ and 1.6 eV. The propagation lengths of higher energy plasmons is much shorter due to higher ohmic loss.
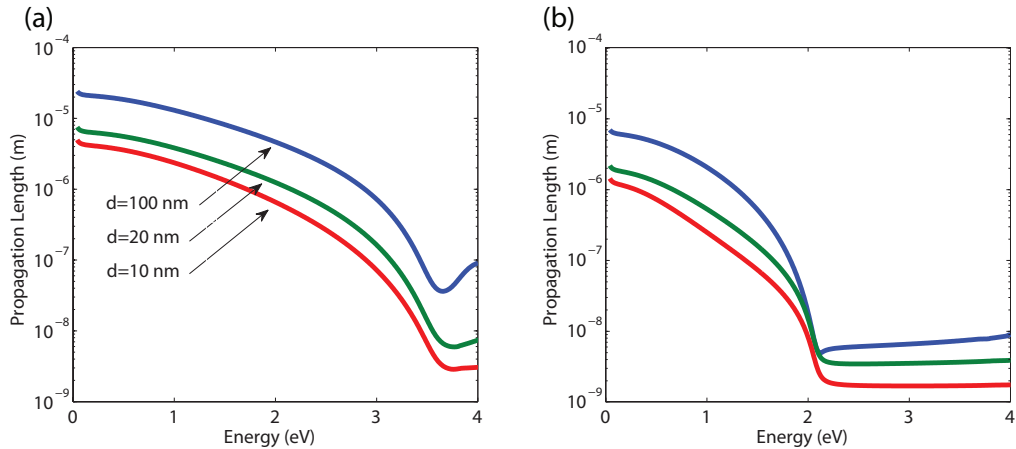
Figure 2.10. A plot of the propagation length of a MIM plasmon with a (a) dielectric material with $n = 1$ and (b) a dielectric material with $n = 3.5$. The propagation length is reduced as the thickness of the dielectric is reduced from 100 to 10 nm.

18
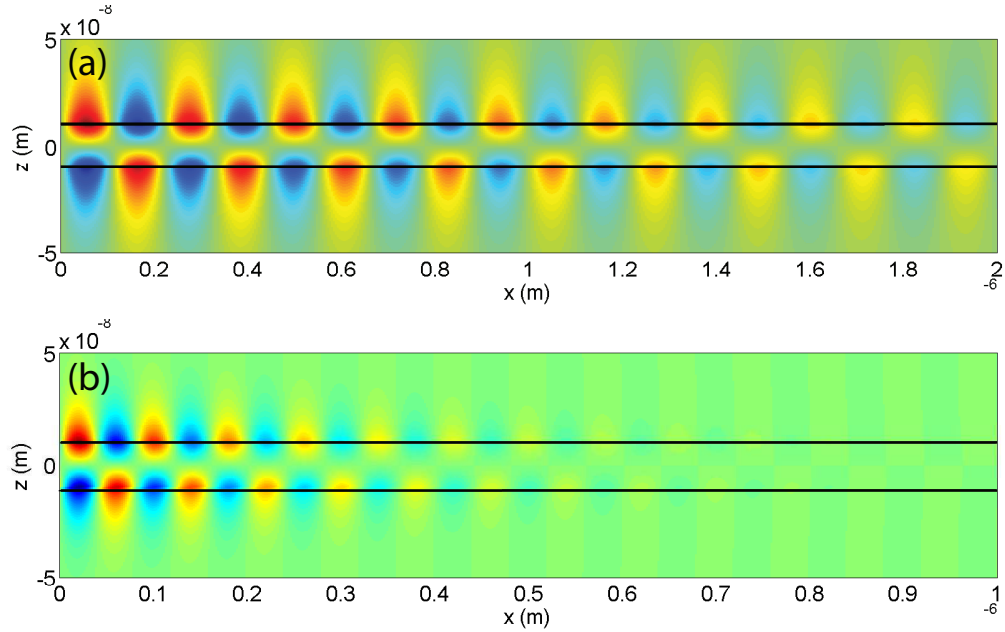
Figure 2.11. (a) A MIM plasmon propagating at an optical frequency $\hbar\omega = 0.8$ eV. (b) A MIM plasmon propagating at an optical frequency $\hbar\omega = 1.6$ eV. The plasmon with energy $\hbar\omega = 1.6$ eV can a much shorter propagation distance than the lower energy plasmon. In general, there is a tradeoff between surface plasmon wavelength (confinement) and propagation loss.

2.2   Light Amplifying Materials

Integrating light-generating materials with metallic nanocavities is the general strategy for creating subwavelength lasers. All materials are able to absorb light (or photons), but very few materials are able to then emit that light back out. Usually, the electronic excitation that occurs from light absorption is then dissipated into heat by a phonon bath. If, however, an electronic excitation is allowed to persist for roughly 1 ns, than the photon can be re-emitted via spontaneous emission. Today, light is regularly generated from singled-molecules (i.e. fluorescent dyes) or extended crystalline materials (such as direct-gap semiconductors).

In general, light can interact with matter in three different ways: 1) It can be absorbed, 2) it can be emitted spontaneously at a rate that is dependent on various properties of the material itself and its electromagnetic environment, or 3) it can be emitted after receiving stimulus from external photons. All three processes occur as electrons in the material interact with an electromagnetic field. Therefore, all three processes are intimately related.

2.2.1 Absorption

In the classical picture, absorption occurs when energy from an electromagnetic wave is absorbed by a material that is composed of oscillating dipoles. The dipoles in the material have a certain resonance frequency, and thus they will absorb light more efficiently if the frequency of the electromagnetic energy is at the resonance frequency of the material dipoles. Absorption, or α, is defined as:

$$\alpha[m^{-1}] = \frac{\text{density of photons absorbed}}{\text{photon flux}} \frac{[m^{-3}s^{-1}]}{[m^{-2}s^{-1}]} \tag{2.24}$$

To find how well a material absorbs, therefore, the rate at which photons are absorbed in a material and the photon flux (or the Poynting vector) must be found for any electromagnetic field propagating in the material.

To find the rate at which photons are absorbed, Fermi's Golden rule can be used to understand how an electron in a material interacts with an electromagnetic field:

$$\gamma_{abs} = \frac{2\pi}{\hbar}|\langle 2 \mid H' \mid 1\rangle|^2\delta(E_2 - E_1 - \hbar\omega)$$

where the δ-function enforces energy conservation and $|\langle 2 \mid H' \mid 1\rangle|^2$ is the matrix element of the perturbing Hamiltonian:

$$|\langle 2 \mid H' \mid 1\rangle|^2 = \int \Psi_2^*(\vec{r})H'(\vec{r})\Psi_1(\vec{r})dV$$

where $\Psi(\vec{r})$ are the electron wave functions of the ground and excited states, and the Hamiltonian is the electrical dipole energy associated with the electromagnetic field interacting with the electron:

$$H'(\vec{r}) = -\vec{\mu}_{21} \cdot \vec{E}$$

In a extended crystalline semiconductor material, electrons are delocalized and travel at different wavevectors $\vec{k}$ and energies $E(\vec{k})$. Each semiconductor atom has all of its valence shell filled with covalent bonds. To delocalize, the electrons have to gain energy. This energy is what defines the semiconductor's bandgap. From an optoelectronic perspective, electrons can transition from the conduction band to the valence band and emit photons, or they can transition from the valence band to the conduction band, and absorb a photon (Fig. 2.12). The rate of transitions of electrons in a volume V can thus be summarized using Fermi's Golden rule as well as the Fermi-Dirac statistics to model the thermal energy distribution of the electron gas:

$$\gamma_{v\to c} = \frac{2}{V}\sum_{\vec{k}_v}\sum_{\vec{k}_c}\frac{2\pi}{\hbar} \mid H'_{vc} \mid^2 \delta(E_c(\vec{k}_c) - E_v(\vec{k}_v) - \hbar\omega)f_c(1 - f_v)$$

$$\gamma_{c\to v} = \frac{2}{V}\sum_{\vec{k}_c}\sum_{\vec{k}_v}\frac{2\pi}{\hbar} \mid H'_{vc} \mid^2 \delta(E_v(\vec{k}_v) - E_c(\vec{k}_c) - \hbar\omega)f_v(1 - f_c)$$

$$\gamma_{abs} = \gamma_{v\to c} - \gamma_{c\to v} = \frac{2}{V}\sum_{\vec{k}_c}\sum_{\vec{k}_v}\frac{2\pi}{\hbar} \mid H'_{vc} \mid^2 \delta(E_c(\vec{k}_v) - E_v(\vec{k}_v) - \hbar\omega)(f_v - f_c)$$

20

where the Fermi-Dirac functions f_v and f_c denote the probability of finding an electron or hole at a particular energy and are defined as:

$$f_v = \frac{1}{1 + e^{(E_v - F_v)/kT}} \qquad f_c = \frac{1}{1 + e^{(E_c - F_c)/kT}}$$
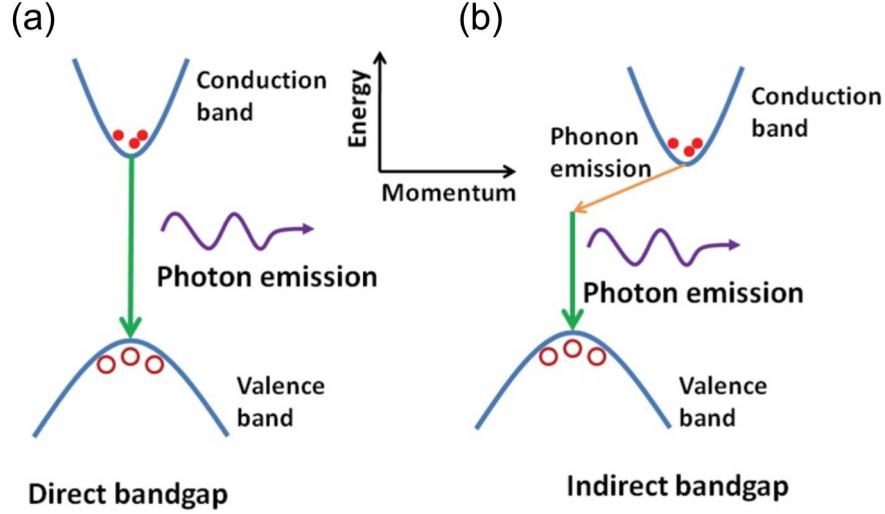
Figure 2.12. (a) A conduction to valence band transition of an electron in a direct bandgap semiconductor that emits a photon. (b) A conduction to valence band transition of an electron in a indirect bandgap semiconductor [55].

In order to sum over all wavevectors of electrons and holes in the conduction and valence band, I first make the approximation that the wavevectors of photons are much smaller than wavevectors of electrons. Thus, an electronic transition is "vertical" with an electron gaining energy amounting to $\hbar\omega$ and no momentum. Mathematically, this approximation is:

$$\sum_{\vec{k}_a} \sum_{\vec{k}_b} = \sum_{\vec{k}_a} \sum_{\vec{k}_b} \delta(\vec{k}_a - \vec{k}_b) = \sum_{\vec{k}}$$

Now, I can convert the sum into an integral in momentum space, where I assume that each wavevector exists in a volume $V = L \times L \times L$ that eventually extends to infinity. Thus, each wavevector now has a volume $(2\pi)^3/V$:

$$\sum_{\vec{k}} = \sum_{\vec{k}} \frac{\Delta \vec{k}}{\Delta \vec{k}} = \frac{V}{(2\pi)^3} \int_{\vec{k}} d^3\vec{k} = \frac{V}{(2\pi)^3} \int_{\vec{k}} k^2 \sin\theta \, dk \, d\theta \, d\phi = \frac{V}{(2\pi)^3} 4\pi \int_k k^2 dk$$

The double sum over wavevectors becomes an integral over momentum space for the absorption rate γ_{abs}:

$$\gamma_{abs} = \frac{2}{V} \sum_{\vec{k}_c} \sum_{\vec{k}_v} \frac{2\pi}{\hbar} \mid H'_{vc} \mid^2 \delta \left(E_c(\vec{k}_v) - E_v(\vec{k}_v) - \hbar\omega \right) (f_v - f_c)$$

$$= \frac{2}{V} \frac{V}{(2\pi)^3} 4\pi \frac{2\pi}{\hbar} \mid H'_{vc} \mid^2 \int_k k^2 dk \delta \left(E_c(\vec{k}_v) - E_v(\vec{k}_v) - \hbar\omega \right) (f_v(k) - f_c(k))$$

21

The dispersion $E(\vec{k})$ for electrons and holes can follow a parabolic approximation taken from quantum mechanics: $E(\vec{k}) = p^2/2m^* = \hbar^2 k^2/2m^*$ where m^* is an effective mass of the electron or hole in the gain material of choice. The δ-function is a function of the dispersion of the valence and conduction band of second degree in the variable k. I can simplify the delta function as follows:

$$\delta\left(E_c(\vec{k}_v) - E_v(\vec{k}_v) - \hbar\omega\right) = \delta\left(E_g + \frac{\hbar^2 k^2}{2m_e^*} + \frac{\hbar^2 k^2}{2m_h^*} - \hbar\omega\right)$$

$$= \delta\left(E_g + \frac{\hbar^2 k^2}{2m_r^* - \hbar\omega}\right) \text{ where } m_r^* = 1/m_e^* + 1/m_h^*$$

Now, $\delta(g(k)) = \sum_{k_i} \delta(k - k_i)/|g'(k_i)|$ so that the delta function simplifies further to:

$$\delta\left(E_g + \frac{\hbar^2 k^2}{2m_r^* - \hbar\omega}\right) = \frac{\delta(k - k_i)}{|g'(k_i)|} = \frac{\delta\left(k - \sqrt{\frac{2m_r^*}{\hbar^2}(\hbar\omega - E_g)}\right)}{\frac{\hbar^2}{m_r^*}\sqrt{\frac{2m_r^*}{\hbar^2}(\hbar\omega - E_g)}}$$

Plugging the δ-function back into the the absorption rate calculation, the general expression for the absorption rate per unit volume in a semiconductor is:

$$\gamma_{abs}(\hbar\omega) = \frac{2}{V}\frac{V}{(2\pi)^3}4\pi\frac{2\pi}{\hbar} \mid H'_{vc} \mid^2 \int_k k^2 dk \frac{\delta(k - k_i)}{\hbar^2 k_i/m_r^*}) \left(f_v(k) - f_c(k)\right)$$

$$= \frac{2\pi}{\hbar}|H'_{vc}|^2 \cdot \frac{1}{2\pi^2}\left(\frac{2m_r^*}{\hbar^2}\right)^{3/2}\sqrt{\hbar\omega - Eg}(f_v - f_c) = \frac{2\pi}{\hbar}|H'_{vc}|^2 \cdot \rho_r(\hbar\omega)(f_v - f_c)$$

Now that the number of photons that are absorbed per unit volume per second has been determined, the absorption coefficient $\alpha(\hbar\omega)$ is found simply by dividing the absorption rate $\gamma_{abs}(\hbar\omega)$ by the photon flux $|\vec{S}| = \vec{E} \times \vec{H}/(\hbar\omega)$ propagating through the material in accordance to equation 2.24:

$$\alpha(\hbar\omega) = \frac{\pi\omega}{nc\epsilon_0}|\hat{e} \cdot \langle 2 \mid q\vec{x} \mid 1\rangle|^2 \cdot \rho_r(\hbar\omega) \cdot (f_v - f_c) \tag{2.25}$$

The absorption of photons in a semiconductor material depends on multiple factors: 1) the dipole matrix element, 2) the reduced density of states ρ_r, and 3) the populations of electrons and holes in the valence and conduction bands. The populations of electrons and holes play an especially critical role in engineering nanolasers because photons can only be absorbed if electrons are in the valence band of the semiconductor. In the conduction band, electrons will recombine with holes and emit photons instead. This process is the opposite of absorption (the absorption rate derived is the *net* absorption rate. The emission of photons from excited electrons can occur as either spontaneous emission of stimulated emission.

2.2.2   Spontaneous and Stimulated Emission

The spontaneous and stimulated emission rates can be calculated by following Einstein's original theory that a material immersed in a thermally-equilibrated photon bath will absorb

and emit light in equal amounts at every photon energy [56]. First, lets define various rates of absorption and emission:

$$R_{abs} = R_{spon} + R_{stim} \text{ where}$$
$$R_{spon} = A_{cv} \cdot f_c(1 - f_v)$$
$$R_{abs} = B_{vc} \cdot f_v(1 - f_c) \cdot n_{ph} \cdot N(\hbar\omega)$$
$$R_{stim} = B_{cv} \cdot f_c(1 - f_v) \cdot n_{ph} \cdot N(\hbar\omega)$$

The absorption and stimulated emission rates are dependent on the presence of photons. Photons follow Bose-Einstein statistics so that the number of photons per state is:

$$n_{ph}(E = \hbar\omega) = \frac{1}{e^{\hbar\omega/kT} - 1}$$

The number of states for any energy E per unit volume per energy interval is also found as:

$$N(E) = \frac{2}{V} \sum_{\vec{k}} \delta(E - \hbar\omega) = 2 \int \frac{k^2 dk d\Omega}{(2\pi^3)} \delta(E - \hbar\omega)$$

$$N(E) = \frac{n^3 E^2}{\pi^2 \hbar c^3}$$

In thermal equilibrium, a closed system (our gain material) will absorb and emit light in equal amounts. Otherwise, it will be gaining or losing energy. Equilibrating the absorption and emission rates, A and B are related:

$$R_{abs} = R_{spon} + R_{stim}$$
$$B_{vc} f_v(1 - f_c) n_{ph}(\hbar\omega) N(\hbar\omega) = A_{cv} f_c(1 - f_v) + B_{cv} f_2(1 - f_1) n_{ph}(\hbar\omega) N(\hbar\omega)$$
$$n_{ph}(\hbar\omega) N(\hbar\omega) = \frac{n^3 E^2}{\pi^2 \hbar c^3} \cdot \frac{1}{e^{\hbar\omega/kT} - 1} = \frac{A_{cv} f_c(1 - f_v)}{B_{vc} e^{\frac{E_c - E_v}{kT}} - B_{cv}}$$
$$\text{so that } B_{cv} = B_{vc} = B \text{ and } \frac{A_{cv}}{B} = N(E) = \frac{n^3 E^2}{\pi^2 \hbar c^3}$$

One fundmental insight from this simple analysis is that absorption and stimulated emission are essentially symmetric processes. In absorption, a previously existing photon causes an electron to transition to an excited state and destroys the photon. In stimulated emission, a previously existing photon causes an electron to transition to the ground state and creates another photon. Spontaneous emission, in this case, occurs without the presense of a photon, and so is different from the other two phenomenon. We can find the ratio of spontaneous to stimulated emission in the material:

$$\frac{R_{stim}}{R_{spon}} = \frac{B \cdot f_c(1 - f_v) \cdot n_{ph} \cdot N(\hbar\omega)}{A_{cv} \cdot f_c(1 - f_v)}$$
$$= n_{ph} = \frac{1}{e^{\hbar\omega/kT} - 1}$$

To find the absolute magnitude of the spontaneous (and stimulated) emission rates, the newly found A and B coefficients can be related to the previously derived absorption

coefficient that was found via Fermi's Golden Rule, keeping in mind that absorption and stimulated emission are symmetric processes:

$$R_{net} = r_{net}dE = R_{abs} - R_{stim} = B(f_v - f_c)n_{ph}N(\hbar\omega)$$

$$R_{spon} = r_{spon}dE = A_{cv}f_c(1 - f_v)$$

$$\alpha(\hbar\omega)dE = \frac{r_{net}dE}{n_{ph}N(\hbar\omega)(n_r/c)} = \frac{n_r}{c}B(f_v - f_c)$$

$$\frac{r_{spon}(\hbar\omega)}{\alpha(\hbar\omega)} = \frac{A_{cv}}{B}\frac{f_c(1 - f_v)}{f_v - f_c}\frac{c}{n_r}$$

$$r_{spon}(\hbar\omega) = \frac{n^3(\hbar\omega)^2}{\pi^2\hbar c^3}\frac{1}{e^{\frac{\hbar\omega - \Delta F}{kT}} - 1}\alpha(\hbar\omega)$$

where ΔF is $F_c - F_v$ where F_c is the average energy of electrons and F_v is the average energy of holes. Therefore, the spontaneous emission rate is dependent on the photon energy, the Fermi-level splitting of electron and hole energies, and the absorption coefficient.

In summary, absorption, spontaneous emission, and stimulated emission are all interrelated light-matter interactions. The absorption coefficient of a material can be derived by first principles by Fermi's Golden Rule. Stimulated emission is the symmetric process to absorption, and thus the total rates of stimulated emission and absorption depend only on the populations of electrons and holes in the material, and the intrinsic rate (B) is the same. Spontaneous emission is related to absorption as shown above. Usually, the spontaneous emission rate is expressed as a lifetime, and in semiconductors, this lifetime is $\tau_{sp} \approx 1$ ns. The stimulated emission rate, therefore, is faster by the number of photons present in the cavity. Thus, if the spontaneous emission lifetime is $\tau_{sp} = 1$ ns and there are 10 photons in the semiconductor, than the stimulated emission rate will be $\tau_{stim} = 0.1$ ns.

2.2.3   Examples of Gain Media

In most cases, when a photon is absorbed by a material, the electronic excitation is degraded rapidly to heat in less than 1 picosecond. However, in optoelectronically active materials, the excited electronic state can persist for upwards of 1 nanosecond when spontaneous emission can occur. There are several broad categories of materials that will emit light. The only requirement for light absorption and generation is the presence of separated quantum energy levels that allow electrons to transition between them through light interaction (as opposed to nonradiative decay paths). Rare earth elements implanted in crystals or glasses, gases with high-lifetime transitions, molecules with strong dipole moments, and semiconductors are all discovered gain materials to date. Dye molecules and semiconductors are the most promising gain media for nanolasers, so they will be discussed in more detail.

Dye Molecules

Single-molecule dyes function by absorbing light at one wavelength (or energy), and releasing all or part of that energy as another photon of equal or lesser energy. The loss of photon energy is converted to vibrational energy for the molecule, and thus energy is still conserved. Because the absorption and emission of light from dye-molecules involves both electronic and vibrational states, we call the process a *vibronic* transition. In Fig. 2.13, we show how such transitions occur with a simple molecule with two electronic states and multiple vibrational states in between the two electronic states. The absorption of a photon will change the electronic configuration of the molecule so that the nuclear coordinates will shift away from their equilibrium positions (i.e. when the molecule is in its vibrational ground state). However, this absorption process will only happen if the shift in nuclei due to the photon absorption is compatible with the positions and momenta of an existing vibrational mode of the molecule. The selection rules associated with how photonic and vibrational transitions occer is known as the Franck-Condon principle [57]. Once the photon is absorbed, the vibrations decay in the excited electronic state, where a photon is then released, causing vibration in the ground electronic state (which then decays quickly as well).
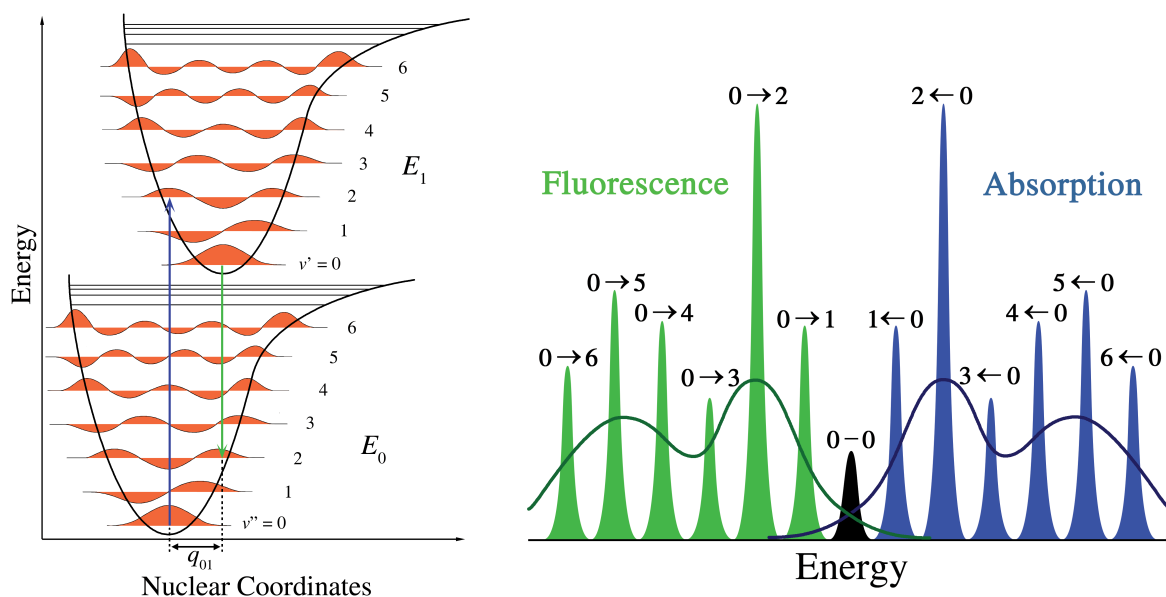
Figure 2.13. A graphical illustration of the Franck-Condon effect

The absorption of a photon by a dye molecule can be characterized by the molecules cross-section σ to incoming radiation. Thus, if an infinite plane wave were to strike the molecule, the cross-section of the molecule would explain how much power (W) was absorbed by the relation $P = \sigma \vec{E} \times \vec{H}$. The cross section $\sigma(\hbar\omega)$ is closely related to the absorption coeffcient by $\alpha(\hbar\omega) = N\sigma(\hbar\omega)$ where N is the number of molecules per unit volume (cm^{-3}). Thus, the amount of gain that a certain dye-doped material has can be easily engineered by varying the concentration of dye in the carrier material. For example, Oregon Green 488, the dye used in a recent nanolaser demonstration [40], has a absorption cross-section $\sigma_{abs} = 2.55 \times 10^{-16}$

cm^{-2}. The group was able to achieve laser oscillations with roughly 2700 dye molecules in a gain media volume of 2.9×10^4 nm^3 to acheive a gain of $-\alpha = 24000$ cm^{-1}!

Unfortunately, there are some major disadvantages of using dyes for gain media that have yet to be overcome. Firstly, most strongly fluorescing dyes eventually are destroyed by photobleaching. When a fluorophore absorbs a photon, its electronic configuration changes from a stable ground state to an unstable excited state. In this excited state, the molecule can interact with its surroundings. This interaction can lead to chemical reactions that destroy the molecule and thus reduces total fluorescence from the material. For example, Oregon Green 488 loses 60% of its fluorescense after exposure to an excitation light source for 1 minute [58]. Also, it is difficult to excite these molecules by electrically driving them. In semiconductor laser diodes, semiconductors can easily emit light by electroluminescence. Such behavior is extremeley difficult to engineer efficiently in dye-based media. Thus, at this time, the only dye-based lasers in use require external light sources and continuously flowing dye in the cavity. In the nanoscale, such engineering is prohibitive.

Semiconductors

Crystalline semiconductors are characterized by having conductivities in the range of $\sigma = 10^3$ S/cm to $\sigma = 10^{-8}$ S/cm. For laser applications, however, the important point is to understand which semiconductors can absorb and *emit* light efficiently. Like all crystals, the periodic arrangement of atoms in a lattice has significant consequences for the behavior of electrons in the lattice, especially valence electrons that take part in crystalline covalent bonds. From the perspective of Schrödinger's equation:

$$H\Psi(\vec{r}) = \left[\frac{\hbar^2}{2m_0}\nabla^2 + V(\vec{r}) \right] \Psi(\vec{r}) = E(\vec{k})\Psi(\vec{r})$$

$$V(\vec{r}) = V(\vec{r} + \vec{R})$$

where $\vec{R}$ is a lattice vector, delocalized electrons and holes are travelling throughout a periodic lattice. In this case, Bloch's theorem states that the wavefunction for electrons and holes are given by the general solution

$$\Psi_{p\vec{k}}(\vec{r}) = e^{i\vec{k}\cdot\vec{r}}u_{p\vec{k}}(\vec{r})$$

$$u_{p\vec{k}}(\vec{r}) = u_{p\vec{k}}(\vec{r} + \vec{R})$$

These wavefunctions are characterized by different energy bands p in which electrons can reside and wavevectors $\vec{k}$ that they possess. Each electron and hole also has a certain energy $E = E(p, \vec{k})$ that is also dependent on which band and what wavevector a particular carrier has. This energy-wavevector relationship determines the dispersion of the electrons in the semiconductor. In freespace, the kinetic energy of a particle is determined simply by $E = p^2/2m_0 = \hbar^2 k^2/2m_0$. In a semiconductor, the mass of the electron at a particular

wavevector can be modified to obtain a similar relationship:

$$E = \frac{\hbar^2 k^2}{2m^*}$$

$$m^* = \hbar^2 \cdot \left[\frac{d^2 E(\vec{k})}{d\vec{k}^2} \right]^{-1}$$

where m^* is the effective mass of a carrier in the material. In this effective mass approximation, the disperion $E(p, \vec{k})$ is parabolic, and so m^* is a constant within a reasonable range of $\vec{k}$ values.
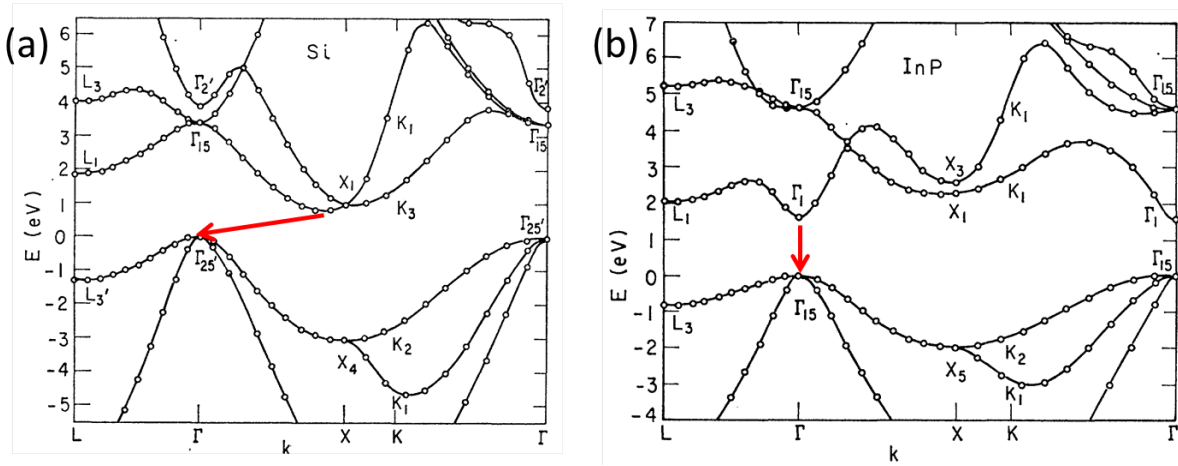
Figure 2.14. (a) A plot of the band structure of silicon. The red arrow represents a conduction band to valence band transition of an electron. A necessary change in both energy and momentum is needed to make the transition. Thus, this transition must be phonon-assisted. (b) A plot of the band structure of indium phosphide. The red arrow represents a conduction band to valence band transition of an electron. This process can occur efficiently with the absorption or emission of a photon [59]

In Fig. 2.14, I show the bandstructure for silicon and indium phosphide (InP). This band structure summarizes the energy-wavevector dispersion for electrons and holes in various bands. In silicon, the L_3' band represents the highest occupied valence band, whilre the L_1 band represents the lowest unoccupied conduction band. Thus, the L_3' and L_1 bands represent the two quantum states from which optical absorptiona and emission can occur. Yet, relative to the wavevectors associated with electrons, photons have much less momentum. Thus, a photon absorption or emission event can be represented as a vertical transition in Fig. 2.14. In silicon, unfortunately, the smallest energy transition also requires substantial momentum, so that an absorption or emission event can only happen if additional momentum is provided by another source (such as a phonon). Thus, absorption and emission of radiation is very inefficient in silicon due to this "indirect gap".

In contrast, indium phosphide (and most other compound semiconductors made with group III and group V elements) have a "direct gap." Thus, vertical photon absorption and

emission transitions take place between L_3 and the L_1 bands. Since no additional momentum is necessary, these transitions happen very efficiently. Compound III-V semiconductors are therefore some of the most useful gain materials for nanolaser applications.

The best method for understanding the potential usefulness of a direct-gap semiconductor is to compare the absorption coefficient $\alpha(\hbar\omega)$. Since absorption and stimulated emission are symmetric processes, a material that possesses strong absorption will also strongly amplify light when the population of carriers are inverted so that all carriers are in their excited states.
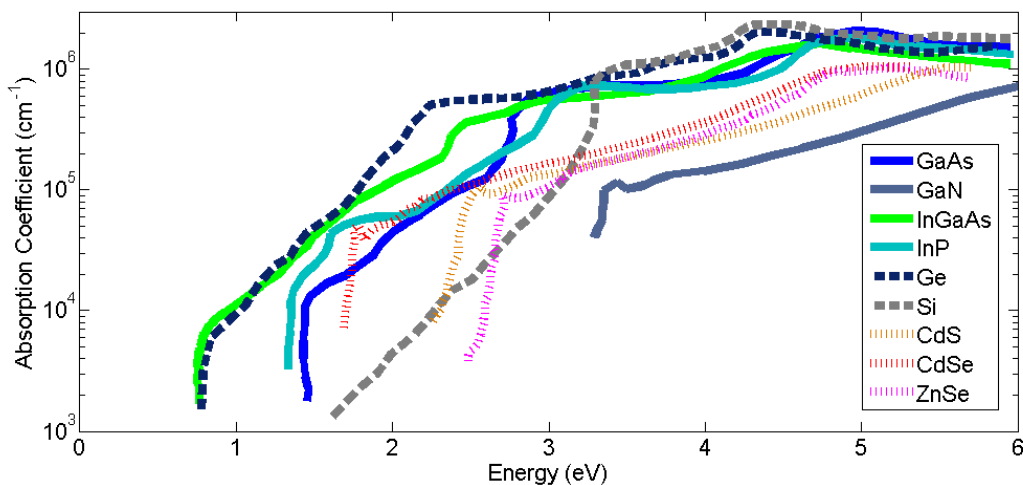
Figure 2.15. A plot of absorption coefficients for various III-V, Group IV, and II-VI semiconductors. The group IV semiconductors (long dashed lines) have indirect bandgaps, making them poor absorbers and emitters of light. III-V semiconductors (solid lines), on the other hand, have reasonable absorption properties and direct bandgaps. Semiconductors made of II-VI materials (short dashed lines) have very strong absorption, but are difficult to grow [60–65].

In Fig 2.15, I present the absorption coefficient of various Group IV, III-V, and II-VI semiconductor crystals. Since the ability of the material to absorb light is directly related to its ability to provide light amplification, understanding this basic material property is critical to developing successful nanolasers. Group IV elements, although great semiconductors for electronic properties, have indirect bandgaps. Thus, the ability of silicon and germanium to absorb light efficiently is low, and thus they are useful for only passive optical components (thus far). Materials made out of group III and group V elements have direct bandgaps, and can reach absorption coefficients of 10^4 cm^{-1}. They are also well understood in the context of current laser technology and easily grown. Semiconductors made of II-VI compounds have even better absorption characteristics. Very close to the bandgap energy, these materials can achieve absorption coefficients of $3 - 7 \times 10^5$ cm^{-1}. Such strong absorption is preferential for nanolaser design, but the technology to grow these materials reliably in double-heterostructure configurations is still in development. Thus, in this work,

III-V semiconductors were used as a technologically robust material platform from which experimentation with nanolaser design could reliably be performed.

Chapter 3

Nanocavity Design and Examples

Designing nanolasers is in many ways not different from standard laser design. Any laser needs 1) a cavity that can trap light for extended periods of time to increase the effects of stimulated emission, and 2) a gain media that can amplify light sufficiently to overcome inefficient losses within the cavity and radiation losses of photons escaping the cavity.

Of course, the novel aspects of nanolasers are also numerous. Can an optical cavity be designed to confine light within a volume that is smaller than the diffraction limit? Are there gain materials that can provide the necessary amplification to sustain laser oscillations in such a small cavity? In this section, some basic limits on nanolasers will be explored. These limits will help us to understand the opportunities and challenges in developing subwavelength light sources.

3.1 Nanolaser Design Considerations

3.1.1 Device Considerations

In order to understand nanolasers, we must first understand traditional lasers where the electromagnetic energy is not confined below the diffraction limit. In the case of a traditional Fabry-Pèrot cavity as seen in Fig. 3.1, the laser consists of two mirrors (the left one is 100% reflective, while the right one is partially reflective), and a semiconductor gain medium that has achieved population inversion by current injection. As light travels through the semiconductor from the left mirror to the right mirror, it gets amplified by a factor $e^{-\alpha L}$. At this mirror, it loses some light, so that the reflected light's intensity is $r_1 e^{-\alpha L}$. It propagates again through the gain media, getting amplified so that at the left mirror, the light intensity is $r_1 e^{-\alpha L} e^{-\alpha L}$. Finally, there is some light loss at the back mirror as well (although small).

Thus, in one round trip, the light intensity has been changed by a factor of $r_1 e^{-\alpha L} r_2 e^{-\alpha L}$. For the light generation to be self-sustaining, the original intensity must equal the final intensity after one roundtrip. Thus, we come to an expression to describe the threshold gain needed to produce laser oscillations:

$$g_{th} = -\alpha_{th} = \frac{1}{2L} \ln \left(\frac{1}{r_1 r_2} \right) \tag{3.1}$$
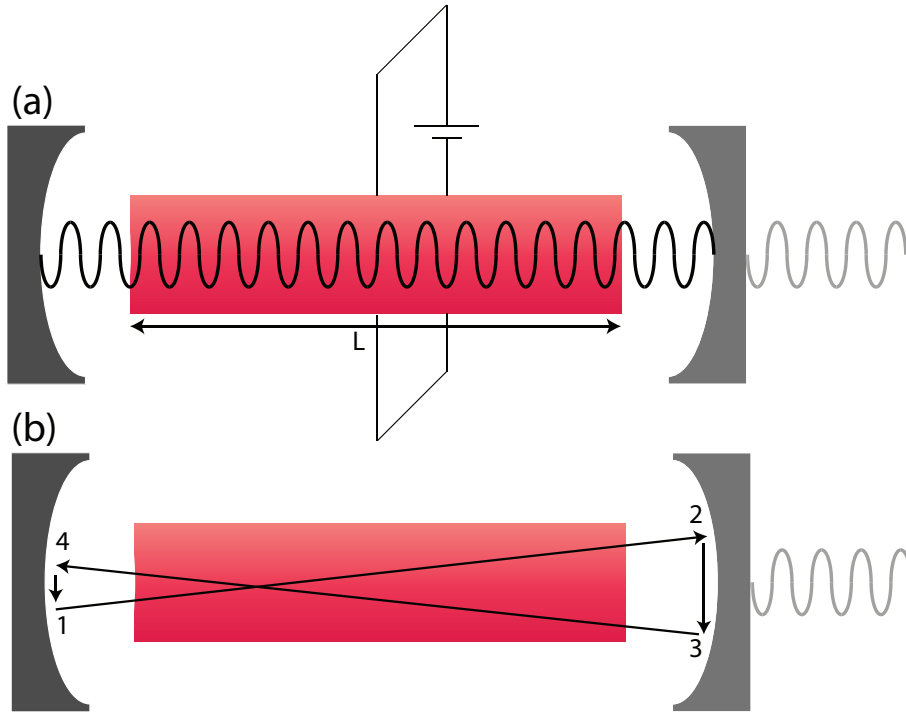
Figure 3.1. (a) A schematic of a Fabry-Pèrot cavity laser. The laser consists of a semiconductor diode that acts as a gain material, and two mirrors on the two ends of the semiconductor. In practice, the edge of the laser chip serves as a mirror since the semiconductor can be cleaved to produce atomically smooth surfaces. (b) A simplified version of the movement of light within a laser cavity. As the light makes a round trip through the cavity, it gets amplified through the semiconductor, and attenuated at the mirrors as some light escapes the cavity. In one round trip, the light intensity must by equal for the laser to be self-sustaining.

As lasers shrink to the nanoscale, it becomes difficult to understand exactly where there are reflections in the cavity, and how light is lost. Thus, the threshold amplification needed to produce laser oscillations becomes unclear when applied to Eq.(3.1). Therefore, in order to better understand the nature of a nanocavity, we drop our focus of the need to maintain constant intensity after a single trip through the cavity. Instead, we focus on the need to maintain a constant intensity in the cavity at all times (for steady-state operation). In other

words, the rate of photon generation must equal the photon loss rate:

$$\gamma_{gen} = \gamma_{loss}$$

$$\gamma_{gen} = \frac{1}{\tau_{ph}}$$

$$\Gamma \frac{c}{n_{eff}} g_{th} = \frac{\omega_0}{Q_0}$$

where τ_{ph} is the photon lifetime in the cavity, c is the speed of light, n_{eff} is the effective refractive index of the electromagnetic mode, g_{th} is the threshold gain, ω_0 is the laser frequency, Q_0 is the cold quality factor of the cavity, and Γ is the confinement factor, or the fraction of the electromagnetic mode's energy that is inside the gain medium. Using this time-based approach to photon-balance within a cavity, the threshold gain can be written as:

$$g_{th} = \frac{1}{\Gamma} \frac{\omega_0}{Q_0} \frac{n_{eff}}{c} \tag{3.2}$$

Now, since the absorption of semiconductors shown in Fig. 2.15 shows that III-V semiconductors have $\alpha_{max} \sim 5000$ cm^{-1}, nanolaser designs must have cavity quality factors of at least $Q_0 = 30$. Since getting full inversion of carriers is also not possible at room temperature, practical limits will suggest that these nanocavities will need to have quality factors closer to $Q_0 = 100$ or higher.

In order to achieve these quality factors, it is important to find all of the potential loss mechanism for both carriers and electromagnetic energy. For example, carriers can be lost by spontaneous emission, stimulated emission, surface recombination, Auger recombination, etc. Electromagnetic energy will be lost by useful laser radiation and inefficient energy loss due to metal ohmic resistance. The loss of carriers will result in a degradation in the potential gain that the semiconductor can provide. The electromagnetic energy loss can be further quantified in the design of nanolasers. The total quality factor Q_o can be also written as:

$$\frac{1}{Q_0} = \frac{1}{Q_{rad}} + \frac{1}{Q_{ohmic}} \tag{3.3}$$

The radiation quality factor, Q_{rad}, can be engineered by properly designing the nanocavity. The ohmic loss quality factor, Q_{ohmic}, can also be engineered by keeping the electromagnetic mode away from metal. However, as the electromagnetic energy interacts less with metal, the nanolaser size will necessarily get larger due to the intrinsic loss vs. confinement tradeoff present in metal optics. Thus, a "worst case scenario" would occur when all of the electromagnetic energy were to reside in the metal. In this case, we can find a quality factor Q_{metal} that is purely material dependent. Following the work of Conway [66]:

$$Q_{metal} = \frac{\omega U_e}{dU_e/dt}$$

$$= \frac{\frac{1}{2} \int_{metal} \frac{\partial(\omega\epsilon')}{\partial\omega} E^2 dV}{\int_{metal} \epsilon'' E^2 dV}$$

$$= \frac{\frac{\partial(\omega\epsilon')}{\partial\omega}}{2\epsilon''}$$

The ohmic loss Q_{ohmic} will then simply become $Q_{ohmic} = Q_{metal}/\Gamma_{metal}$ where Γ_{metal} is the fraction of electromagnetic mode energy in the metallic area. In Fig. 3.2, I show Q_{metal} for various metals that are useful for metal-optics. Thus, a good metal-based nanocavity will try to mitigate the electromagnetic field penetration into metal (until metals are engineered to be much less lossy).
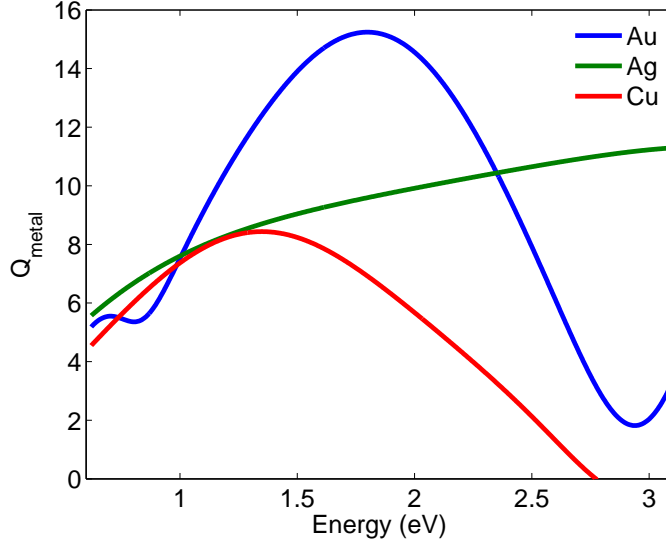
Figure 3.2. A plot of various material dependent quality factors Q_{metal} for good conductors [52, 53]. Gold seems to be the best material with quality factors as high as $Q_{metal} = 15$.

3.1.2 System-level Considerations

Another consideration for nanolaser design comes from a systems design perspective. Miller [15] has noted that optical transmitters must consume < 10 fJ/bit of energy in order to be viable for on-chip computer interconnect applications. In order to achieve such low energy consumption, the total active volume of the laser must be scaled down significantly. A simple but useful metric can be found by balancing the amount of power going into a laser and the amount of carrier recombination happening (the generation of carriers must equal the recombination of carriers in steady state):

$$\frac{I}{qV} = \frac{N_{th}}{\tau} \tag{3.4}$$

where I is the current into the laser, q is the unit charge, V is the laser's active volume, N_th is the carrier concentration at when the laser is at its lasing threshold, and τ is the recombination lifetime of carriers in the semiconductor.

In order to find the largest possible laser volume that would allow 10 fJ/bit laser operation, the laser will have to dissipate a maximum power $P = IV$. If the voltage drop

of the semiconductor laser is simply the bandgap energy of the semiconductor ($V \sim 1$ volt), we need to find I such that there is 10 fJ/bit efficiency. A typical laser may operate at roughly 10 Gbit/sec, so that the total allowed power dissipation of the device is $10\frac{\text{fJ}}{\text{bit}} \cdot 10 \times 10^9 \frac{\text{bits}}{\text{sec}} = 100\mu\text{W}$. Therefore, the maximum current allowed for laser operation is $I = 100\mu\text{A}$.

The threshold carrier concentration of the laser will depend strongly on the amount of gain needed to operate the device. The amount of gain, in turn, will depend on the quality factor of the nanocavity. If I assume a logarithmic gain model for InGaAs, the threshold carrier concentration for lasing is:

$$g_{th}(N) = g_0 \ln(\frac{N}{N_{tr}})$$

$$g_{th} = \frac{1}{\Gamma}\frac{\omega}{Q}\frac{n}{c}$$

$$N_{th} = N_{tr}e^{g_{th}/g_0}$$

$$N_{th} = N_{tr}e^{\frac{1}{\Gamma}\frac{\omega}{Q}\frac{n}{c}/g_0}$$
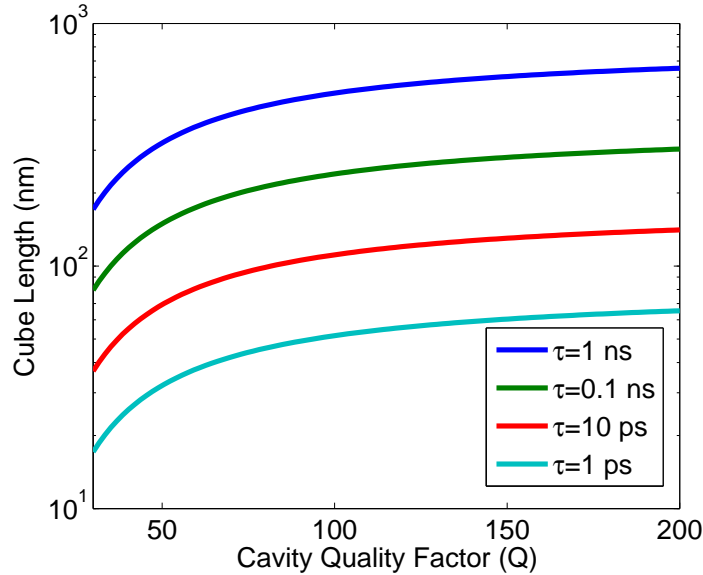
Figure 3.3. A plot of the maximum size of a semiconductor cube for a nanocavity laser that operates at 10 fJ/bit energy usage. The laser size varies with the quality factor achieved by the cavity as well as the carrier recombination lifetime achieved.

Finally, the carrier lifetime for the laser cavity is determined by the various recombination mechanisms present before the laser threshold condition is reached. The major recombination mechanisms for nanolasers will most likely result from spontaneous emission, Purcell-enhanced spontaneous emission, surface recombination, and Auger recombination. There may also be some Schockley-Reed-Hall recombination if there are a lot of mid-gap

defects in the semiconductor. Thus, the lifetime can be represented as:

$$\frac{1}{\tau} = \frac{F\beta}{\tau_{sp}} + \frac{(1-\beta)}{\tau_{sp}} + v_s\frac{S_a}{V} + \frac{1}{\tau_{aug}}$$

where τ_{sp} is the spontaneous emission lifetime, $F = \frac{2}{\pi^2}\frac{Q}{V}\frac{\lambda_0}{2n}^3$ is the Purcell enhanement factor (see below), β is the probability that spontaneous emission will couple to the cavity mode, v_s is the surface recombination velocity, S_a is the surface area of the laser, and τ_{aug} is the Auger recombination lifetime. Since many of these lifetimes are difficult to measure or calculate, τ will be treated as a parameter when trying to determine the maximum size the nanolaser can be to achieve 10 fJ/bit operation.

With this complete (yet simplified) model of the carrier dynamics inside a laser, the maximum size of the laser can be determined for various quality factor cavities as well as various predicted carrier lifetimes. The maximum length of a semiconductor cube given a quality factor and carrier lifetime is shown in Fig. 3.3. An important distinction to make is that the volume calculated relates only to the active gain volume. Ideally, active semiconductor would only be present where there is large overlap with the cavity eigenmode, yet in many cases, practical limitations do not allow such selective placement. This is an area for further research.

3.1.3 Carrier Dynamics and the Purcell Effect

One extremely interesting phenomenon that occurs only in nanoscale light cavities is traditionally termed the Purcell effect [67]. In brief, Purcell originally theorized that the spontaneous emission rate of a material could be modified by changing the electromagnetic environment into which the material was radiating. Recently, there has been interest in harnessing the fast spontaneous emission speeds in lasers to create so-called thresholdless lasing [68].

There are many ways to change the electromagnetic surroundings of a spontaneous emitter. For example, if we consider the radiation rate of an atom into a homogeneous media, than the spontaneous emission rate is:

$$\gamma_{spon} = \frac{nq\omega^3|x_{12}|^2}{3\pi\epsilon_0\hbar c^3} \tag{3.5}$$

where ω is the emission frequency, n is the refractive index of the homogeneous material, x_{12} is the dipole transition matrix element, and c is the speed of light. Notice that in this case, a dipole in a semiconductor medium with $n = 3.5$ will have a spontaneous emission radiation rate 3.5 times higher than the same dipole in air! Thus, by changing the refractive index, we have modified the environment the dipole is in (i.e. the density of states of photons into which a dipole can radiation into).

In a nanocavity, often times there may only be one electromagnetic state into which a dipole can radiate. The spontaneous emissin rate into a single electromagnetic mode with a

energy bandwidth $\hbar\Delta\omega$ can be calculated with Fermi's Golden rule:

$$\frac{1}{\tau_{spon}} = \frac{2\pi}{\hbar}|q\vec{x}_{12} \cdot \vec{E}_{max}|^2\frac{dN}{dE}$$

$$= \frac{2\pi}{\hbar}|q\vec{x}_{12} \cdot \vec{E}_{max}|^2\frac{1}{\hbar\omega}$$

where E_{max} is the electric field present inside the cavity to excite spontaneous emission and $dN/dE = 1/\hbar\omega$ is the density of electromagnetic states in a nanocavity with one mode with a finite linewidth.

The zero-point electric field which excites spontaneous emission necessarily carries an energy of $\hbar\omega/2$. Therefore, the electric field in the cavity E_{max} can be found by relating it to the zero-point electric field present in the cavity:

$$\int \epsilon_0 E^2 dV = \frac{\hbar\omega}{2}$$

If we define a effective mode volume:

$$V_{eff} = \frac{\int \epsilon_0 E^2 dV}{\epsilon_0 E_{max}^2} \tag{3.6}$$

than we can solve for the electric field that excites the spontaneous emission in the material in terms of the photon energy associated with the electromagnetic resonance in the cavity and the effective mode volume of the same resonance:

$$E_{max}^2 = \frac{\int \epsilon_0 E^2 dV}{\epsilon_0 V_{eff}} = \frac{\hbar\omega}{2\epsilon_0 V_{eff}}$$

Now that the density of photonic states and the electric field amplitude are known, I solve for the spontaneous emission rate of a material in a nanocavity:

$$\frac{1}{\tau_{spon}} = \frac{2\pi}{\hbar}|q\vec{x}_{12} \cdot \vec{E}_{max}|^2\frac{1}{\hbar\omega}$$

$$= \frac{\pi}{\hbar\epsilon_0}|qx_{12}|^2\frac{Q}{V_{eff}}$$

If we compare the rate of spontaneous emission into free space versus into a nanocavity, then the Purcell enhancement F to the spontaneous emission is:

$$F = \frac{3}{8\pi}Q\frac{\lambda^3}{V_{eff}} \tag{3.7}$$

This derived Purcell factor differs from the original by a factor of $\pi/2$, but that is probably due to the definition of the mode volume that I used in the derivation.

The Purcell enhancement can have a large affect on the carrier dynamics of lasers [29]. For example, with a faster spontaneous emission rate, the carriers recombine faster so that

more current is needed to reach the laser threshold condition. To fully understand the total implications of enhanced spontaneous emission, lets first write rate equations for carriers and photons in a nanocavity light emitter:

$$\frac{dN}{dt} = P - g(N)S - F\beta\frac{N}{\tau_{sp0}} - (1-\beta)\frac{N}{\tau_{sp0}} - \frac{N}{\tau_{nr}} \tag{3.8}$$

$$\frac{dS}{dt} = \Gamma g(N)S - \frac{S}{\tau_{ph}} + \Gamma F\beta\frac{N}{\tau_{sp}} \tag{3.9}$$

where N is the carrier concentration in the cavity, S is the number of photons in the cavity, P is the pump rate, $g(N)$ is the gain in the semiconductor as a function of carrier concentration, F is the Purcell enhancement factor, β is the fraction of spontaneous emission that couples to the nanocavity, τ_{sp0} is the free-space spontaneous emission lifetime, Γ is the modal confinement factor, and τ_{nr} is the non-radiative recombination lifetime. The details of the rate equation model are given elsewhere [29].
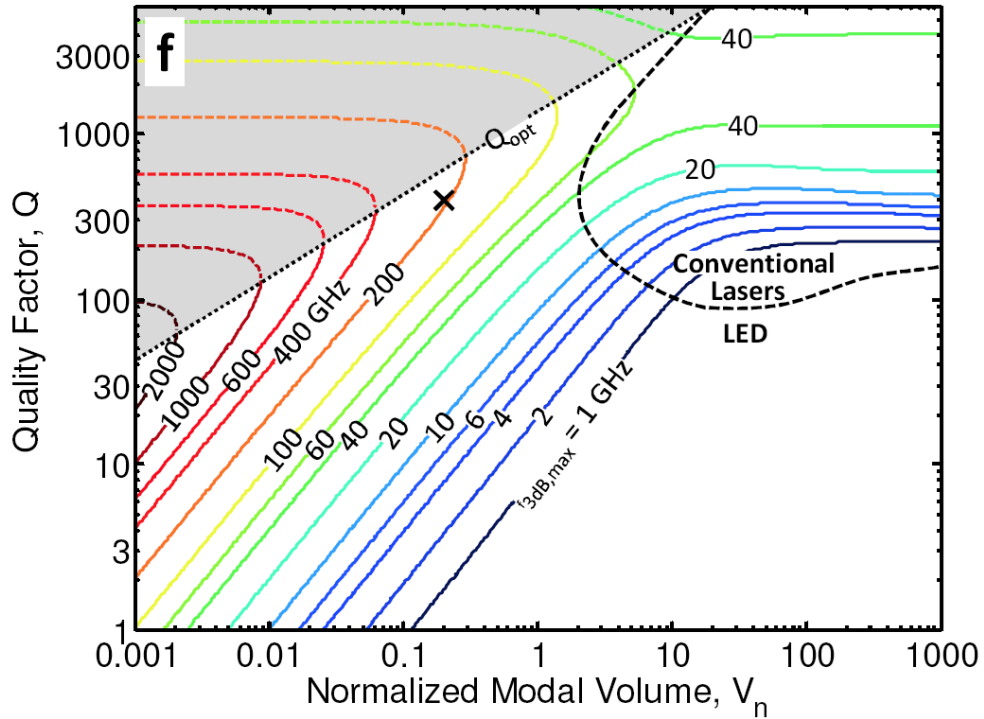
Figure 3.4. A contour plot of maximum achievable bandwidth through a nano-LED design involving the speed-up of spontaneous emission via a nanocavity. The strong coupling regime is shown in gray, while the regime of conventional lasing is shown to have lower modulation speeds than nano-LEDs [29].

A major result of this carrier dynamics analysis is that the modulation speeds of nanocavity light emitters can be dramatically increased by fast spontaneous emission, provided that the cavity does not reach laser threshold. In Fig. 3.4, the modulation bandwidths of various nanocavity designs with quality factor Q and mode volume V_{eff} are shown. It turns out that the modulation bandwidth is influenced more by the effective mode volume of the

cavity rather than the quality factor. This results because with higher quality factor, the photon lifetime also increases so that a modulated photon loses the ability to escape from the cavity. Counterintuitively, for high modulation bandwidths, the nanocavity must be designed with a moderate quality factor, as small an electromagnetic mode volume as possible, and subthreshold biasing during operation.

The drawback of this approach to modulation is that the output light is no longer monochromatic. Monochromicity, of course, can be very advantageous for any communication purpose where multiple channels are desired. Thus, for lasers, this Purcell-enhanced spontaneous emission may be useful to create devices with no threshold, but will not increase modulation bandwidths. Furthermore, the fast spontaneous emission will blur the lines between coherent and incoherent light output from the device. The true benefits of spontaneous emission enhancement for lasers is still a heavy subject of research [50, 68].

3.1.4 Size Limits on Surface Plasmon Nanocavities

Surface plasmon based nanocavities, as we saw in Chapter 2, are interesting since SPPs are more compact than photons. To find the theoretical mode volume of a nanolaser that confines energy to the diffraction limit of a single-sided surface plasmon, I will analytically solve for the mode volume over a standing surface wave that is $(\lambda_{sp}/2)^2$ in area. The mode volume is defined again as:

$$V_{eff} = \frac{\int \frac{\partial \omega \epsilon(\vec{r})}{\partial \omega} |\vec{E}|^2(\vec{r}) dV}{\max\left(\epsilon(\vec{r})|\vec{E}|^2(\vec{r})\right)} \tag{3.10}$$

To start, the electrical energy density of an SPP can be determined from the original electric field profiles:

$$\vec{E}_d = \left(\frac{ik_2' - k_2''}{\omega \epsilon_0 \epsilon_s}\hat{x} - \frac{\beta' + i\beta}{\omega \epsilon_0 \epsilon_s}\hat{z}\right) \cdot e^{i(\beta' + i\beta'')x} e^{-(k_2' + ik_2'')z} \qquad z > 0 \tag{3.11}$$

$$\vec{E}_m = \left(\frac{-ik_1' + k_1''}{\omega \epsilon_0 (\epsilon_m' + i\epsilon_m'')}\hat{x} - \frac{\beta' + i\beta''}{\omega \epsilon_0 (\epsilon_m' + i\epsilon_m'')}\hat{z}\right) \cdot e^{i(\beta' + i\beta'')x} e^{(k_1' + ik_1'')z} \qquad z < 0 \tag{3.12}$$

where E_d is the electric field in the dielectric and E_m is the electric field in the metal.

Using these electric field profiles, the total electrical energy is:

$$\vec{E}_d \cdot \vec{E}_d^* = \frac{1}{(\omega \epsilon_0 \epsilon_s)^2}\left(|k_2|^2 + |\beta|^2\right) e^{-2k_2'z - 2\beta''x} \qquad z > 0 \tag{3.13}$$

$$\vec{E}_m \cdot \vec{E}_m^* = \frac{1}{(\omega \epsilon_0 \epsilon_m)^2}\left(|k_1|^2 + |\beta|^2\right) e^{2k_1'z - 2\beta''x} \qquad z < 0 \tag{3.14}$$

$$U_d = \int \frac{1}{4}\epsilon|\vec{E}|^2 dV = \frac{\lambda_0^2}{16\pi^2 c^2 \epsilon_0 \epsilon_s}\left(|k_2|^2 + |\beta|^2\right) \int_0^\infty \int_0^{\frac{\pi}{\beta'}} \int_0^{\frac{\pi}{\beta'}} e^{-2k_2'z} e^{-2\beta''x} dx\,dy\,dz$$

so that the energy in the dielectric (U_d) and metal (U_m) are:

$$U_1 = \frac{\lambda_0^2}{64\pi^2 c^2 \epsilon_0 \epsilon_s} \frac{1}{\beta'\beta''k_2'} \left(|k_2|^2 + |\beta|^2 \right) \left(1 - e^{-\frac{2\pi\beta''}{\beta'}} \right)$$

$$U_2 = \frac{\epsilon_{md}\lambda_0^2}{64\pi^2 c^2 \epsilon_0 |\epsilon_m|^2} \frac{1}{\beta'\beta''k_1'} \left(|k_1|^2 + |\beta|^2 \right) \left(1 - e^{-\frac{2\pi\beta''}{\beta'}} \right)$$

and the total energy in a area of $(\lambda_{sp}/2)^2$ is:

$$U = U_1 + U_2 = \frac{\lambda_0^2}{64\pi^2 c^2 \epsilon_0} \frac{1}{\beta'\beta''} \left(1 - e^{-\frac{2\pi\beta''}{\beta'}} \right) \left(\frac{1}{\epsilon_s k_2'} \left(|k_2|^2 + |\beta|^2 \right) + \frac{\epsilon_{md}}{|\epsilon_m|^2 k_1'} \left(|k_1|^2 + |\beta|^2 \right) \right)$$
$$(3.15)$$

After finding the total energy in $(\lambda_{sp}/2)^2$, we must find the highest energy density that a dipole in the semiconductor can experience. We focus on the highest energy density in the semiconductor only because radiating dipoles for nanolaser applications can only exist in the semiconductor, and thus the effective mode volume of the cavity will be determined by the field experienced by such radiating dipoles.:

$$u_{max} = \max \left(\frac{1}{4} \epsilon |\vec{E}|^2 \right) = \frac{\lambda_0^2}{16\pi^2 c^2 \epsilon_0 \epsilon_s} \left(|k_2|^2 + |\beta|^2 \right) \tag{3.16}$$

so that the effective mode volume V_{eff} is:

$$V_{eff} = \frac{\epsilon_s \pi}{4} \frac{1}{\beta'\beta''} \left(1 - e^{-\frac{2\pi\beta''}{\beta'}} \right) \left(\frac{1}{\epsilon_s k_2'} + \frac{\epsilon_{md}}{|\epsilon_m|^2 k_1'} \frac{(|k_1|^2 + |\beta|^2)}{(|k_2|^2 + |\beta|^2)} \right) \tag{3.17}$$

Normalizing the effective mode volume by a factor of $(\lambda_0/2n)^3$:

$$V_n = \frac{V_{eff}}{\left(\frac{\lambda_0}{2n}\right)^3} = \frac{2\pi\epsilon_s^{5/2}}{\lambda_0^3} \frac{1}{\beta'\beta''} \left(1 - e^{-\frac{2\pi\beta''}{\beta'}} \right) \left(\frac{1}{\epsilon_s k_2'} + \frac{\epsilon_{md}}{|\epsilon_m|^2 k_1'} \frac{(|k_1|^2 + |\beta|^2)}{(|k_2|^2 + |\beta|^2)} \right) \tag{3.18}$$

where V_n is the normalized effective mode volume of half of a surface plasmon wave.

In Fig. 3.5, we summarize the best attainable mode volume for a single sided surface plasmon for various indices of refraction on gold. For each index, there is a surface plasmon resonance where $\epsilon_m = -\epsilon_d$. The minimum mode volume is obtained at that wavelength.

We can also extend this analysis to understand what the constraints would be on a semiconductor gain medium to make a nanolaser that has confined a surface plasmon in this fashion. Since we know that the gain threshold needed to produce laser oscillations is governed by:

$$\Gamma \frac{c}{n_{eff}} g_{th} = \frac{1}{\tau_{ph}} = \frac{\omega_0}{Q} \tag{3.19}$$

we only need to find the confinement of electromagnetic energy inside the semiconductor, the effective index for the plasmon, and the quality factor of the resonance. In the case of a
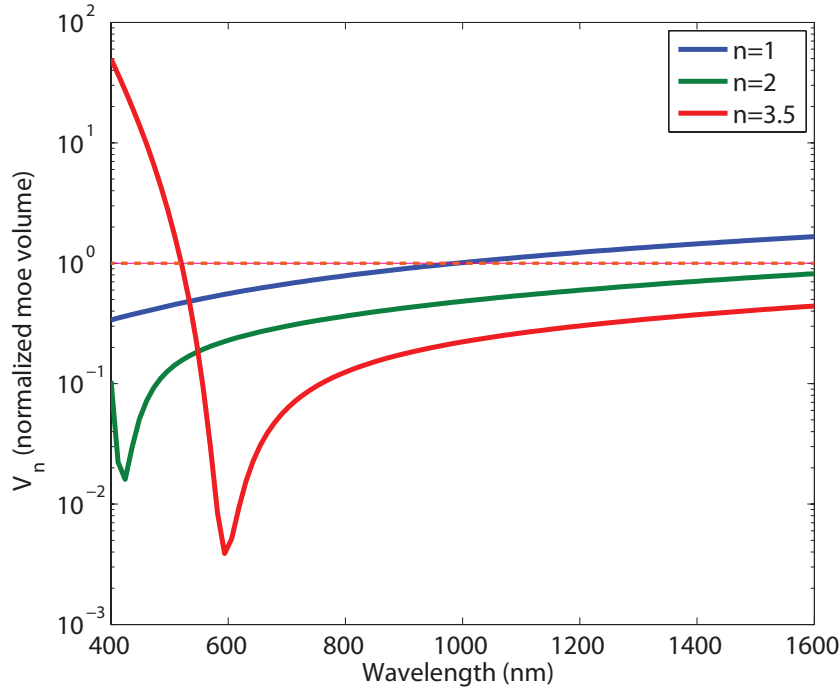
Figure 3.5. The normalized mode volume of a single-sided surface plasmon over an area of $\lambda_{sp}/2)^2$. The metal used is silver, and three different curves representing dielectric media with n=1, n=2, and n=3.5 are shown. The orange dashed line represents the diffraction limit.

surface plasmon, all three can be inferred from the original mode profile. The confinement factor Γ is:

$$\Gamma = \frac{\int_{semi} u dV}{\int_{all} u dV} = \frac{U_1}{U_1 + U_2} = \frac{1}{\left(1 + \frac{\epsilon_{md}\epsilon_s k_2'}{|\epsilon_m|^2 k_1'} \frac{(|k_1|^2 + |\beta|^2)}{(|k_2|^2 + |\beta|^2)}\right)} \tag{3.20}$$

The effective index of refraction depends on the group velocity v_g of the wave, which depends on the surface plasmon dispersion:

$$n_{eff} = \frac{c}{v_g}, \quad v_g = \left(\frac{d\beta}{d\omega}\right)^{-1}, \quad \beta(\omega) = \frac{\omega_0}{c}\sqrt{\frac{\epsilon_m \epsilon_d}{\epsilon_m + \epsilon_d}} \tag{3.21}$$

Finally, the quality factor of a surface plasmon is related to how fast the energy is lost to metal since a surface plasmon does not radiate. For a travelling wave, the plasmon will lose energy related to the imaginary component of the wavevector β'':

$$\frac{1}{\tau_{ph}} = \frac{\omega_0}{Q} = v_g \alpha = v_g 2\beta'' \quad \rightarrow \quad Q = \frac{\omega_0}{2v_g\beta''} \tag{3.22}$$

Below, in Figs. 3.6, 3.7, and 3.8, the confinement factor Γ, n_{eff}, and Q are plotted, respectively. The threshold gain Eq. (3.19) is also plotted in Fig. 3.9. The threshold gain
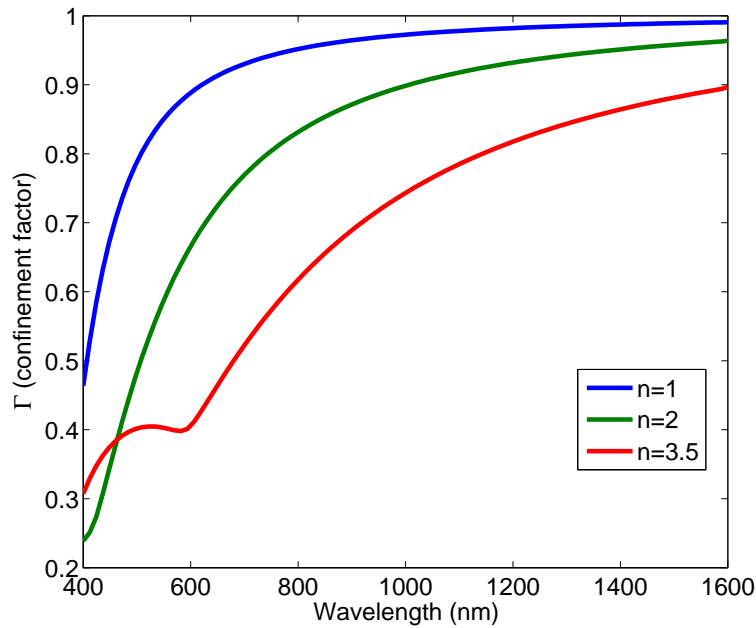
Figure 3.6. The confinement factor, or the percentage of electromagnetic energy of a surface plasmon between the interface of silver and a dielectric material, is plotted for three different indices of refraction ($n = 1$, $n = 2$, and $n = 3.5$).
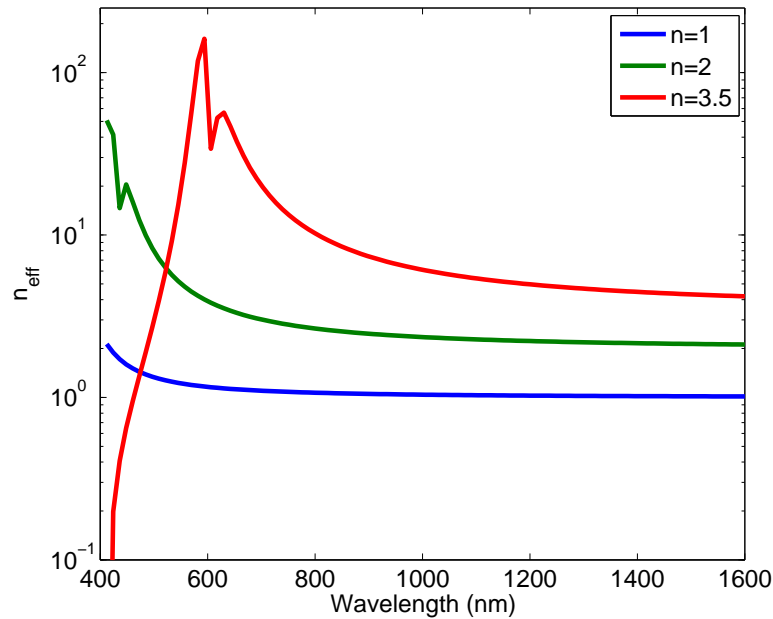
Figure 3.7. The effective index of a surface plasmon wave travelling between a silver and dielectric media with indices of refraction of $n = 1$, $n = 2$, and $n = 3.5$.
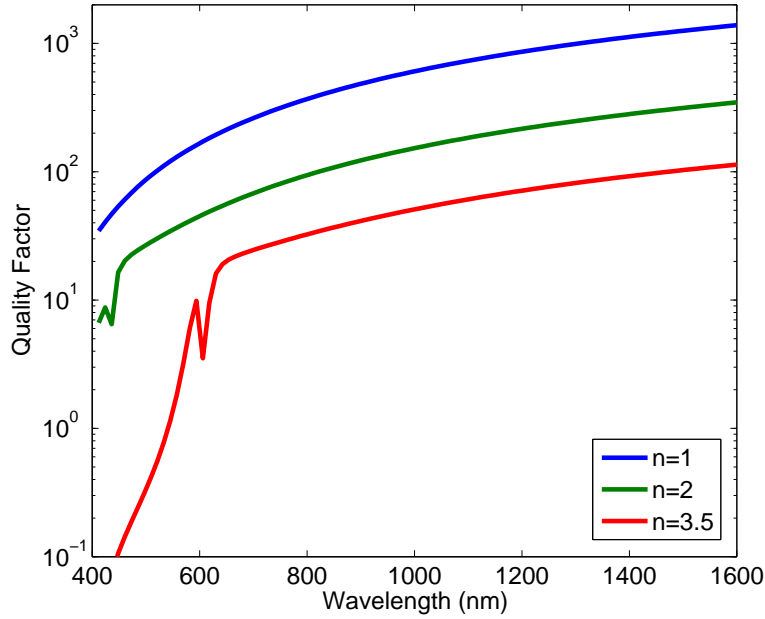
Figure 3.8. The quality factor of a surface plasmon that has been confined into a cavity between silver and a dielectric with indices of refraction of $n = 1$, $n = 2$, and $n = 3.5$
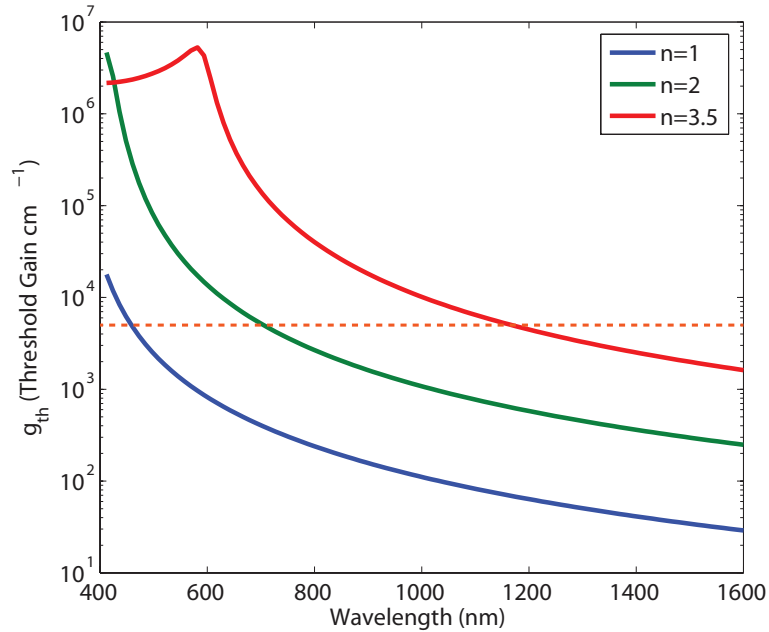
Figure 3.9. The threshold gain needed to produce laser oscillations for a single-sided surface plasmon between silver and three different indices of refraction. The orange dashed line represents the maximum gain available in III-V materials.

necessary to achieve lasing will be critical to understanding how much light can be practically confined in a surface plasmon nanocavity. From Fig. 3.9, we can see that III-V materials will only have enough gain to allow nanolaser operation at long wavelengths. In the future, low-loss metals will help to alleviate this issue.

Because MIM plasmons do not have an inherent limit on mode volume, I have skipped a full analysis what mode volumes would be attainable with MIM cavities. The problems with losses is exacerbated due to the presence of two metal films as well as the desire to strongly confine the optical mode. MIM cavities will thus be useful in the medium term only for Purcell-enhanced LEDs.

3.2   Examples of Nanocavities

As I have previously stated, when a metallic nanocavity is designed, the device will usually operate either via some sort of plasmonic effects to squeeze the light or through metal-optic effects which supress radiation by reflection. Here, I will present an example of each type of cavity, and discuss its merits for nanolaser technology. First, I will introduce a nanoarch optical resonator that has electromagnetic resonances due to confined MIM surface plasmon waves. Finally, in collaboration with Kim [69], I will introduce a waveguide couple metal-optic nanocavity that uses metal reflection to control and confine light into small volumes and also efficiently radiates into a silicon-on-insulator (SOI) optical waveguide.

3.2.1   Nanoarch Optical Resonators

The nanoarch optical resonator can be described as a MIM waveguide truncated at one end with metal and with a dielectric interface on the other end (Fig. 3.10). The physics of operation resemble that of a split-ring resonator [70], or a MIM transmission line [71]. This nano-arch resonator can be thought of as an optical RLC circuit. It possesses several advantages in maximizing capacitance and inductance in an extremely small volume (maximizing L and C is akin to minimizing the cavity size). Firstly, the capacitance of the nanocircuit can be controlled independently of the inductance be simply varying the width of the semicondcutor sandwiched between the two metal planes. The magnetic inductance of the circuit is also large since the metal forms a half-loop around the semiconductor ridge. Thus, a strong magnetic field is also present in the middle semiconductor layer as well where the energy of the inductor is stored. Finally, as the size of the device shrinks, the kinetic inductance becomes important as the magnetic inductance of the half-loop is reduced proportionally to the loop's circumference.

Another simple, yet intuitive way to understand the nanoarch resonator is as an open cylinder tube with discrete resonances (Fig. 3.11). Open cylinder tubes, used extensively in acoustics, have resonance frequencies that depend on the length of the tube, the shape, and whether it has closed or open ends. In a cylinder where both ends are open, the mode is
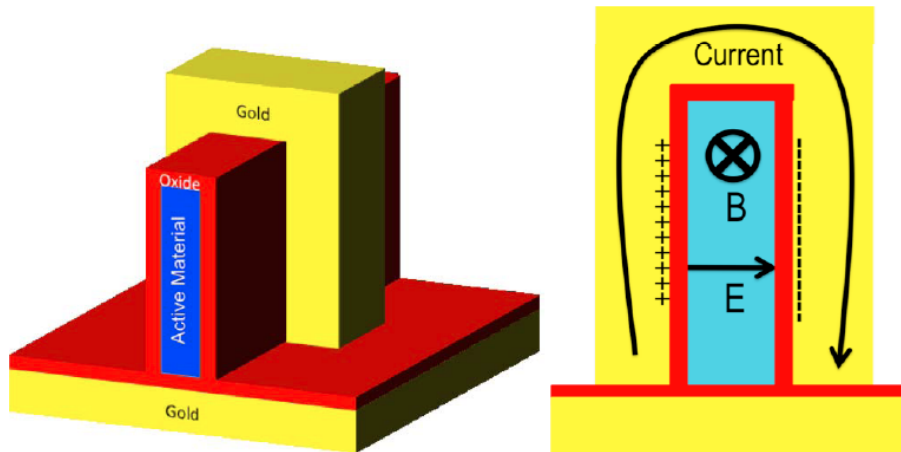
Figure 3.10. A schematic of the nano-arch circuit with an active material in the center (left). The inductance and capacitance are tuned independently to reach sub-wavelength scales. The charge and current distribution in the metal is also shown (right), where the magnetic field and electron inertia provide an inductance, and the semiconductor in the middle provides a capacitance to properly tune the circuit to the desired optical frequency. A metal ground plane is shown as a way to engineer radiation. However, the ground plane is not necessary for device operation.
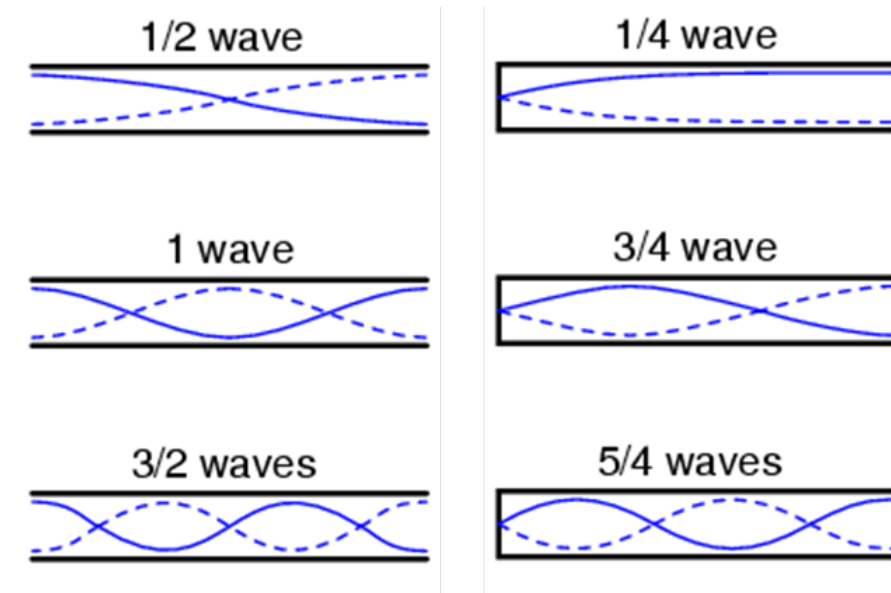
Figure 3.11. Mode resonances of an open (left) and closed (right) cylindrical cavity. The resonance frequencies of a closed cavity are half of an open cavity, making a closed cavity much more sub-wavelength than an open cylinder. [72]

extremely leaky from both sides, so that the resonance is not very strong. As the waves reflect at the open ends of the cylinder, corrections have to also be made to account for the fact that the wave is not reflected exactly at the cylinder-air boundary, but a small distance outside

of the tube. A cylinder with one side closed, on the other hand, has resonance frequencies that are half of the open cylinder cavity. This type of tube only produces odd harmonics of a fundamental frequency. The approximate equations that determine the resonance frequencies for both tubes are:

$$f_{open} = \frac{n_1 v_{sound}}{2(L + 0.8D)}$$
$$f_{closed} = \frac{n_2 v_{sound}}{4(L + 0.4D)}$$

where $n_1 = 1, 2, 3,$ and $n_2 = 1, 3, 5,$, L is the length of the tube, and D is the diameter of the tube [73].

The nano-arch cavity should have resonances that match somewhat to the simple theory described. For example, consider a cavity with a 20 nm semiconductor thickness (let the depth of metal also be 20 nm), a height of 120 nm, and a refractive index of $n = 3.5$. A closed cylindrical cavity should operate at a wavelength of $\lambda_{cav} \sim 1.8$ μm, according to the closed cylinder theory. Such a cavity is simulated to operate at a fundamental wavelength of $\lambda_{cav} \sim 1.5 - 1.8$ μm, depending on the thickness of gold around the semiconductor fin. Thus, there is qualitative agreement between the simple closed-end cylinder theory and computer simulations of the cavity design.

In COMSOL Finite Element Method (FEM) simulations, the nanoarch resonator was simulated using both 2-D and 3-D simulation modes. A monochromatic plane wave was used to excite the cavity by specifying boundary conditions. In the 2-D simulations, the magnetic field was assumed to be transverse (out of the plane of the simulation), and the E-field was polarized along the x-direction, as seen in Fig. 3.10. In this configuration, the magnetic field will drive the current to oscillate between the two prongs of the resonator. In geometries where the nano-arch structure is recessed into a substrate, quartz was used as the substrate due to its transparency near the plasma frequency of most metals.

The first two fundamental cavity modes of the nano-arch are shown in Fig. 3.12. The cavities shown are extremely subwavelength, and operate at near-IR wavelengths from 1500-1600 nm. The radiation from the cavity can be engineered by incorporating a metallic ground plane underneath the cavity and effectively cancelling out radiation into the substrate (Fig. 3.10). Thus, the surrounding metal simultaneously achieves sub-wavelength confinement, another potentially straightforward method for electrical injection, and enhanced heat dissipation. The device in the bottom panel of Fig. 3.12 has dimensions $W \times H \times L = 20 \times 40 \times 140$ nm^3 and shows a simulated cavity mode with a resonance at 1500 nm, $V_n = 0.0015$, and Q = 10. An additional design shown in the top panel of Fig. 3.12 has dimensions $W \times H \times L = 20 \times 20 \times 50$ nm^3. The cavity resonance is at 1600 nm, $V_n = 0.007$, and $Q = 11$. The calculated 3-dB bandwidths, based on the cavity volume and Q, of these two structures are 660 GHz and 160 GHz, respectively due to Purcell-enhanced spontaneous emission (Fig. 3.4). The internal quantum efficiency of the device will be high since the spontaneous emission lifetime will be enhanced greatly relative to all other non-radiative recombintation mechanisms.

FEM simulations also show that there are even higher order plasmonic resonances in the nanoarch cavity configuration, as would be expected from the simple closed-cylinder

45
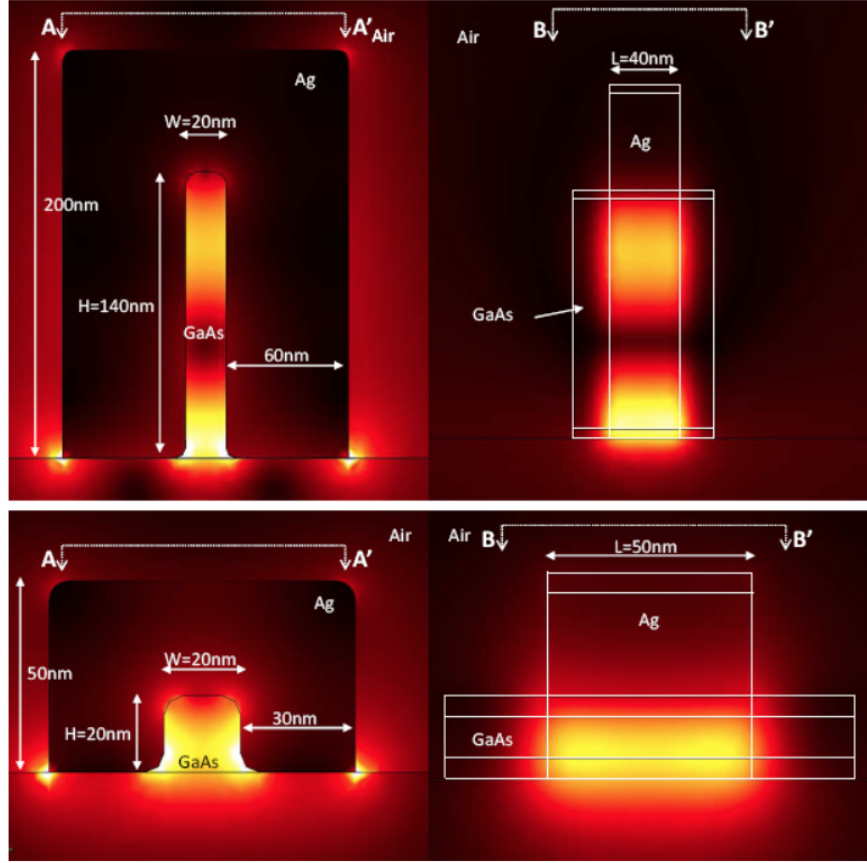
Figure 3.12. Two different nano-arch cavities are presented. The bottom panel shows a short circuit with a resonance at 1500 nm, Vn =0.0015, and Q = 10. The top panel shows a tall circuit with a resonance at 1600 nm, Vn = 0.007, and Q =11. The color represents the electric field intensity of each resonator.

theory. From Fig. 3.13, two higher order modes (3rd and 4th order) are also simulated. The third order resonance at 870nm has a quality factor of $Q_{tot} \approx 25$, a $Q_{ohmic} \approx 28$, and a $Q_{rad} \approx 270$. The confinement of the mode to the dielectric was simulated to be around 62%. The fourth order resonance at 746nm has $Q_{tot} \approx 38$, a $Q_{ohmic} \approx 39$, and a $Q_{rad} \approx 1070$. The confinement factor for this mode dropped to around 40%. From Fig. 3.13, it is apparent that higher order modes are less confined to the dielectric, and therefore the maximum field enhancement is lowered as well. This follows the fundamental relationship observed in classical metal-insulator-metal structures where higher wavevector modes require more electromagnetic field in the metal and therefore propagate for shorter distances. The resonance, however, gets sharper with increasing mode order. This occurs mainly because of the reduction in metal loss. The imaginary part of the metal's dielectric constant reaches a minimum around 670nm optical wavelength. Thus, there is less metal loss at 750nm vs. 870nm. The optical mode also radiates much less at higher optical frequencies. As the mode acquires higher wavevectors, the optical currents begin to cancel so that free-space radiation is suppressed. Thus, higher-order modes of nano-arch cavities may, with higher quality factors, may offer better designs for nanolaser design.
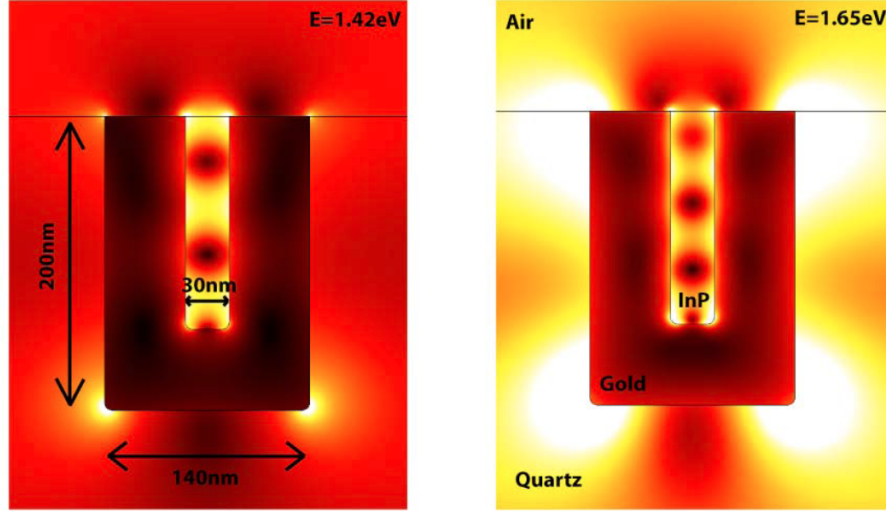
Figure 3.13. The third (left) and fourth (right) order resonances of the nano-arch device. The metal loss of the cavity becomes least lossy at energies approaching E=1.85eV, where the imaginary part of the dielectric constant of gold is minimum. The third order resonance at 870nm has a quality factor of $Q_{tot} \approx 25$, a $Q_{ohmic} \approx 28$, and a $Q_{rad} \approx 270$. The confinement of the mode to the dielectric was simulated to be around 62%. The fourth order resonance at 746nm has $Q_{tot} \approx 38$, a $Q_{ohmic} \approx 39$, and a $Q_{rad} \approx 1070$. The confinement factor for this mode dropped to around 40%.

Although the nanoarch optical resonator is an extremely small optical cavity, the coupling of the metal to the optical mode naturally reduces the cavity-Q in the form of metal resistance, making fundamental mode laser operation impossible with III-V materials ($Q_{min} \approx 30$), and difficult with II-VI materials ($Q_{min} \approx 5$). At room temperature, where non-radiative recombination and thermalization prevents full inversion of carriers, the task becomes even harder. In the future, this cavity may prove to be an extremely valuable nanolaser, but with current metallic materials, the device serves better as a Purcell-enhanced nanoLED [29]. Without the burden of achieving laser threshold conditions, a nanocavity with a normalized electromagnetic mode volume $V_n = 0.01$ only needs $Q > 10$ in order to achieve bandwidths above 100 GHz (Fig. 3.4). Thus, to obtain a coherent light source, we turn to more conventional metal-optic nanocavity designs.

3.2.2 Waveguide-coupled Metal-optic Nanocavities

Metal-optic nanolasers do not rely on surface plasmons to confine light into small volumes. Instead, the metal acts as a reflector. It is well known that as a purely dielectric cavity is shrunk and approaches the diffraction limit, large amounts of energy escape the high-index semiconductor as radiation. In Fig. 3.14, as a metal shield is wrapped more and more tightly around a semiconductor resonator, the large amount of radiation is basically eliminated. It is important to stress that the nature of the light-metal interaction is distinctly different

47

than a purely plasmonic interaction. In a surface plasmon, electric field lines are terminated on the metal surface where charge accumulates. In the case of this metal reflector, electric field lines are parallel to the metal surface and are thus repelled from the metal itself. This "repulsion" reduces the amount of electromagnetic energy in the conductor and helps to increase the optical quality factor of the nanocavity. Of course, without the incredibly large wavevectors available to surface plasmons, metal-optic cavities will necessarily be larger than plasmonic nanocavities.
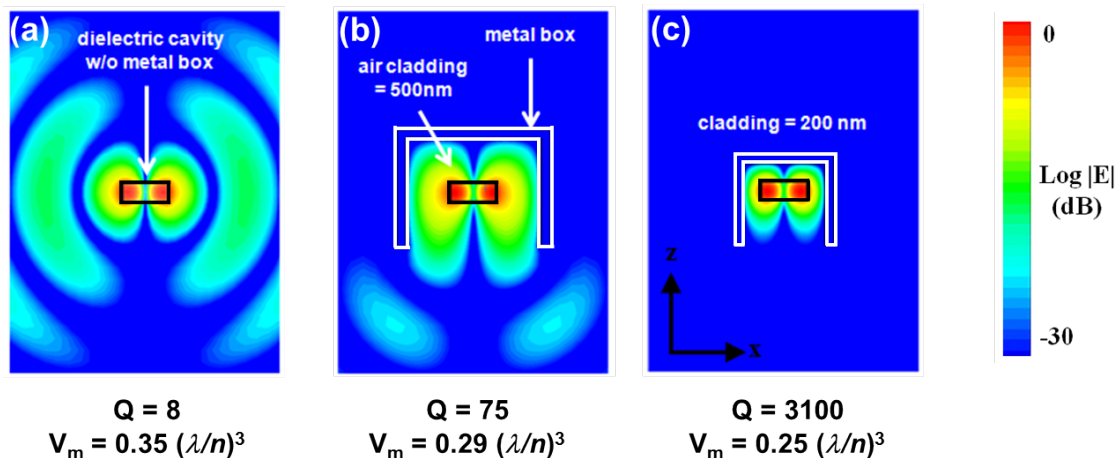
Figure 3.14. In (a), (b), and (c) we show the successive reduction in radiation for a 500nm x 400nm x 200 nm semiconductor block by introducing a reflective metallic box around it. Using metal, we can acheive quality factors as high as $Q = 3100$.

Up to this point, we have not focused on methods that will couple laser radiation for useful purposes (i.e. on-chip optical communication). Coupling this laser radiation efficiently to a waveguide will be critical to integrate the devices into a coherent optical communication system. In Fig. 3.15a, a metal-optic nanocavity is integrated with a silicon-on-insulator waveguide [51]. The electromagnetic energy of the laser is confined (mostly by dielectric confinement) into an amplifying semiconductor region. The oxide coating and metal enclosure furthers serves as a method to eliminate excessive radiation into undesirable modes. Using metal purely as a radiation engineering tool, the device is able to achieve quality factors higher than $Q > 600$.

The actual electromagnetic nanocavity consists of an InGaAsP bulk semiconductor cuboid with a height (h) of 350 nm, a width (w) of 350 nm, and a variable length (l). The device is also configured for electrical carrier injection by introducing doped InP posts on the top and bottom of the cavity. To reduce the resistivity of the laser diode, 50 nm thin doped InGaAsP pads are used as the ohmic contacts to the n- and p-metal layers. The n-InGaAsP electrode has the same length and width as the InGaAsP nanocavity (l by 350 nm). For the cubic cavity structure with $l = 350$ nm, the cavity operates in the fundamental transverse electric (TE) mode that resembles a donut at a frequency of 204.8 THz (1.46 μm). The second mode is spectrally separated from the first mode by 44 THz (258 nm). An SiO$_2$ cladding also envelops the device with a certain thickness that can be engineered

to control the quality factor (Q) of the cavity and achieve the highest coupling rate into the Si-waveguide. Finally, to suppress unwanted radiation, we coat the entire cavity with 100 nm of silver (except on the bottom). The width of the Si-waveguide is designed to be the same as the cavity in order to simplify the fabrication process so that the nanolaser and waveguide are self-aligned, as shown in Fig. 3.15c. We also fix the thickness of the waveguide to 120 nm to guarantee that it operates in the single-mode regime. Finally, we use a 50 nm interfacial SiO_2 layer between the p-InGaAsP and Si-waveguide in a molecular wafer bonding process [74], as shown in Fig. 3.15b.
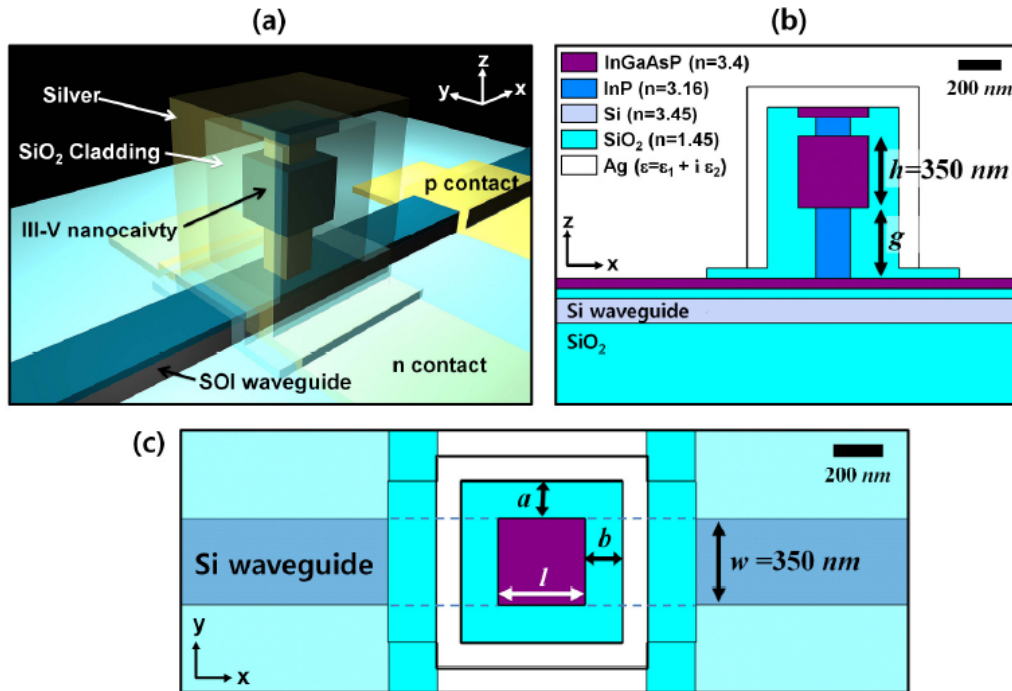
Figure 3.15. Perspective (a) and cross-sectional (b, c) schematic views of a Si-waveguide coupled metal-clad nanolaser cavity. Here, the nanolaser cavity is designed as a cuboid structure with a height (h) of 350 nm, a width (w) of 350 nm, and a variable length (l).

Initially, we focus on optimizing the nanolaser without the Si-waveguide. The first parameter we engineer is the thickness of the SiO_2 cladding by simulating the cavity structures using finite-difference time-domain (FDTD) simulations. To study the effects of the cladding, we first place the nanolaser cavity on a pure silicon substrate instead of a Si-waveguide (Fig. 3.16a) to avoid any second-order effects that may result due to variations in coupling efficiency as a function of cladding thickness. We also keep the cladding thickness the same in both x- and y-directions ($a = b$, where a and b are defined in Fig. 3.15c) to preserve the symmetry of the cavity mode. The heights of top and bottom InP posts are initially fixed at 100 nm and 600 nm, respectively, and we find that the InP posts must be undercut by at least 90 nm to maintain a high quality factor nanocavity. Here, the cavity length (l) is fixed at 350 nm. In Fig. 3.16b, we can see that the Q-factor of the device depends sensitively on the SiO_2 thickness. If the SiO_2 is 150 nm thick, we are able to achieve a maximum Q-factor
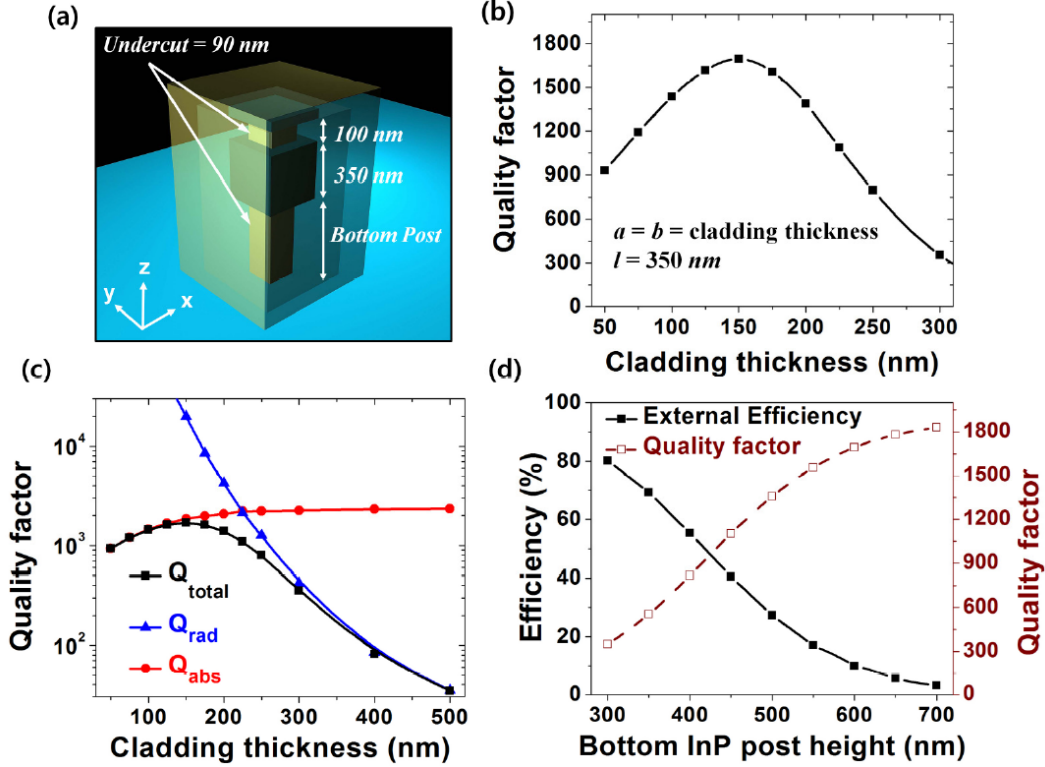
Figure 3.16. (a) Schematic of a metal-clad nanocavity on a semiconductor substrate. (b) Quality factor as a function of the cladding size ($a = b$). (c) Total Q-factor, radiation Q-factor, and absorption Q-factor as a function of cladding size. (d) External efficiency and quality factor of the cavity as a function of bottom InP post height between the nanocavity and the substrate.

of 1700. This optimal cladding thickness suggests that there is a trade-off between metal and radiation loss. If we decompose the total cavity quality factor into radiation (Q_{rad}) and the absorption (Q_{abs}) with the relation of $Q_{total}^{-1} = Q_{rad}^{-1} + Q_{abs}^{-1}$ (Fig. 3.16c), we find that for cladding thicknesses larger than 225 nm, radiation is the dominant loss mechanism in the cavity. Such large amounts of radiation are the result of the low effective refractive index of the fundamental mode resulting in weak vertical confinement. To investigate the effect of cladding size on radiation, we transform the spatial modes of two cavities with cladding thicknesses of 300 nm and 150 nm, respectively seen in Figs. 3.17a and 3.17b, into the Fourier domain to see the in-plane wavevector distribution ($k_{\parallel}$) of the cavity modes (Figs. 3.17e and 3.17f). Here, the k-components inside the white dotted line of n=1.5 represent the vertical radiation components of the mode into the SiO$_2$ cladding since they fail to satisfy the condition of total-internal-reflection (TIR) along the vertical direction. In comparing the two different cavities, we see that the device with a cladding of 300 nm has much more energy that fails to satisfy TIR compared to the more thinly clad device. From the effective index viewpoint, the device with 300 nm cladding has an effective index of $n = 1.63$ while the cavity with 150 nm of SiO$_2$ has an effective index of $n = 2.0$. Thus, we see that although thicker claddings result in less metal loss, the effective index of the mode decreases, resulting

in large amounts of radiation. Specifically, a cladding of 300 nm around the nanocavity results in a radiation to total loss ratio of 84%. We can achieve a radiation to total loss ratio of 50% when the cladding is 225 nm thick. Although we can achieve high suppression of radiation by reducing the cladding thickness, the absorption loss from the metal reflector starts to become significant. As a result, the maximum total quality factor is the result of the trade-off between these two loss channels, as shown in Fig. 3.16c.
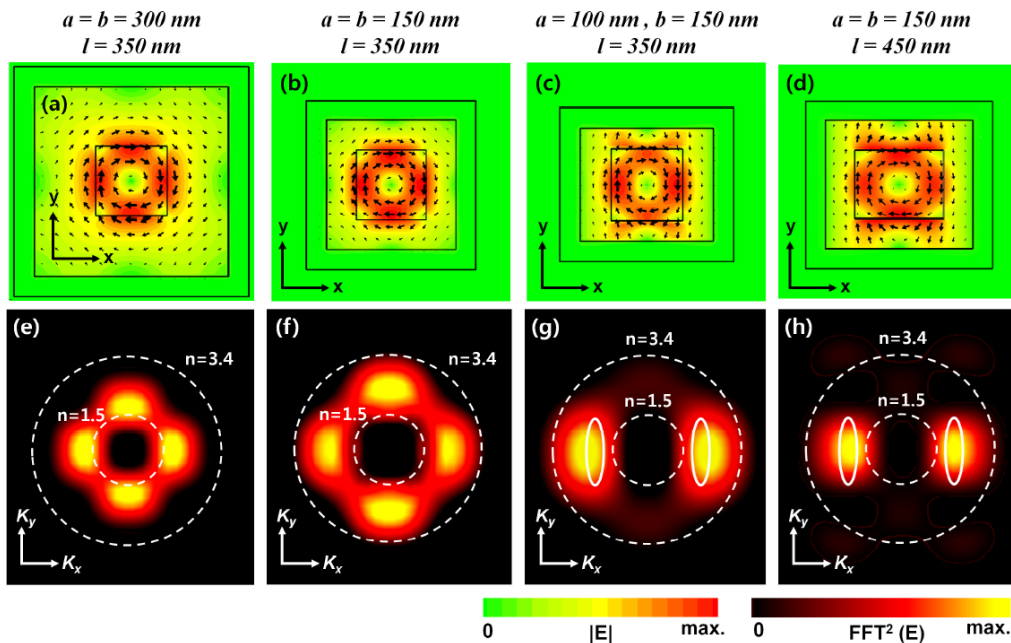
Figure 3.17. Electric field intensity profile (vector plot overlaid) and the Fourier transform of the electric field profile for (a, e) $a = b = 300$ nm and $l = 350$ nm, (b, f) $a = b = 150$ nm and $l = 350$ nm (c, g) $a = 100$ nm, $b = 150$ nm and $l = 350$ nm, and (d, h) $a = b = 150$ nm and $l = 450$ nm, respectively. Here, a, b and l are defined in Fig. 3.15c. The closed solid lines in (g) and (h) enclose the wavevectors that couple to the Si-waveguide.

After optimizing the SiO$_2$ cladding to obtain a quality factor > 1700, the bottom InP post height (g) can also be engineered to create high total external efficiency (defined to be the ratio of total radiated power and total lost power, including metal loss). In Fig. 3.16d, we show the dependence of the cavity quality factor as well as the external efficiency of the cavity as a function of bottom InP post height. As we reduce the post height, the radiation rate increases due to strong coupling of the cavity mode with the continuum modes of the high-index substrate. Thus, the external efficiency can be engineered from 10% to 55% by reducing the bottom post height from 600 nm to 400 nm although total Q-factor is reduced from 1700 to 810.

After optimizing the cavity design to have a high quality factor and a high external efficiency, we focus our attention to efficiently coupling the device to a conventional waveguide. Thus, we aim to maximize the efficiency of coupling of laser radiation into the Si-waveguide ($\gamma_{coupling}/\gamma_{rad}$). Here, $\gamma_{coupling}$ and γ_{rad} represent the cavity-to-waveguide coupling rate and

the total cavity radiation rate, respectively, as seen in Fig. 3.18a. The emission pattern of the nanocavity is naturally divergent due its small size, making it difficult to couple the output light efficiently into a waveguide. Among various coupling approaches, coupling light to a single mode SOI waveguide is particularly interesting because it provides a means to integrate laser sources for silicon photonics technology. Using wafer bonding techniques, the metal-clad nanocavity can be integrated onto a Si-waveguide [75–77]. The light from the nanocavity will then couple to the waveguide via weak evanescent coupling from the bottom of the nanocavity. For example, a nanocavity with a cladding thickness and bottom post height (g) of 150 nm ($a = b = 150$ nm) and 600 nm, respectively, has a 22% coupling efficiency to the Si-waveguide. To further couple light into the waveguide, we modify the field distribution of the cavity mode to break the symmetry of the cavity mode and make it preferentially radiate in the x-direction into the waveguide. There are two main ways to break the symmetry of the nanocavity: we can introduce asymmetry in the cladding thickness in the x- and y-directions around a cubic cavity, as shown in Fig. 3.17c, or we can modify the cubic InGaAsP gain region to make it rectangular, as shown in Fig. 3.17d. Both cases are investigated.

In Fig. 3.17c, we show the electric-field distribution of a device with asymmetric cladding thicknesses along the x- and y-direction with $a = 100$ nm and $b = 150$ nm. As we might expect, the symmetry of the field-profile is reduced and the electric field vectors point predominantly along the y-direction (when $a < b$). Accordingly, the in-plane k-components in the Fourier domain are highly concentrated on the k_x axis, as shown in Fig. 3.17g. Thus, by making the cladding asymmetric, we can independently engineer the amount of metallic reflection on the cavity mode along the x- and y-direction.

Similarly, we can modify the InGaAsP cavity to make it rectangular while keeping the cladding thickness the same. In this case, the electric field vectors again point predominantly along the y-direction when $l > 350$ nm, as shown in Fig. 3.17d. Accordingly, the in-plane k-components in the Fourier domain are highly concentrated on the k_x axis as well, as shown in Fig. 3.17h. The closed solid white lines in Figs. 3.17h and f enclose the approximate wavevectors that couple to the Si-waveguide. Since the in-plane wavevectors of the cavity and the waveguide modes are largely overlapped, we verify the high coupling rate from the nanocavity to the waveguide.

In Fig. 3.18, we summarize the influence of various design parameters on the coupling efficiency, energy confinement factor, cavity quality factor, and laser threshold gain. In Fig. 3.18b, we show how the coupling efficiency and energy confinement factor (in the III-V active region) change as a function of the y-cladding thickness (a) for a fixed x-cladding thickness (b), cavity length (l), and bottom post height (g) of 150 nm, 350 nm, and 600 nm, respectively. As we reduce a to less than 60 nm, the coupling efficiency to the Si-waveguide dramatically increases to over 75% although the confinement and quality factors are degraded as more field leaks out into the cladding and metal as a is reduced. Figure 3.18c shows the quality factor and threshold material gain coefficient for lasing as a function of a. Thus, if a is designed to be 60 nm, then the coupling efficiency is 76%, the threshold gain is 100 cm^{-1}, and the cavity quality factor is ~ 1000.

If we make the InGaAsP cavity rectangular (we vary l), then there is a potential advantage
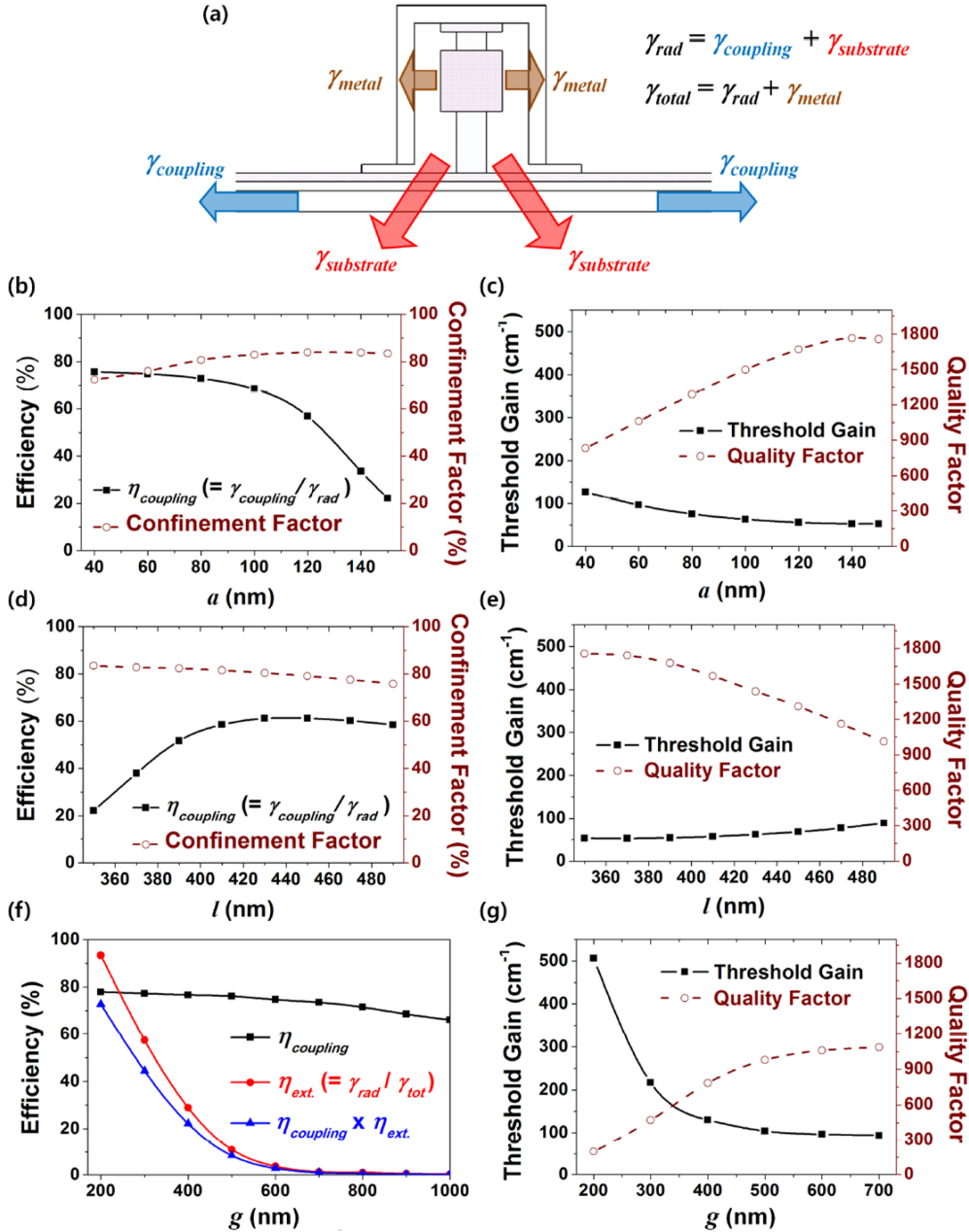
Figure 3.18. (a) Illustration showing the various energy loss paths from the cavity including metal and radiation losses. (b, c, d, e) Coupling efficiency ($\gamma_{coupling}/\gamma_{rad}$) to Si-waveguide, energy confinement factor into active region, threshold material gain coefficient for lasing, and cavity quality factor as a function of a and l, respectively, with $b = 150\ nm$ and $g = 600\ nm$. (f, g) Coupling efficiency, total external efficiency, total energy efficiency to Si-waveguide, threshold material gain coefficient for lasing, and quality factor as a function of g for the optimal structure with $a = 60\ nm$, $b = 150\ nm$ and $l = 350\ nm$.

in fabrication, since the oxide can be kept uniformly thick around the device. A rectangular cavity can also be self-aligned, making fabrication easier. Thus, if $a = b = 150\ nm$, and
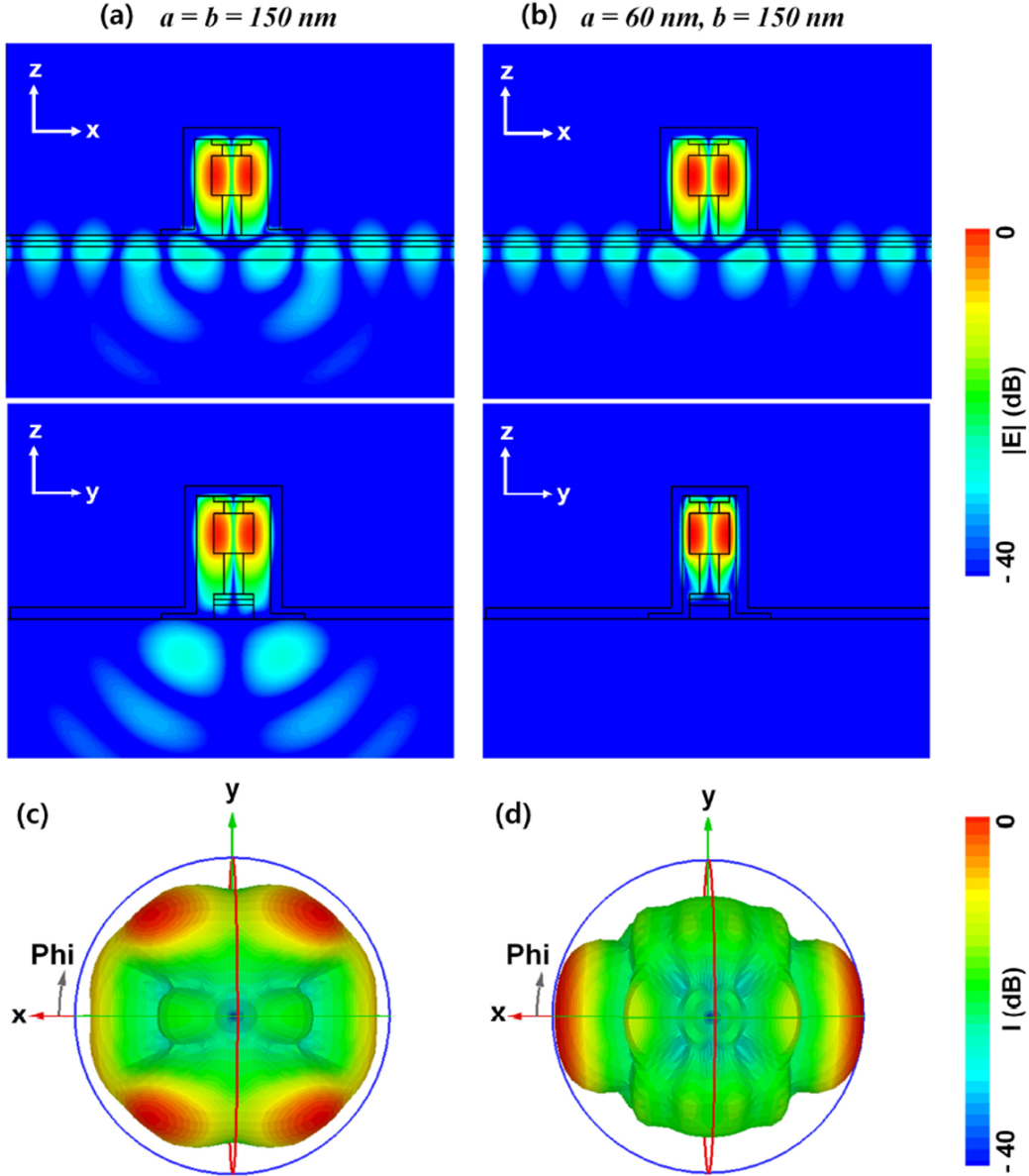
Figure 3.19. Cross-sectional side views of —E— in logarithm scale with 40 dB range in the x-z and y-z planes for a of (a) 150 nm and (b) 60 nm, respectively, where b and g are fixed at 150 nm and 350 nm, respectively. Far-field radiation patterns to the substrate direction for a of (c) 150 nm and (d) 60 nm, respectively.

the bottom InP post height (g) is kept at 600 nm, then a maximum coupling efficiency of 61% is achieved when $l = 430$ nm (Fig. 3.18d). The confinement factor remains high at 79%, and the quality factor and threshold gain are 1440 and 62 cm^{-1}, respectively (Fig. 3.18e). Thus, we obtain a smaller coupling efficiency for a cavity where we engineer l versus a. We attribute the smaller coupling efficiency to the fact that a 150 nm cladding thickness generates a lot of radiation into the substrate regardless of the shape of the nanocavity. Thus, there seems to be a tradeoff between coupling efficiency and ease of fabrication.

So far, even though we have optimized the coupling efficiency ($\gamma_{coupling}/\gamma_{rad}$) of the nanocavity to the waveguide using two different methods, the total external efficiency ($\gamma_{rad}/\gamma_{total}$) of the device remains low around 4% due to high metal loss. Here, γ_{total} represents the total energy decay rate in the cavity due to both metal and radiation loss, as shown in Fig. 3.18a. As before, however, we can engineer the external efficiency of our device by changing the height of the bottom InP post (g), as shown in Fig. 3.18f. Here, we use asymmetric cladding to optimize our coupling efficiency by setting a, b, and l to 60 nm, 150 nm and 350 nm, respectively. Interestingly, the coupling efficiency remains almost constant around 75% even if we change g from 200-700 nm. Thus, we can independently engineer coupling and total external efficiencies by tuning cladding asymmetry and bottom InP post height, respectively. However, the total quality factor is decreased as g is reduced since we increase our total radiation rate, as shown in Fig. 3.18g. Accordingly, the threshold III-V material gain for lasing is also increased.

After fully and systematically optimizing our nanolaser, we find that the device operates most efficiency when g and a are 350 nm and 60 nm, respectively, in a cubic cavity ($l = 350$ nm). These dimensions result in high external efficiency and high Q-factor cavities. At these conditions, the coupling efficiency, the total external efficiency, the Q-factor, and the threshold material gain coefficient for lasing are calculated to be 78%, 43%, 630 and 153 cm^1, respectively. In Figs. 3.19a and b, we show the electric-field amplitudes in the same logarithm scale with 40 dB range for $a = 60$ nm, $b = 150$ nm, and $g = 350$ nm. These plots illustrate how much more efficiently the nanocavity functions when the y-cladding thickness is 60 nm versus 150 nm. The far-field radiation patterns to the substrate direction of these two cases, as seen in Figs. 3.19c and d, more clearly demonstrate how much the radiation is enhanced to the waveguide direction by the asymmetric claddings.
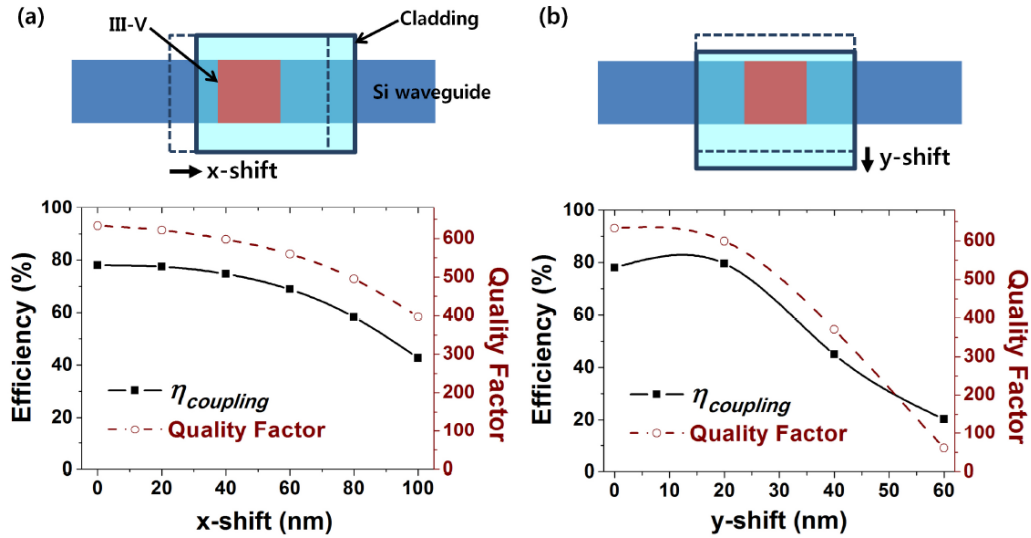
Figure 3.20. Coupling efficiency and quality factor for nanocavities with misaligned cladding positions along the (a) x- and (b) y-direction.

Finally, we have also explored the sensitivity of our design to various alignment errors

that might occur in fabrication. In Fig. 3.20, we explore how the coupling efficiency and quality factor change when the SiO$_2$ cladding is misaligned to the InGaAsP nanocavity in both x- and y-directions. Here, the parameters a, b, l and g are fixed at the optimized values of 60 nm, 150 nm, 350 nm and 350 nm, respectively. Since the field is stronger in this cavity mode in the y-direction due to thin 60 nm cladding, the coupling efficiency and quality factor are highly sensitive to misalignment in this direction, as shown in Fig. 3.20b. When the x- and y-shifts are larger than 90 nm and 37 nm, the coupling efficiency and Q-factor are degraded to less than 50% and 450, respectively.

Chapter 4

Plasmonic Crystal Defect Nanolasers

Up to now, I have discussed various aspects of nanolaser design, and have shown some theoretical nanolaser designs utilizing plasmonics and metal-optics. In this chapter and Chapter 5, I will present experimental demonstrations of two nanolaser designs. These devices utilize very different methods of confining light, but the goal is the same: to create useful nanolasers for integrated photonics applications.

Surface plasmons have a unique ability to manipulate light below the diffraction limit. Nanolasers based on surface plasmons are even more interesting, since they represent coherent light sources that will enable myriad applications in nanophotonic circuits [78]. Yet, in order to truly create nanophotonic (or plasmonic) circuits, new advances must take place that allow the integration of various active and passive circuit elements. Innovation at the device level simply will not suffice for useful applications. System-level integration will be a key driver in ushering in a new era of nanophotonic circuitry.

In photonic circuits, such system-level integration is achieved by carefully engineering discrete components to "work" together with minimal perturbation to the individual devices. For example, an older-generation photonic integration circuit (PIC) from Infinera currently has an array of lasers, modulators, and waveguides designed for high-throughput for long-haul optical communication [13]. Yet, each component was engineered individually, and each device has its own power, material, and fabrication requirements to operate efficiently.

A more elegant solution would involve the creation of a "photonic substrate" where all components could be built at the same time with the same materials [79]. Newer generation PIC's from companies such as Infinera and Luxtera have began using common semiconductor platforms (e.g. InP and silicon) to make photodetectors, modulators, and waveguides in a single fabrication process. Such system level integration will certainly reduce costs and improve photonic performance.

Much like transistors, however, photonic circuits will have incentives to miniaturize to accomodate more functionality and reduce power consumption. At the wavelength scale,

controlling light will become tricky. Yet, photonic crystals may provide an easy to use "nanophotonic substrate" where lasers, waveguides, modulators, etc. could be implemented with minimal footprint and power consumption. Since their discovery in 1987 [80], photonic crystals have made enormous progress in the implementation of entire photonic circuits [34–37]. Yet, electrical injection of carriers has been an elusive goal until recently due to various technological challenges present with introduction resistive metal so close to photonic devices [37].

Recently, Kim et al have theorized that combining concepts from photonic crystal structures with plasmonics to create sub-diffraction-limited nanolasers [69]. In this regime, where metal is a necessary part of the design of plasmonic devices, the major challenge of reliably electrically driving the active components of photonic crystals can be overcome. Furthermore, surface plasmons will allow nanolasers to attain electromagnetic mode volumes that are much smaller than possible with purely photonic devices. In this thesis, I demonstrate a nanolaser based on a defect inside a surface plasmon polariton crystal (SPPC or plasmonic crystal). A SPPC is simply a periodic structure on a metal film capable of manipulating surface plasmons at the metal/dielectric interface. It is engineered to have stopbands that inhibit travelling surface plasmons of certain frequencies. Recent attempts at creating such devices have not been able to overcome resistive losses to create active laser devices [81].

I was able to experimentally localize plasmon oscillations using a defect in this periodic structure and achieve lasing in mode volumes of $V_{eff} = 0.3(\lambda/n)^3$ at $\lambda_0 = 1342\ nm$ for the first time. We envision that plasmonic crystals will be useful for not only nanolasers, but also Purcell-enhanced light-emitting diodes capable of modulation speeds >100 GHz due to the exquisite controllability of electromagnetic mode volumes [29]. With this nanolaser demonstration, plasmonic crystals are strongly placed to become a new paradigm for the development of robust and engineered active nanophotonic circuits capable of incorporating deep-subwavelength light emitters.

4.1 Analytical Modelling and Simulation

In Fig. 4.1a, we show the geometry of the plasmonic crystal defect nanolaser. A periodically patterned nanobeam of InGaAsP/InP is placed on a 100 nm thick gold film with a 3 nm Ti adhesion layer and a 5 nm TiO$_2$ spacer layer. The device has three air holes missing in the center and has a width w, lattice constant a, and hole diameter d. The nanobeam consists of a 200 nm InGaAsP ($E_g = 0.8\ eV$) layer sandwiched by 10 nm of InP barrier material.
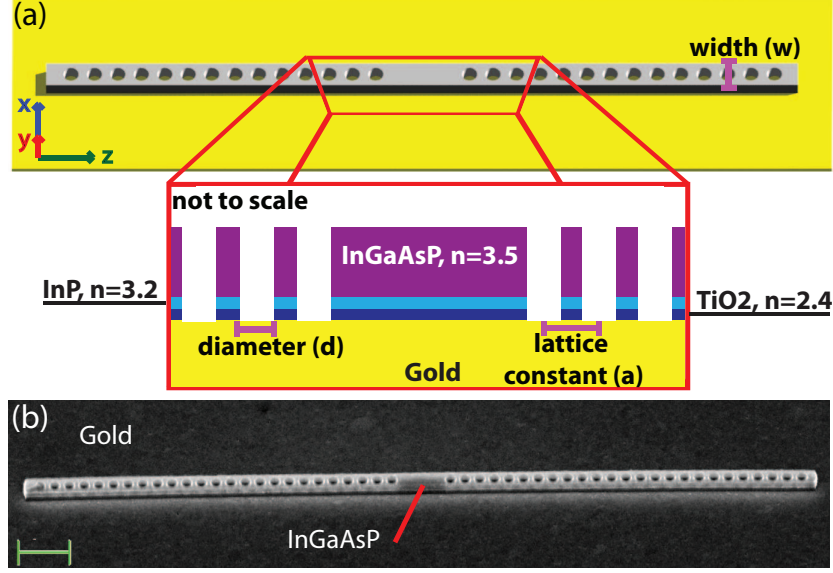
Figure 4.1. (a) A schematic of a one-dimensional plasmonic crystal. The nanobeam consists of InGaAsP with a 5 nm TiO$_2$ dielectric barrier and a 10 nm InP barrier between it and the metal. The 3 nm Ti adhesion layer is left off for simplicity. The device has three-air-hole defect in the middle of the device The beam is 225 nm thick and w wide with air holes of diameter d spaced apart by lattice constant a. (b) A scanning electron micrograph of a fabricated device. The scale bar represents 1 μm.

Analytically, it is very difficult to find a quantitative understanding of both photonic and plasmonic crystals. Yet, the periodic nature of the photonic and plasmonic crystal is analogous to a semiconductor crystal for electrons. In a periodic system with a Brillouin zone and wavevectors $\vec{k} = k_1\vec{b_1} + k_2\vec{b_2} + k_3\vec{b_3}$, each propagating photon will have a energy dispersion $E(\vec{k})$ and a mode profile determined by Bloch waves:

$$\vec{H}_{\vec{k}}(\vec{r}) = e^{i\vec{k}\cdot\vec{r}}\vec{u}_{\vec{k}}(\vec{r})$$

where $\vec{u}_{\vec{k}}(\vec{r})$ is a periodic function of the photonic crystal lattice so that $\vec{u}_{\vec{k}}(\vec{r}) = \vec{u}_{\vec{k}}(\vec{r} + \vec{R})$. Furthermore, the energy dispersion $E(\vec{k})$ will follow the same band structure as electrons in a semiconductor crystal as well. If designed properly, there will be certain bandgaps where photons of certain energies will not be allowed to exist in the crystal.

I simulated the band structure for the one-dimensional plasmonic crystal with finite difference time domain (FDTD) numerical techniques. A unit cell (no defects) with the layer structure shown in Fig. 4.2 was enclosed by a perfectly matched layer (PML) to absorb radiation on all non-repeating boundaries. On the repeating boundaries, we used Bloch boundary conditions to obtain the dispersion of various bands of the periodic structure. To match simulation with experimentally observed data, I used the dimensions (beam width, lattice constant, and hole diameter) of the devices obtained by scanning electron microscope (SEM).

The one-dimensional plasmonic crystal is distinctly different from a photonic crystal due to the metal film. We show the travelling wave resonances of a plasmonic crys-

Figure 4.2. The layer structure that was simulated is shown above. The figure is not drawn to scale and does not represent the true dimensions of the device. The thickness of the TiO_2 layer is 5 nm, the thickness of the InP barrier layer is 10 nm, and the InGaAsP semiconductor (with bandgap $E_g = 0.8\ eV$) is 200 nm thick. The 3 nm Ti adhesion layer between the gold and TiO_2 is not shown. The gold dispersion was obtained using values from [52].

tal and photonic crystal with the same dimensions at the band-edge ($k = \pi/a$, where a is the lattice constant) in Fig. 4.4a. We can quantify how plasmonic or photonic a particular travelling wave is by comparing the amount of energy present in the parallel and perpendicular components of the electric field near the metal/semiconductor interface: $\kappa = \int \epsilon(\vec{r})|\vec{E}_{para}(\vec{r})|^2 da / \int \epsilon(\vec{r})|\vec{E}_{perp}(\vec{r})|^2 da$. Also, we can measure the fraction of electromagnetic energy in the metal for any given travelling wave. If the metal is acting as a reflector, most of the field will be parallel to the interface, and κ will be large (the energy in the metal will be small). If most of the field is perpendicular to the interface, then the metal is supporting a plasmon, and κ will be small. In Fig. 4.4c, the κ parameter is plotted for the first 13 bands of the plasmonic crystal. In the SPPC, the first four modes have dominant plasmonic characteristics. The fifth mode (E) is the first mode to have significant reflection from the metal, and is therefore considered the first TE mode. Similarly, the percentage of energy of the various travelling eigenmodes in the metal is shown in Fig. 4.4b.

Thus, the plasmonic crystal is heavily influenced by the presence of the metal film compared to a photonic crystal structure surrounded completely by air of the same size. To gain more intuition about the mechanisms of the metal's influence, we contrast various aspects of plasmonic and photonic crystals in Fig. 4.3. Both photonic and plasmonic crystals have transverse magnetic (TM) and transverse electric (TE) modes present. For example, band A (TM) and band E (TE) profiles for an SPPC are shown in Figs. 4.3e-f while the same modes in a photonic crystal are shown Figs. 4.3g-h without the metal film. In general, the metal film interacts predominantly with TM waves, and only perturbs TE waves slightly. In a photonic crystal, the TM modes operate at much higher frequency relative to the SPPC and do not form a bandgap (e.g. A' and B' are nearly degenerate at the Brillouin zone edge). The dielectric structure does, however, have a bandgap for TE travelling waves. In contrast, in a plasmonic crystal, the TM travelling waves present in the photonic crystal interact heavily with the metal film and become surface plasmons, which are also TM. Furthermore, their operating frequencies drop (e.g. band A' is at 280 THz while band A is at 190 THz at the band-edge). Finally, and perhaps most importantly, the metal film interaction separates the photonic TM modes at the crystal band-edge and allows for the creation of defects that can

(a) Plasmonic crystal

Frequency (THz) — 160, 180, 200, 220, 240, 260, 280, 300

Wavevector (2π/a) — 0.35, 0.4, 0.45, 0.5

Δ_2, Δ_1, δ, γ, β, α

F, E, D, C, B, A

(b) Photonic crystal

Frequency (THz) — 160, 180, 200, 220, 240, 260, 280, 300

Wavevector (2π/a) — 0.35, 0.4, 0.45, 0.5

TE Photonic Bandgap

α'

D', C', A', B', E'

(e) Plasmonic crystal

A

(f)

E

(g) Photonic crystal

A'

(h)

E'

(c) $\varepsilon|E|^2$ — plasmonic α defect mode

(d) $\varepsilon|E|^2$ — photonic α' defect mode
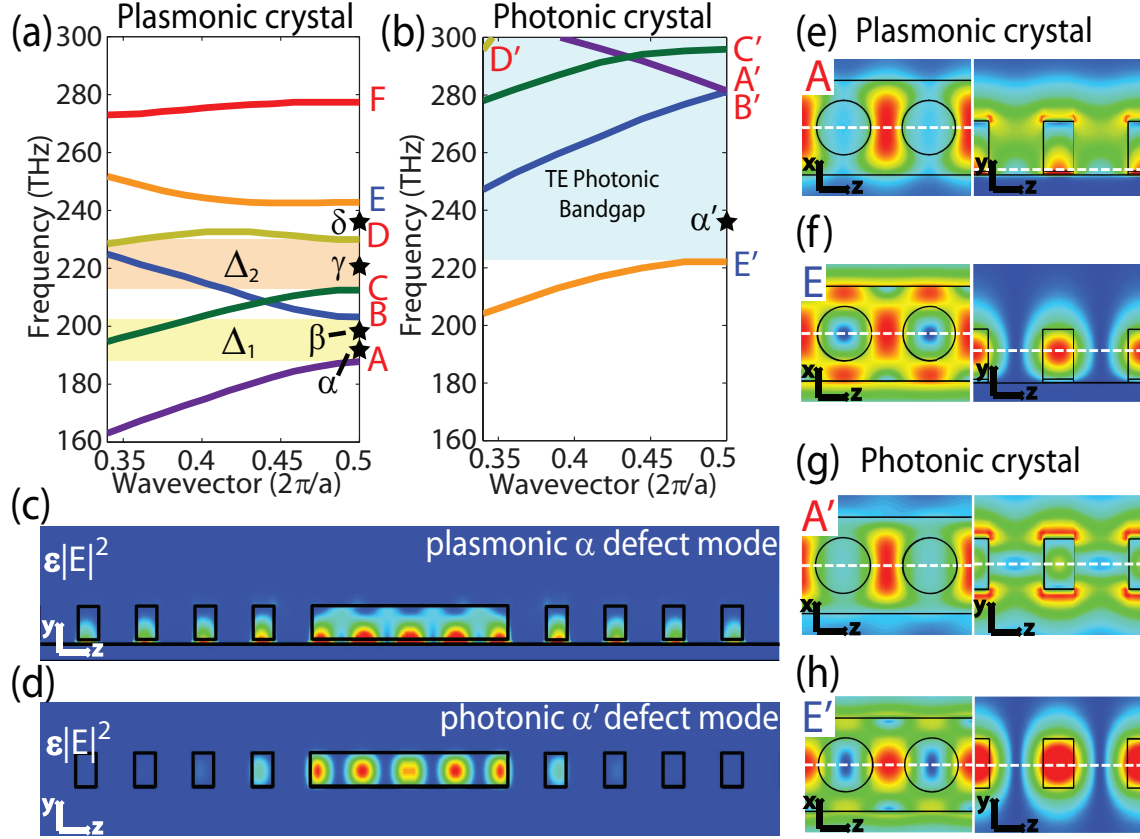
Figure 4.3. A contrast of aplasmonic crystal and photonic crystal of the same dimensions. (a) The simulated band structure for the plasmonic crystal device seen in Fig. 4.8a with first six bands of the device (A-F). The plasmonic/TV bands are red and photonic/TE bands are blue). Two novel plasmonic bandgaps (Δ_1 and $Delta_2$) appear in (a). A 3-hole defect in the device creates defect eigenmodes shown as black stars at the Broullion zone edge. (b) The simulated band structure for a photonic crystal with exact dimensions in Fig. 4.8a but without the metal substrate. The primed bands (e.g. A') correspond to the same waves in the plasmonic crystal geometry (e.g. A). The photonic crystal has a defect mode, α', within a TE bandgap that extends from 222 THz to beyond 300 THz. (c) A profile in the y-z plane of the electric energy density of the α defect mode in a plasmonic crystal. The defect mode is TM/plasmonic in nature. (d) Another profile in the y-z plane of the electric energy density of the α' defect mode of the photonic crystal. This mode is TE/photonic in nature in contrast to the α defect mode. (e,f) Electric energy density profiles of bands A (plasmonic) and E (photonic) in the plasmonic crystal. The white dashed lines represent the cross-section plane of the paired image. (g,h) Electric energy density profiles of bands A' and E', which correspond to the plasmonic crystal modes A and E, respectively. Band A' is a TM wave and turns into a plasmon wave with the introduction of metal, while Band E' is a TE wave and stays photonic in the plasmonic crystal geometry as well.
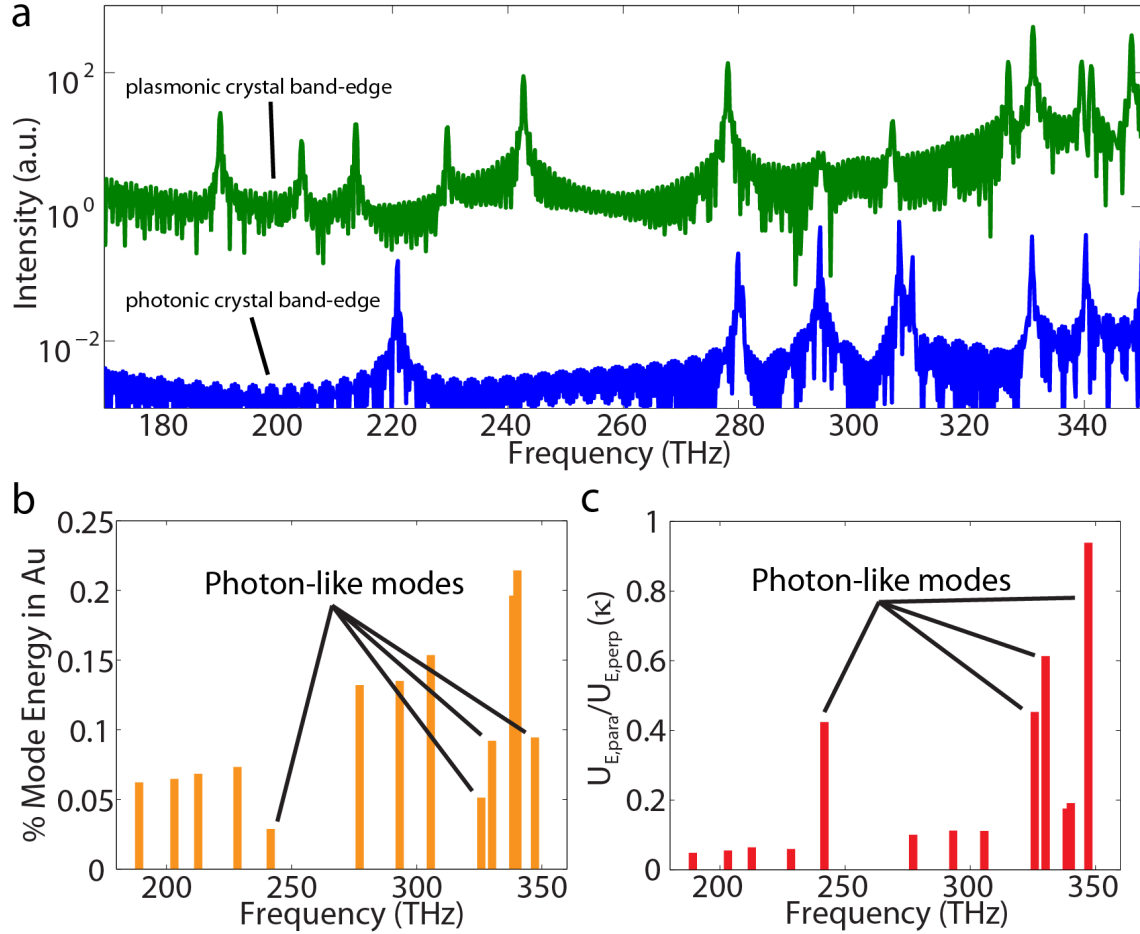
Figure 4.4. We show various characteristics of travelling waves in plasmonic crystals. (a) A semi-log plot of the various travelling waves present in a one-dimensional plasmonic (green) and photonic (blue) crystal. The modes have wave-vectors of $k_z = \pi/a$ (at the Broullion zone edge). There are 13 (9) distinct bands between 170-350 THz in the plasmonic (photonic) crystal. The modes were elucidated through a time-domain based simulation of a periodic crystal and excited by a broadband point-dipole source. The intensity of the resonance is unimportant since it depends on how well the point-dipole source coupled to a particular travelling wave. (b) A plot of the percentage of energy in metal for a particular mode's electromagnetic configuration. Low amounts of energy in the gold implies that a wave is photon-like. (c) A plot of κ, or the fraction of energy present in the parallel versus perpendicular components of the electric field 10 nm above the gold-semiconductor interface over a unit cell of the crystal. Large κ indicates that the metal is behaving more like a reflector for a photon-like mode.

successfully confine plasmons in a SPPC. As an example, we show the simulated dispersion of the device shown in Figure 4.8a (Figures 4.3a and 4.9a) and experimentally observe emission of the C and D plasmonic bands (Figure 4.9b). In simulation, pseudo-bandgaps appear at the edge of the Brillouin zone between bands A and B and also between bands C and D (Fig. 4.3a).
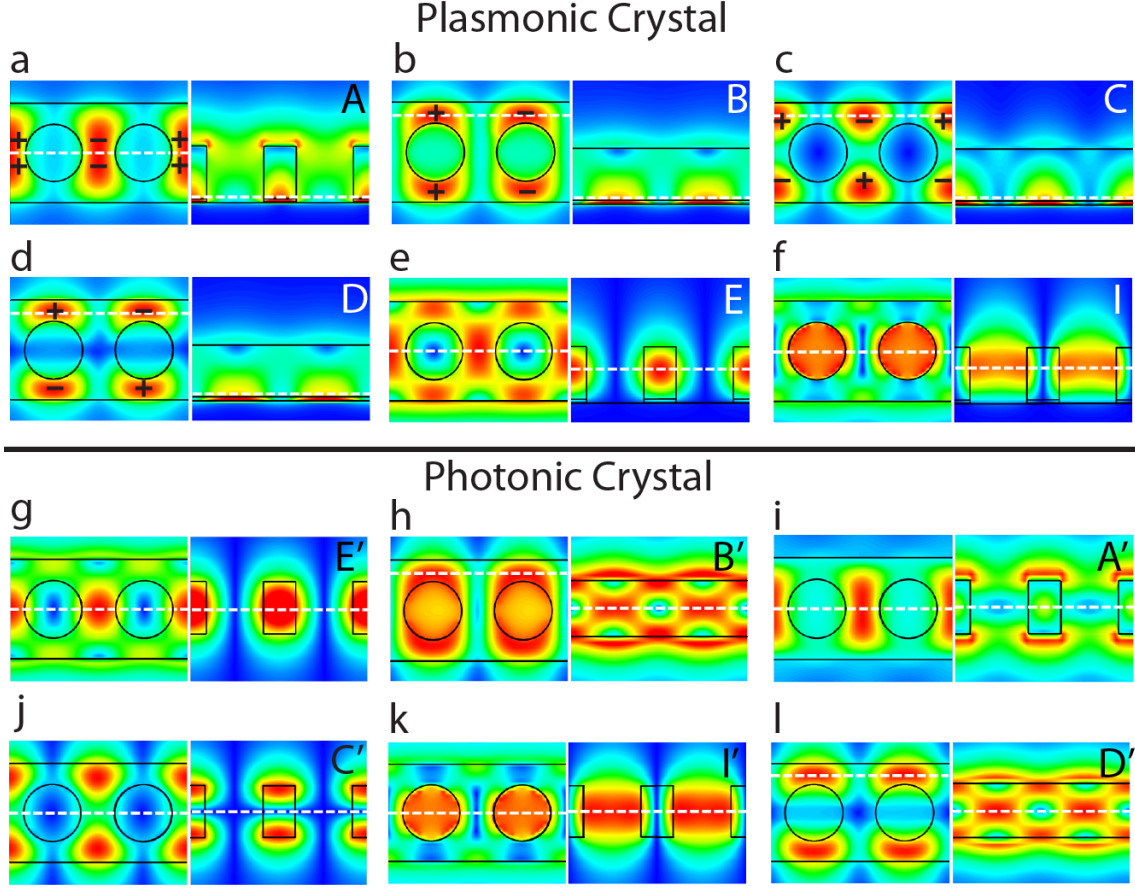
Figure 4.5. We compare plasmonic and photonic crystal band-edge waves. We show the effects of the metal film on the various TE and TM modes of a photonic crystal at the band edge. The TM modes interact strongly with the metal and are converted to surface plasmon waves with a large reduction in resonance frequency. The TE modes maintain their photonic characteristics. The unprimed (e.g. Band A) and primed (e.g. Band A') notation is used to represent the same travelling wave with (unprimed) and without (primed) the metal film. (a,b,c,d,e,f) The electric field magnitude plots of the first four plasmonic bands (A-D) and the first two photonic bands (E,I) are presented for a SPPC. The charge distribution of the plasmon-like (TM) bands (A-D) are overlaid on the field distribution plots. The plot on the left side of each pair is a color plot of $|\vec{E}|$ in the x-z plane specified by the dashed white line in the right figure. The plot on the right represents $|\vec{E}|$ in the y-z plane along the dashed white line in the left figure. Bands A,B,C,D,E,and I resonate at 190, 204, 214, 229, 243, and 327 THz, respectively. (g,h,I,j,k,l) In a similar manner, we show the electric field magnitude plots of the first six bands for a photonic crystal in order of increasing resonance frequency (E', B', A', C', I', and D' resonate at 222, 282, 283, 295, 310, and 312 THz, respectively). The field profiles are plotted in the same manner as (a-f).

The first four plasmon-like (TM) and first two photon-like (TE) bands of the plasmonic crystal with dimensions $w = 380\ nm$, $a = 343\ nm$, and $d = 220\ nm$ and a photonic crystal

with same dimensions (without the bottom metal film) are plotted in Fig. 4.5. The first four plasmon bands of the SPPC exist also in the photonic crystal, but do not exhibit a bandgap and exist at much higher frequencies (e.g. A' resonates at 280 THz while A resonates at 190 THz). Again, we find that the TM bands interact strongly with the metal film and become plasmon waves at frequencies lower than the first TE band of the crystal structures. The metal film also splits the degeneracy of A' and B' and creates a TM bandgap where it did not exist in the photonic crystal. Finally, the gold film also breaks the symmetry of a photonic crystal in the y-direction, causing the photonic modes (TE) that exist in the purely dielectric crystal (Figs. 4.5g, 4.5k) to blue-shift as well (Fig. 4.3).

(a)

	α	β	γ	δ
Q_{total}	71	73	90	143
$Q_{radiation}$	308	438	2380	3550
Q_{loss}	92	88	94	149
$V_{effective}/(\lambda/n)^3$	0.1	0.15	0.3	0.7
Confinement Factor	67%	62%	63%	76%
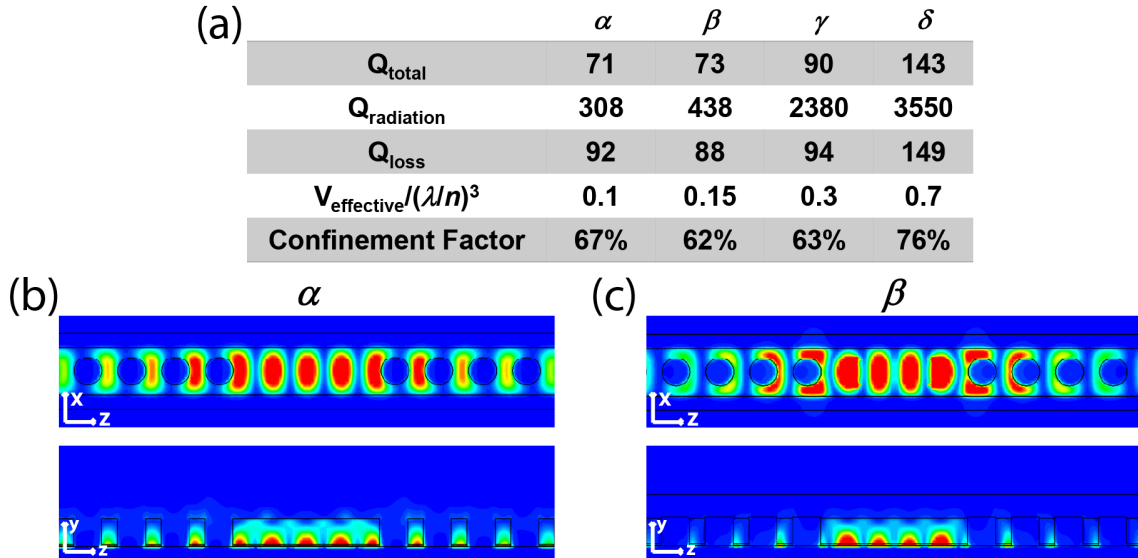
Figure 4.6. (a) Summary table of relevant laser parameters of the first four eigenmodes of a 3-hole defect in a one-dimensional plasmonic crystal. (b,c) The top and side profiles of the electric field magnitude of the α and β defect modes. Both modes are surface plasmon modes that decay evanescently from the gold/semiconductor interface.

After understanding the behavior of a periodic crystal, the properties of various crystal defects can be understood. By removing three air-holes in the SPPC, we form a localized surface plasmon cavity that can support multiple plasmonic resonances. The creation of TM bandgaps due to metal interaction with the one-dimensional cyrstal creats two bandgaps of interest, Δ_1 and Δ_2 (Fig. 4.3a). The first TM pseudo-bandgap is Δ_1 =14 THz and is where the first two defect modes α and β are located. The bandgap is imperfect since band C redshifts at lower wavevectors into the 1st bandgap's energy range. However, any defect mode within this bandgap does not easily couple to band C since there is a large k-vector and parity mismatch between the two waves. Thus, we can achieve high mode confinement with small radiation rates. The bandgap between bands C and D is Δ_2 =17 THz and is where the third defect mode γ is located. Again, the bandgap is not a complete gap since band B blue shifts at small wavevectors into the forbidden energy region; however the γ defect mode will not couple well to band B since there is a large wavevector and parity mismatch between the two modes. Finally, the δ defect mode resides at frequencies higher than band D and begins

to show some photonic characteristics. However, there are very large perpendicular fields present at the metal-semiconductor interface, suggesting a plasmonic nature to the mode.

The differences between the defect modes in SPPCs and photonic crystals are large. I illustrate the differences using the fundamental defect modes (α and α') for the plasmonic and photonic crystals shown in Figs. 4.3c and 4.3d. The α' mode resonates at 235 THz and is TE, while α resonates at 193 THz and is TM; the photonic crystal would have to be roughly 1.25 times larger to match the plasmonic crystal resonance frequency (more size reduction is expected in visible frequencies due to the nature of surface plasmon wavevectors). If we define the electromagnetic mode volume of the lasing mode as:

$$V_{eff} = \frac{\int \frac{\partial \omega \epsilon(\vec{r}, \omega)}{\partial \omega} |\vec{E}(\vec{r})|^2 d^3 r}{\max \left(\frac{\partial \omega \epsilon(\vec{r}, \omega)}{\partial \omega} |\vec{E}(\vec{r})|^2 \right)}$$

then the photonic crystal defect has $V_{eff,\alpha'} = 0.6 \ (\lambda_0/n)^3$ while the plasmonic defect mode has a volume of $V_{eff,\alpha} = 0.1 \ (\lambda_0/n)^3$. Thus, the plasmonic α defect electromagnetic mode volume is 6 times smaller than the photonic counterpart!

We show a summary of different relevant laser parameters for the first four defect modes of a 3-hole cavity in a plasmonic crystal in Fig. 4.6a. We also show the mode profiles for the α and β defect modes in Figs. 4.6b and 4.6c, respectively. Experimentally, we did not see lasing from the first two defect modes, probably because of the use of a necessary Ti adhesion layer [82] and insufficient gain. The metal underneath the semiconductor is as smooth as the initial semiconductor surface due to the nature of the fabrication process. However, after RIE etching, the metal surface surrounding the device is roughened, although the exact average roughness was not measured.

4.2   Fabrication Procedure

We made the devices using the $In_x Ga_{1-x} As_y P_{1-y}$ quaternary semiconductor system. With the low surface recombination velocity characteristic of phosphide-based materials compared to materials such as GaAs [83], such a system is attractive for nanoscale devices where the surface to volume ratio is large. The fabrication process is based on a semiconductor membrane, and therefore can by applied to very large scale integration (VLSI) on silicon in future optical interconnect applications.

First, an epitaxial wafer was purchased (Landmark Optoelectronics Inc.) with an n-InP substrate, a 50 nm $In_{0.53}Ga_{0.47}As$ etch stop layer (lattice matched), a 10 nm u-InP barrier layer, a 200 nm $In_{0.53}Ga_{0.47}As$ active layer, and a final 10 nm u-InP barrier layer grown by MOCVD techniques. It is important to note that this wafer can easily be modified to incorporate electrical injection of carriers by properly doping the thin barrier layers sandwiching the 200 nm thick active layer.

Next, the substrate was cleaned with organic solvents, dipped in 49% hydrofluoric acid for five seconds, and then rinsed in water to remove the native oxide. Immediately after,

the sample was placed into a load-lock to deposit 5 nm of titanium dioxide. The titanium dioxide serves as a dielectric (although it is a large-bandgap semiconductor) to prevent carriers from thermalizing into the metal layer (see Fig. 4.2). The titanium dioxide was deposited using atomic layer deposition (ALD) in a Picosun Sunale R150 reactor with titanium tetraisopropoxide and water precursors. The growth temperature for the oxide was 275°C. After oxide deposition, metal was evaporated onto the substrate. Titanium (3 nm) followed by gold (80 nm) was deposited onto the semiconductor using electron beam evaporation. The rates of evaporation were kept low (less than 1 $\mathring{A}$ per second) and the substrate was never allowed to heat up past 75°C. The chamber pressure was around $5{\times}10^{-6}$ Torr during evaporation.

The substrate was then flipped and bonded to a carrier wafer. Initially, a glass slide was cleaned very carefully, a small drop of NOA-81 UV-curable epoxy was placed onto the semiconductor substrate (on the metal side), and the glass slide was placed on top of the substrate so that a thin layer of epoxy was sandwiched by the glass slide and semiconductor substrate. All air bubbles were removed from the interface. The sample was then placed under a UV light to cure.
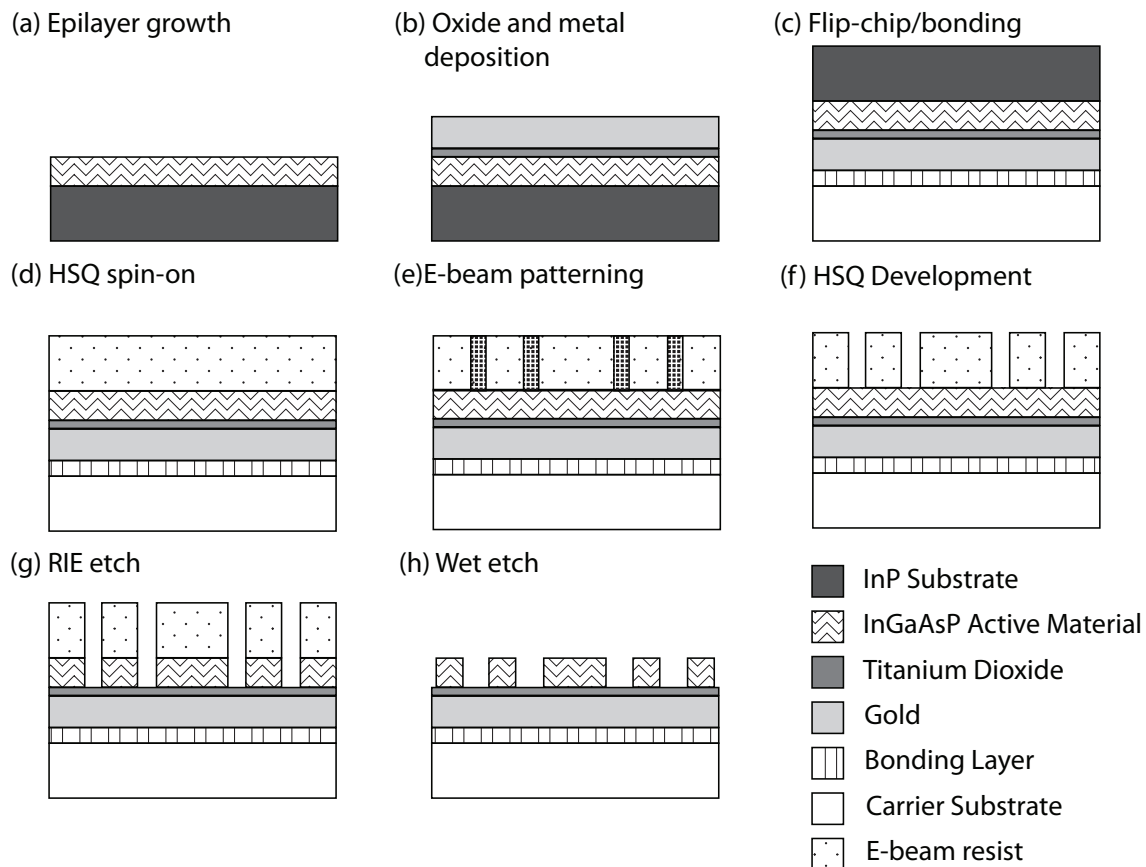
Figure 4.7. A simplified flow chart of the fabrication to build plasmonic crystal defect nanolasers.

Once the epoxy was cured, the chip was mounted on a manual lapping machine, and

mechanically grinded on sandpaper until only 50 μm of the original substrate was left. Then the sample was cleaned with acetone and placed into a 1:1 HCl:H3PO4 acid solution at 50°C. The etching rate of this solution was approximately 5 $\mu m/min$. After the entire substrate was removed, the sample was washed in deionized water and dried. The etch stop layer (made out of $In_{0.53}Ga_{0.47}As$) was subsequently removed using a 1:1:10 H_2SO_4:H_2O_2:H_2O etch for 3 seconds. The sample was then rinsed in water.

Negative e-beam resist was spun onto the substrate immediately after the etch stop was removed. Hydrogen silsesquioxane (FOX-12, Dow Corning) was spun onto the substrate at 2500 rpm for 1 minute. The sample was then baked at 90°C for 40 minutes [84]. This lithography step can also be easily accomplished using conventional optical lithography since the features are larger than 200 nm in most cases.

The resist was then exposed by electron-beam lithography (Crestec CABL-9510CC) with a 50 kV beam. The dose given to the resist was between 300-700 $\mu C/cm^2$. The optimal dose was identified to be around 450 $\mu C/cm^2$. After exposure, the sample was developed in 12.5% TMAH in water at room temperature for 12 seconds. High concentration TMAH solutions were found to increase the contrast of the HSQ resist, although higher doses were needed to expose the resist. The sample was rinsed in water and dried using a nitrogen gun.

Reactive ion etching was used to perform an anisotropic dry etch to define a single plasmonic crystal device (with HSQ acting as an etching mask). The semiconductor was etched using hydrogen and methane gases. A custom-built plasma-thermal parallel plate plasma etcher (RIE) was used. The chamber was first cleaned using oxygen plasma for 1 hour. Around 15% methane in hydrogen at roughly 35 milliTorr of etching pressure and a self-bias of $\sim$500 V resulted in an etch rate of roughly 20 nm/min. The RF power used was 50 mW/cm^2. After dry etching the substrate, the sample was wet etched to remove the resulting damage associated with reactive ion etching. First, the sample was placed in 30% hydrogen peroxide and rinsed in water. Then the sample was placed in 49% hydrofluoric acid to remove the oxidized semiconductor. One such cycle removed roughly 10-15 nm of semiconductor from the sidewalls. This process was repeated three times to effectively clean the sidewalls of the devices [85].

4.3 Experimental Verification of Lasing

In the SPPC, I observed lasing from the γ and δ defect modes. The α and β defect modes were not experimentally observed in this study due probably to insufficient gain with the current material system and the use of titanium as an adhesion layer between the gold and semiconductor interface. In the future, low-loss metals and high-gain semiconductors should elucidate these modes. The γ mode's eigenfrequency is in the second pseudo-bandgap between bands C and D. The presence of the C and D bands and the γ mode was experimentally verified in Figs. 4.9a and b. I show a scanning electron micrograph (SEM) of a device where the third defect mode lases dominantly in Fig. 4.8a. Finally, δ resonates at energies larger than modes in the D band (Fig. 4.3a).

The devices probed were cooled to 77 Kelvin in a cryostat (Janis ST-500) using liquid nitrogen, and then optically pumped using a 1064 nm laser operating in pulsed mode (QPhotonics WFBGLD-1060-200). The input-output power characteristics of the lasers were probed using pump light with pulse widths of 8 ns and a duty cycle of 0.016%. The peak power of the pump was around 28 mW. I build a custom micro-photo-luminescence setup mounted on an automated stage (Sutter MP-285) to probe the sample. The laser light was collected through a 0.8 NA 100X objective and sent simultaneously to a two-dimensional IR-CCD (Sensors Unlimited Inc.) to image the lasing mode and a spectrometer coupled to a liquid nitrogen cooled InGaAs CCD array (PI Acton OMA-V) to record the light spectrum. The laser mode images in Figs 4.8f-4.8g and 4.10f-4.10g are taken with the nanolaser and objective focal plane mismatched by $\sim$10 μm to better resolve the radiation pattern of the lasers. The theoretical resolution limit of the spectrometer system is around 0.1 nm.

4.3.1 Lasing of the γ-defect

Out of the many working devices that were fabricated, I have chosen one to illustrate lasing from the γ defect mode (Fig. 4.8a). Taking geometrical measurements from SEM, I simulated the entire device using 3D Finite Integral techniques (FIT), and the computed eigenfrequencies of various resonances agreed well with experimental data (Fig. 4.9). Using micro-photoluminescence, I verified that the band edge modes appeared brightest when the edge of the device was optically pumped, whereas the defect mode only lased when the center of the device was pumped. In almost all instances, I saw lasing from band edge modes as well (see below). To further verify that the γ-mode was lasing, I imaged the radiation from the device (Figs. 4.8f-g). These polarization-resolved patterns were compared to simulated far-field radiation directivity of the γ-defect mode (Figs. 4.8d-e). There is strong qualitative correspondence between the measured and simulated patterns. Also, in both simulation and experiment, the z-polarized light was 10 times weaker than the x-polarized light.

The γ defect mode is purely a surface plasmon mode, with evanescent decay in both the metal and semiconductor (Figs. 4.9b and 4.9c). The modal volume of the simulated structure is $V_{eff} = 0.30 \ (\lambda_0/n)^3$, where $n = 3.5$ is the index of InGaAsP. The third photonic defect mode (γ') has a mode volume of 3 $(\lambda_0/n)^3$ (λ_0 is 970 nm), making the plasmonic crystal defect 10 times smaller in electromagnetic mode volume. The mode is also confined in the semiconductor so that $\sim$66% of the mode's energy resides in the gain media, where the electric energy density is defined as:

$$U = \int \frac{\partial \omega \epsilon(\vec{r}, \omega)}{\partial \omega} |\vec{E}(\vec{r})|^2 d^3 r$$

This defect mode can have a cold-cavity quality factor at room temperature of $Q_{Ag} = 330$ if silver is used with no Ti adhesion layer, Q_{Au}=90 if gold is used without a Ti adhesion layer, and Q_γ=33 if gold is used with a 3 nm Ti adhesion layer (assuming bulk Ti properties). With the current design, the radiation quality factor is Q_{rad}=2380. In our fabrication, we used Ti/Au even though the quality factor of the cavity is lower due to ease of fabrication. The lasing spectrum at maximum pumping power of the γ-defect laser can be seen in Fig.
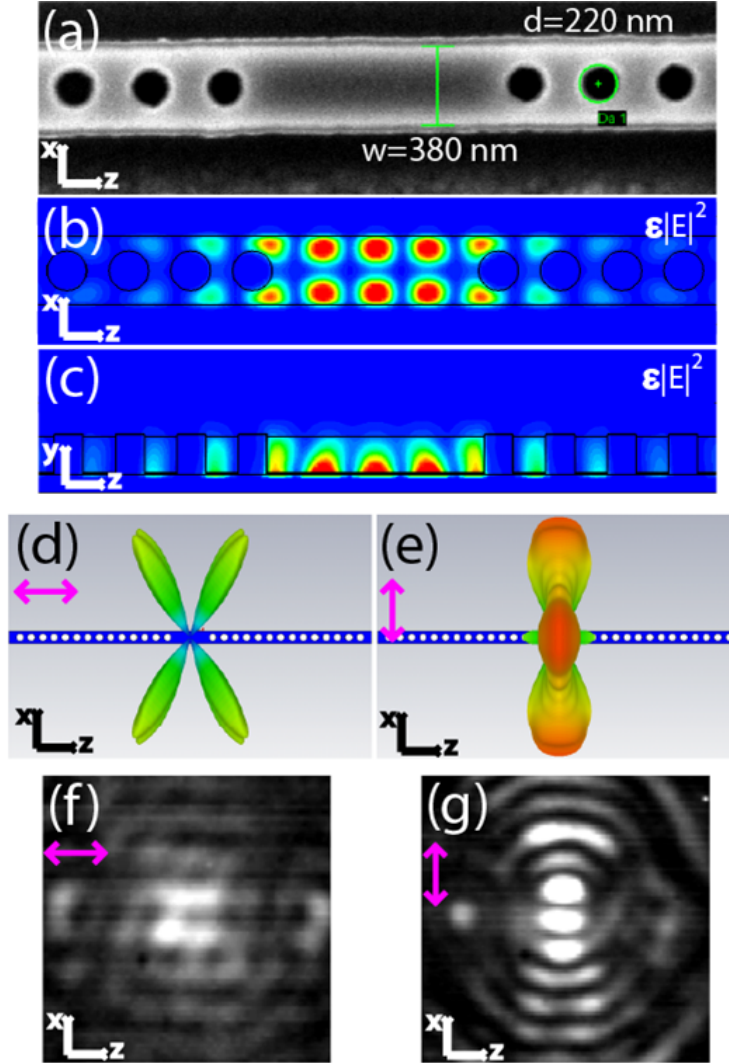
Figure 4.8. We observed lasing in the γ defect mode of a SPPC and now present the electromagnetic properties of a γ-defect nanolaser. (a) An SEM micrograph of a device in which the γ defect mode lases. It has a lattice constant of a=343 nm. (b,c) The top (x-z) view and the side (y-z) view of the electric energy density of the γ defect resonance. The mode decays evanescently from the metal-semiconductor interface. (d,e) The simulated z-polarized and x-polarized far-field radiation directivity of the γ defect mode. The device is shown for reference. The total z-polarized radiation is computed to be 10 times weaker than the x-polarized radiation. (f,g) Experimentally obtained z-polarized and x-polarized images of the γ lasing mode. The image plane is $\sim$5μm above the device plane to clearly resolve the radiation pattern. The total z-polarized radiation is measured to be 8 times weaker than the x-polarized radiation. The simulated and experimental polarized mode patterns match well confirming the presence of the plasmonic γ defect nanolaser.

4.9c. I found the threshold pumping power to be $\sim$100 kW/cm^2. However, this threshold is artificially high, since not all the pump power was absorbed by the structure due to

69
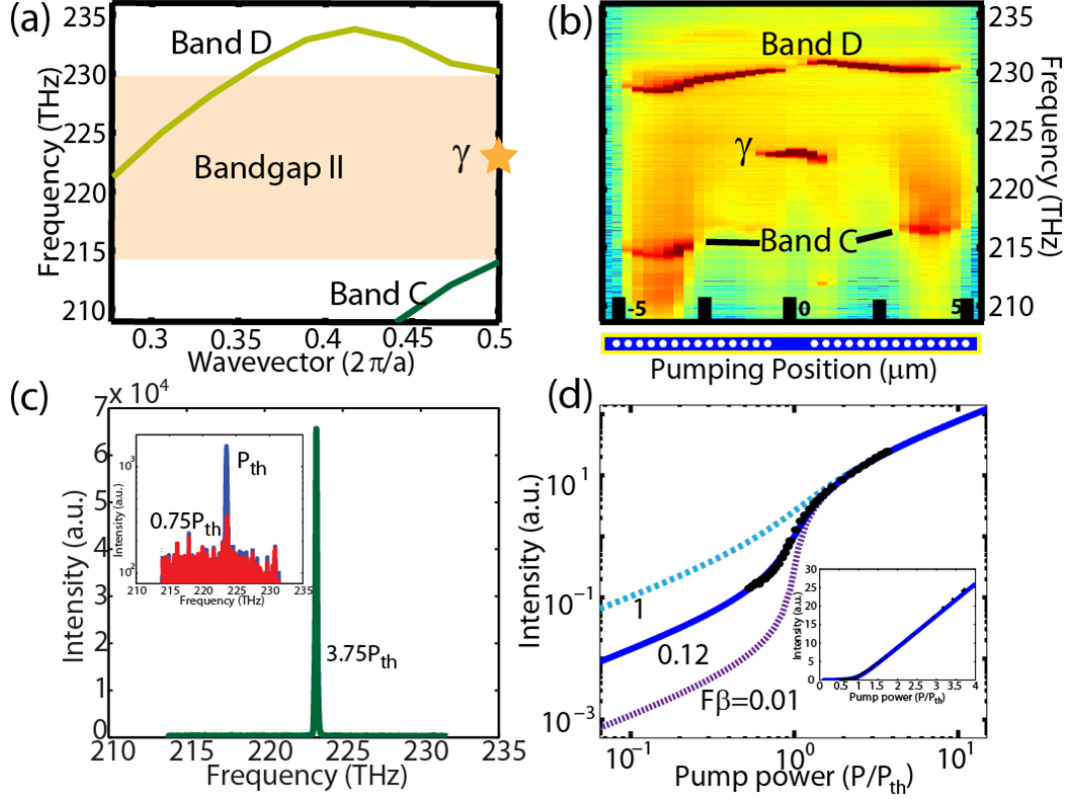
Figure 4.9. Laser characteristics of the γ-defect laser mode. (a) The simulated plasmonic dispersion, bandgap, and defect location of the device in Fig. 4.8a. The position of the γ defect is seen between band C and band D with a resonance frequency near 224 THz. (b) The spectra obtained from the device shown in Fig. 4.8a versus pump position along the device (the spot size is $\sim 3 \mu$m). Away from the center of the device, bands C and D are observed and confirmed through agreement with simulation in (a). The third defect begins to lase when the device is pumped in the device center (where the defect is located). (c) The lasing spectra of the γ defect mode. The linewidth of the nanolaser reaches a minimum value of 0.5 nm. The inset shows the laser spectrum in semi-log scale below and at threshold pump power. (d) The input-output power characteristics (L-L curve) of the γ defect in log-log scale. Using rate equation models, it is estimated that the device has large spontaneous emission coupling into the laser mode with $F\beta = 0.122$. L-L curves with $F\beta = 0.01$ and $F\beta = 1$ are shown for comparison to the obtained data (black circles). Also, the L-L curve is plotted in linear scale (inset).

its size. I also found the linewidth of the laser to be to 0.5 nm at maximum pumping power. The peak wavelength of the device also stabilized as lasing was reached, since carrier dependent refractive index changes are stabilized due to carrier clamping. We also analyzed the pump-power-dependent light output (L-L curve) for the γ-defect mode. I show the integrated intensity from the defect cavity mode in Fig. 4.9d. The spontaneous emission rate is enhanced in the nanocavity due to high coupling of spontaneous emission into the laser mode (β) and the Purcell effect ($F = (16/n^2)(Q/V_{eff})(\lambda_0/n)^3$). The light output

characteristics of the nanolaser (L-L curve) were analyzed using rate equations and previously published material parameters (see below). Taking into account the above effects regarding spontaneous emission, a good fit of the experimental data was obtained using a rate equation model with a fitting parameter $F\beta = 0.122$ (Fig. 4.9d).

4.3.2   Lasing of the δ-defect

The δ defect mode also underwent laser oscillations at 77K. For the δ defect mode, I measured the device shown in Fig. 4.10a. The device has dimensions w=400 nm, d=186 nm, and a=343 nm. The electric energy density is even along the x-y symmetry plane and odd along the y-z symmetry plane (Figs. 4.10b and 4.10c). I calculated the mode volume to be $V_{eff} = 0.67 \, (\lambda_o/n)^3$, where $n = 3.5$. Also, the confinement factor (fraction of energy in the gain media) is Γ 76%. The radiation rate is smaller than the γ mode with $Q_{rad} = 3550$, total quality factor $Q_{Au} = 143$, and $Q_\delta = 52$ if a 3 nm Ti adhesion layer is used. Theoretically, if silver was used, a total $Q_{Ag} = 620$ could have been achieved.

For the δ-defect, when the device was pumped off-center, the dominant lasing modes were attributed to band-edge lasing (Band D). When the defect region was pumped, a different frequency mode began to lase (the δ mode). The experimental frequencies of the different resonances corroborated well with the eigenfrequencies of a simulated device with the exact dimensions (Figs. 4.11a and 4.11b) of the device in Fig. 4.10a. To further verify the presence of the δ mode, I imaged the lasing device at maximum pump power in both orthogonal polarizations (same procedure as the γ mode). The mode images in both polarizations (Fig.s 4.10f and 4.10g) matched the simulated far-field directivity radiation pattern well (Figs. 4.10d and 4.10e) in both polarizations and thereby confirmed that the δ defect mode was excited. In simulation, the integrated x-polarized light was 12 times brighter and the z-polarized light. In experiment, we observed that the x-polarized light was 10 times brighter and the z-polarized light.

The laser properties for the δ-defect were measured by taking pump-power-dependent spectra from pump powers ranging from 0.7-4.6 P_{th} (where P_{th} is the threshold pump power of the laser, Fig. 4.11c). This threshold power was P_{th}=90 kW/cm^2 for the δ-defect nanolaser. I measured the linewidth to be 0.4 nm at maximum pump power. This linewidth, again, is probably artificially broad due to the thermal effects of pumping the laser with a pulsed source. The δ mode also had enhanced spontaneous emission due to its small size with the best fitting standard rate equation model having $F\beta = 0.061$ (see below). The L-L behavior of the δ-laser is shown in Fig. 4.11d.
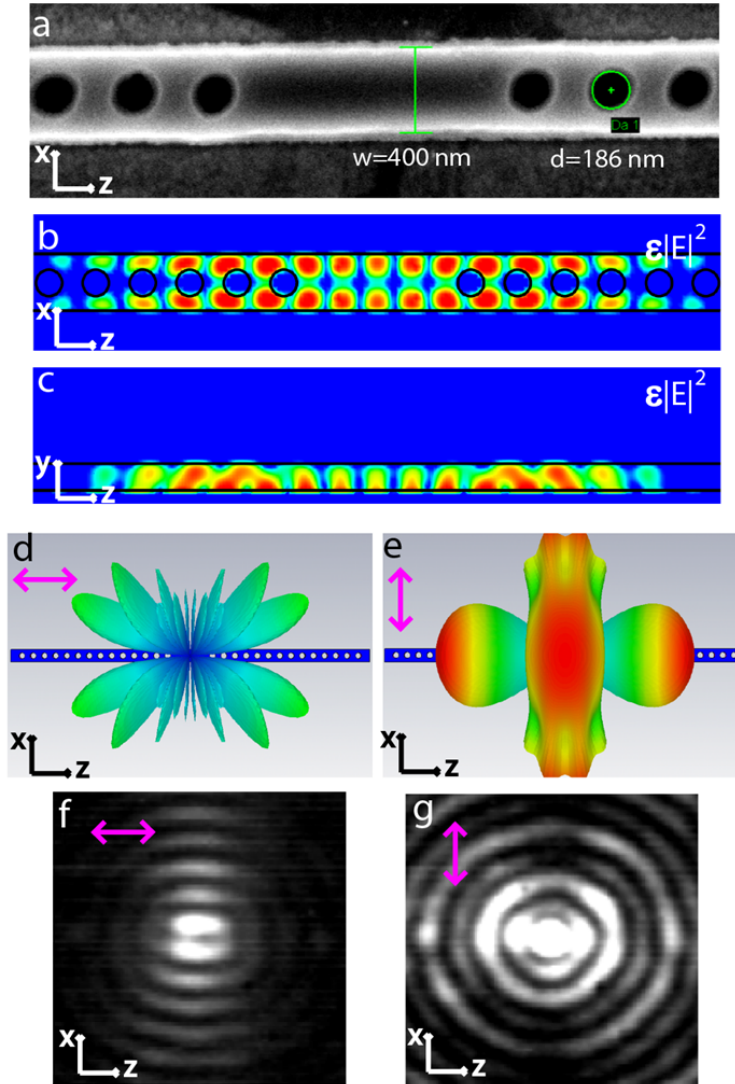
Figure 4.10. We show δ-defect mode electromagnetic properties. (a) A top view SEM of the measured δ-defect nanolaser. (b,c) The top and side view profiles of the electric energy density profile of the δ mode. Red indicates max energy density, and blue indicates minimum energy density. The device geometry is outlined in black lines and was determined from SEM measurement of the lasing device. (d,e) Plots of the directivity of the radiation resulting from a δ-defect resonance. Red indicates large directivity, and blue indicates small directivity. The device geometry is shown in the background as a reference. Radiation with z-polarized light is seen in (d) while radiation with z polarized light is shown in (e). (f,g) Experimentally obtained polarization-resolved images of the δ-defect mode during laser oscillation.
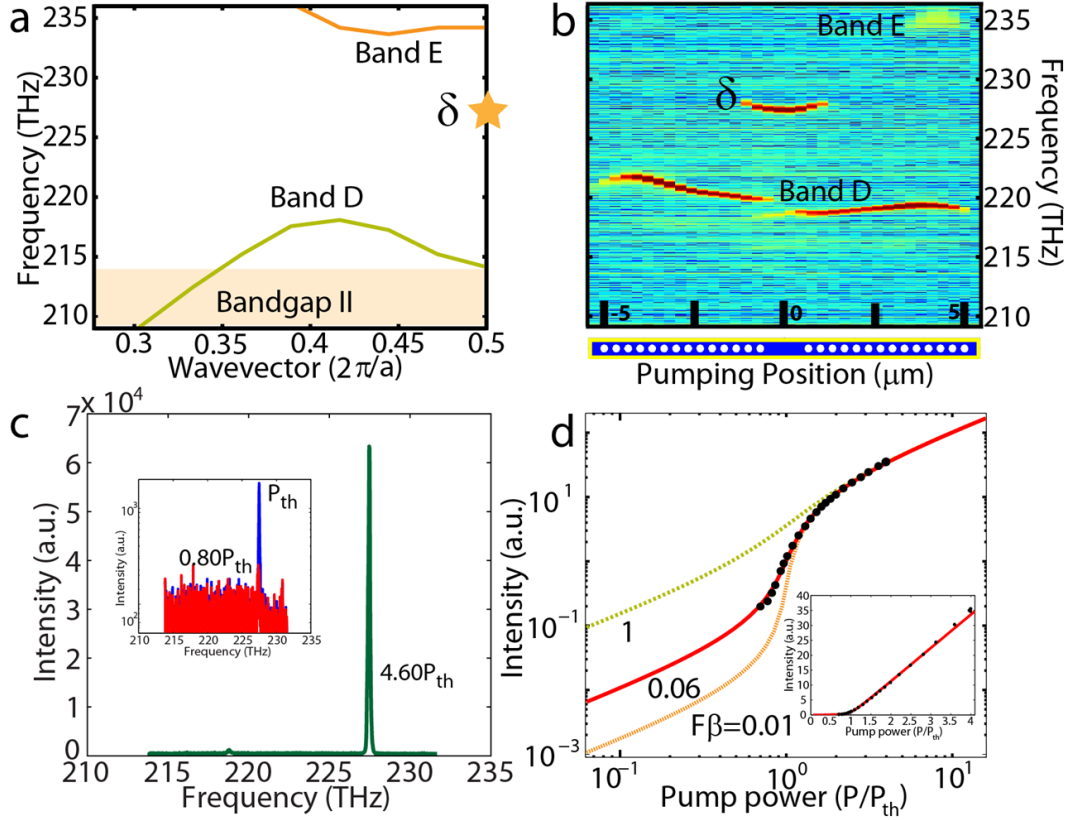
Figure 4.11. Laser characteristics of the δ-defect mode. (a,b) A comparison of the simulated plasmonic crystal band structure (a) and position-dependent pumping of the nanolaser (b) shown in Fig. 4.10a. The frequencies of the various resonances match very well. The defect mode is only excited when the device is pumped in the center where the defect is located. Otherwise, the band-edge modes exclusively lase at frequencies well-matched between experiment and simulation. (c) The spectrum of the lasing device is shown at 4.6 times the threshold pump power. The inset shows in semilog scale the laser spectrum below ($0.8P_{th}$) and at P_{th}. (d) L-L curve of the δ-defect nanolaser in log-log scale and linear scale (inset). The black dots represent experimentally obtained data while the lines represent modeled curves based on standard rate equation analysis. The model and experiment fit well when $F\beta = 0.06$. L-L curves with $F\beta = 1$ and $F\beta = 0.01$ are shown for comparison.

73

4.3.3 Additional Laser Properties

I fit the input-output power curves of both lasers using carrier and photon rate equations used elsewhere [45]:

$$\frac{dN}{dt} = P - g(N)S - \frac{1-\beta}{\tau_{sp}}N - \frac{F\beta}{\tau_{sp}}N - \frac{v_s S_a}{V_a}N \tag{4.1}$$

$$\frac{dS}{dt} = \Gamma g(N)S - \frac{S}{\tau_{ph}} + \frac{\Gamma F\beta}{\tau_{sp}}N \tag{4.2}$$

where N and S are carrier and photon densities, P is the input power, $g(N)$ is the assumed to be a linear gain model for the semiconductor ($g = ca(N - N_0)/n_g = 1.1 \times 10^{-5}(N - 4 \times 10^{17})$ s^{-1}), where c is the speed of light, n_g is the group index, and a is the gain coefficient), β is the fraction of spontaneous emission coupled to the laser mode, F is the Purcell factor, $v_s = 2 \times 10^4$ cm/s is the surface recombination velocity, S_a is the active volume surface area, V_a is the active gain volume, Γ is the laser's confinement factor, and τ_{sp} is the bulk spontaneous emission lifetime (1.5 ns), and τ_{ph} is the cavity photon lifetime ($\tau_{ph} = Q/(2\pi f)$, Q is the cavity's quality factor, f is the resonance frequency.

In order to calculate a realistic Purcell enhancement, I needed to measure an experimentally determined quality factor for each mode. However, because of loss and gain within the semiconductor material, an accurate measurement of quality factors is difficult. The quality factor of plasmonic crystal lasers is metal-loss dominated, and thus should improve at low temperatures. The lowest measured quality factor for the γ-mode was $Q_{meas} = 250$ (see Fig. 4.12), and the lowest measured quality factor for the δ-mode was $Q_{meas} = 950$. Yet, these quality factors are probably do not represent the actual nature of the defect cavity. Thus, in fitting the $F\beta$ product for each L-L curve, I used a range of values for quality factors of the cavity, keeping in mind that previously published results suggest that metal loss is decreased by 5 times at 77K relative to room temperature [38]. There is also uncertainty in the mode volume used in the Purcell factor calculation, since not every carrier recombines that the point of maximum energy density. I present a summary for different $F\beta$ products using various quality factors in Table 4.1. In the table, I would suggest that the quality factors near 5 times the simulated quality factors (including Ti loss) are most accurate, and the simulated mode volumes are accurate. The change in $F\beta$ product is modest at best with quality factor variation, suggesting that a relatively good model for spontaneous emission can be ascertained even with uncertainty in cavity quality factors and mode volumes.

I also collected additional data concerning the linewidth and peak wavelength of the γ- and δ-defect modes in Fig. 4.12. The peak wavelengths for both modes initially blue shift, then red shift, and finally slowly blue shift as the laser operates beyond lasing threshold (Figs. 4.12a and 4.12c). These data suggest that in both lasing devices, there is a competition between thermal heating causing redshift and band-filling causing blue shift in the peak wavelength of the lasers. The pump dependent line-width of each mode is shown in Figs. 4.12b and 4.12d. The linewidth broadens at high pump powers. This suggests that the laser frequency changes during the duration of one pulse (i.e. it is chirped). However, this explanation still needs to be verified.

Table 4.1. We show the change in $F\beta$ product versus potential values the quality factor of the two defect modes that are observed. We suggest that Q_{model}, which is 5 times the simulated quality factor using bulk metal dispersion for gold and titanium is the best guess for actual fit. We also show the $F\beta$ factor using the lowest obtained experimental quality factor, Q_{exp}, for comparison with the suggested fit.

γ-laser	Q	F	β	$F\beta$
$0.1Q_{model}$	18	1.53	0.060	0.090
$0.33Q_{model}$	60	5.11	0.018	0.092
Q_{model}	180	15.33	0.008	0.122
Q_{exp}	250	21.29	0.006	0.126
$10Q_{model}$	1800	153.26	0.003	0.383
δ-laser				
$0.1Q_{model}$	25	1.07	0.032	0.034
$0.33Q_{model}$	82	3.53	0.012	0.042
Q_{model}	250	10.69	0.005	0.053
Q_{exp}	950	40.61	0.003	0.110
$10Q_{model}$	2500	106.88	0.002	0.214
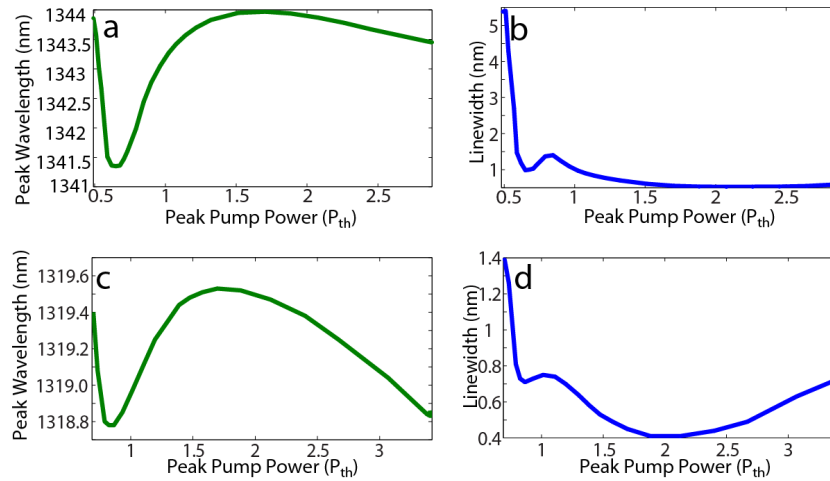
Figure 4.12. (a,b) The peak wavelength and linewidth for the laser shown in Fig. 4.8a. (c,d) The peak wavelength and linewidth, for the laser shown in Fig. 4.10a.

Finally, as I have already mentioned, laser oscillations also occur for plasmon waves at the edge of the Broullion zone of the plasmonic crystal since the group velocities of the travelling modes go to zero. Thus, very large gain can be achieved for bandedge modes in plasmonic crystal cavities. For instance, I present the lasing characteristics of band D in Fig. 4.13. In band D, the group velocity approaches zero at the band edge and at $k \sim 0.42(2\pi/a)$ (Fig. 4.3a). Lasing in a plasmonic band mode seemed to behave very classically with a sharp threshold, as seen in the pump vs. intensity characteristics of the representative device in Fig. 4.13c.
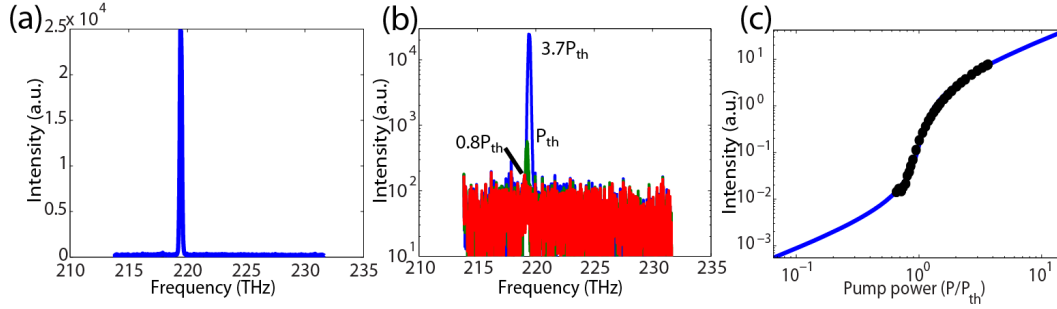
Figure 4.13. Lasing obtained from a band-edge mode (band D). (a) I show a lasing spectrum obtained at a peak pump power of 380 kW/cm^2. (b) The semi-log scale pump-dependent spectra for the band-mode. (c) The L-L curve shows that the band-edge mode behaves the most classically, with a sharper threshold than both the γ- and δ-defect modes. Since the exact nature of the bandedge mode is not known, the mode volume and quality factor of the mode cannot be used to find the Purcell enhancement and spontaneous emission coupling present in this mode. The threshold pump power for this device is 55kW/cm^2 of peak power.

Chapter 5

Nanopatch Lasers

Although surface plasmons have the ability to exceed the diffraction limit by transducing photons to electrical currents, metal-optics can provide tight confinement of light as well purely by reflecting radiation [38, 45–50]. To reduce the physical and electromagnetic modal size of optical nanocavities further using metal-optics, techniques used in the microwave community can be borrowed. The microstrip resonator, used at microwave frequencies for various applications including antennas and filters, provide a robust method of creating high quality factor cavities with tunable radiation profiles [86, 87]. The use of circular patch cavities in the optical regime has been proposed and theoretically studied by Manalatou and Rana [88]. The paper focuses mainly on the fundamental cavity modes for this particular cavity geometry. However, using higher order modes can be beneficial in obtaining higher quality factors, and also engineering the radiation pattern of such cavity structures.

In this dissertation, resonant structures inspired by microstrip resonators are used to create moderate quality factor cavities in near-infrared wavelengths. The cavities demonstrated include circular and rectangular nanopatch cavities. Each cavity shape has advantages, and they will be demonstrated throughout the chapter. Many other cavity designs, such as nanoring lasers, are also possible. The basic geometry of nanopatch cavities can be seen in Fig. 5.1. The cavities are integrated with an active compound semiconductor gain medium (InGaAsP) to produce a nanolaser. Because these lasers operate in near-infrared frequencies, metal behaves much more ideally than in visible wavelengths. Thus, the shrinking of devices due to the plasmonic effects (large kinetic inductance [54]) can be considered a second order effect. Thus, metals can be used in their traditional roles, with the exception that there is large resistive loss in the near-infrared wavelength range. Using these metal-optic effects, lasing is achieved in the two most fundamental modes with moderate quality factors in a cylindrical resonator, and lasing is also achieved in rectangular nanopatch cavities. I achieve physical laser volumes as low as 6 $(\lambda_0/2n)^3$: a world-record-setting small laser cavity.
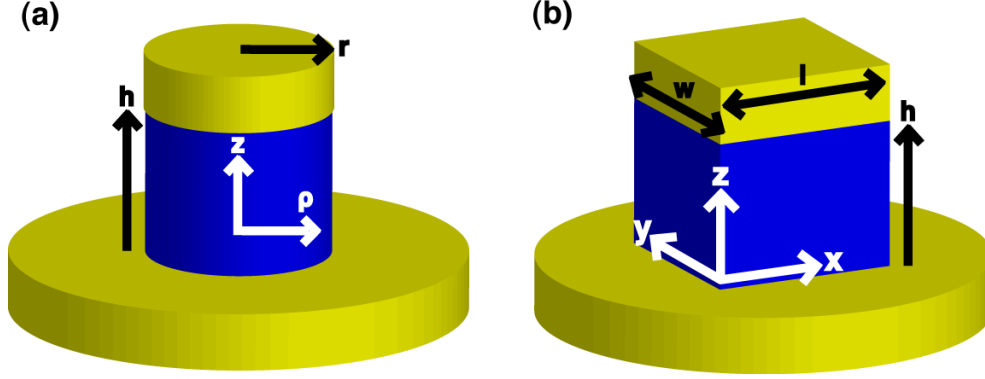
Figure 5.1. A schematic of (a) circular and (b) rectangular nanopatch cavities. Yellow regions represent gold and blue areas signify InGaAsP semiconductor gain media.

5.1 Analytical Modelling and Simulation

5.1.1 Analytical Model

Nanocavities with metal covering the top and bottom and sidewalls exposed can be analyzed analytically using the first-order Cohn model to predict mode profiles and resonance frequencies [89]. The analysis, although only an approximation, gives the general trend of how cylindrical and rectangular nanocavities will behave as a function of geometry. In the model, the metal is assumed to be a perfect electrical conductor (PEC) with some skin depth (Δ) associated with the amount of energy present in the real metal for any particular mode. The semiconductor sidewall is assumed to be a perfect magnetic conductor (PMC, tangential magnetic field is assumed to be zero at the semiconductor-air interface). This particular approximation is excellent in the microwave regime, where dielectric constants can be extremely high ($\epsilon_r \sim 100$)[90]. Even though at optical frequencies the dielectric constant of semiconductor is $\epsilon_r \sim 12$, this approximation is still surprisingly accurate in predicting the energy dispersion versus geometry for many eigenmodes of nanopatch cavities.

Starting from the Helmholtz equation, $(\nabla^2 = k^2)\vec{E} = 0$, a general solution in cylindrical coordinates is:

$$E_{\rho,\phi,z}(\rho,\phi,z) = \sum_{m=0}^{\infty}\sum_{p=0}^{\infty}\left[\alpha_{mp}J_m\left(\rho\sqrt{k^2+p^2}\right) + \beta_{mp}Y_m\left(\rho\sqrt{k^2+p^2}\right)\right] \times$$
$$[c_m\cos(m\phi) + d_m\sin(m\phi)]\left[f_p e^{-pz} + g_p e^{pz}\right]$$

where $k^2 = \omega^2\mu\epsilon$, m is the azimuthal mode number, p is the axial mode number (and eigenvalue),J_m is a Bessel function of the first kind, and Y_m is a Bessel function of the second kind.

Transverse magnetic (TM) and transverse electric (TE) solutions exist in nanopatch cavity structures. The notation TM_{mnp} and TE_{mnp} can be used to annotate a particular eigenmode for any cavity structure, where m, n, and p represent the azimuthal, radial,
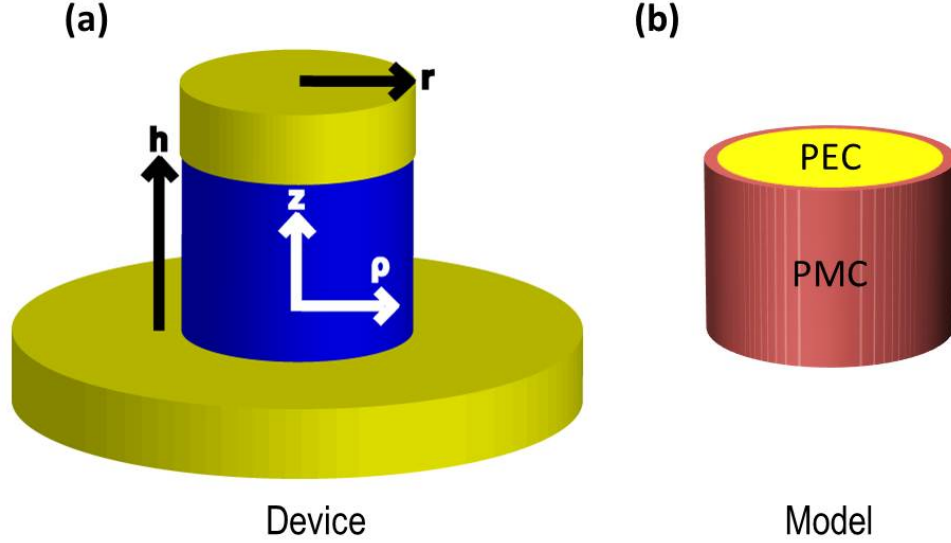
Figure 5.2. (a) The schematic of the nanopatch cavity structure and (b) the corresponding optical resonator model with perfect conductor boundary conditions. The top and bottom surfaces are perfect electrical conductors (PEC), while the cylinder sidewall is a perfect magnetic conductor (PMC).

and axial mode numbers, respectively. In general, m, n, and p are non-negative integers. However, due to the PEC boundary, the axial mode number, p, cannot be 0 ($p = 1, 2, 3,$) in TE solutions. Since the smallest root of the Bessel functions and their derivatives is $\chi_{11} \approx 1.841$, the fundamental mode among the TM_{mnp} and TE_{mnp} modes is the TM_{110} mode. However, this cavity mode is an extremely efficient radiator, and unsuitable for laser cavities. Thus, the next eigenmode, the TM_{111} mode, will be referred to as the fundamental mode of the nanopatch geometry. Under a PEC boundary condition, surface plasmon polariton waves near the metal-dielectric interface do not exist. However, electromagnetic waves can still interact with metal surfaces and form loosely-bound Sommerfeld-Zenneck waves [91, 92].

It is only necessary to solve for one field component (E_z for TM modes and H_z for TE modes), since the others can be obtained through Maxwells equations:

$$
\left.\begin{aligned}
E_z &= P(x,y)\cos(p\pi z/h) \\
E_\perp &= -\frac{p\pi}{h\alpha^2}\sin(p\pi z/h)\nabla_\perp P \\
H_\perp &= -\frac{i\omega\epsilon}{\alpha^2}\cos(p\pi z/h)\hat{z}\times\nabla_\perp P
\end{aligned}\right\} TM
\qquad
\left.\begin{aligned}
H_z &= P(x,y)\sin(p\pi z/h) \\
E_\perp &= -\frac{i\omega\mu}{\alpha^2}\sin(p\pi z/h)\hat{z}\times\nabla_\perp P \\
H_\perp &= -\frac{p\pi}{h\alpha^2}\cos(p\pi z/h)\nabla_\perp P
\end{aligned}\right\} TE
$$

where $\alpha^2 = \omega^2\mu\epsilon - (p\pi/h)^2$.

For example, the TM_{111} mode (the most fundamental moderate quality factor mode) has

a mode profile:

$$E_z(\rho, \phi, z) = -E_0 J_1(\beta_{\rho,TM_{111}}\rho) \cos(\pi z/h) \sin(\phi)$$

$$E_\rho(\rho, \phi, z) = -E_0 \frac{\pi}{h\beta_{\rho,TM_{111}}} J_1'(\beta_{\rho,TM_{111}}\rho) \sin(\pi z/h) \sin(\phi)$$

$$E_\phi(\rho, \phi, z) = -E_0 \frac{\pi}{h\rho\beta_{\rho,TM_{111}}^2} J_1(\beta_{\rho,TM_{111}}\rho) \sin(\pi z/h) \cos(\phi)$$

where $\beta_{\rho,TM_{111}} = 2\pi\sqrt{\lambda_{TM_{111}}^{-2} - (2h)^{-2}}$, h is the height of the cavity, and only one of the two degenerate modes is shown for simplicity. A vector plot of the TM_{111} mode is seen in Fig. 5.3.
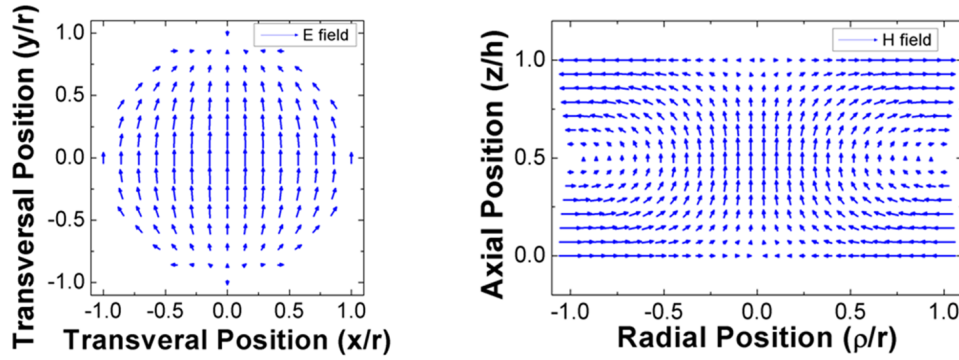
Figure 5.3. (a) The electric field profile of the electric dipole mode (TM_{111}) at the cavity mid-plane ($z = h/2$). (b) The magnetic field profile of the magnetic dipole mode (TE_{011}) at the vertical cross-section ($\phi = 0, \pi$).

The most fundamental TE mode has a mode profile:

$$H_z(\rho, \phi, z) = -H_0\beta_{\rho,TE_{011}}^2 J_0(\beta_{\rho,TE_{011}}\rho) \sin(\pi z/h)$$

$$H_\rho(\rho, \phi, z) = H_0 \frac{\pi\beta_{\rho,TE_{011}}}{h} J_0'(\beta_{\rho,TE_{011}}\rho) \cos(\pi z/h)$$

$$E_\phi(\rho, \phi, z) = iH_0\omega\mu\beta_{\rho,TE_{011}} J_0'(\beta_{\rho,TE_{011}}\rho) \sin(\pi z/h)$$

$$H_\phi(\rho, \phi, z) = E_z(\rho, \phi, z) = E_\rho(\rho, \phi, z) = 0$$

where $\beta_{\rho,TE_{011}} = 2\pi\sqrt{\lambda_{TE_{011}}^{-2} - (2h)^{-2}}$.

More generally, the eigenvalues for a cylindrical cavity can be derived from the Helmholtz equation:

$$\lambda_{TM_{mnp}} = \frac{2\pi\sqrt{\epsilon}}{\sqrt{\left(\frac{\chi_{mn}'}{r}\right)^2 + \left(\frac{p\pi}{h+2\Delta_{TM_{mnp}}}\right)^2}} \tag{5.1}$$

$$\lambda_{TE_{mnp}} = \frac{2\pi\sqrt{\epsilon}}{\sqrt{\left(\frac{\chi_{mn}}{r}\right)^2 + \left(\frac{p\pi}{h+2\Delta_{TE_{mnp}}}\right)^2}} \tag{5.2}$$

where ϵ is the materials dielectric constant, χ_{mn} (χ'_{mn}) is the nth zero of the (derivative of the) mth Bessel function, p is the axial mode number, r is the cavity radius, h is the cavity height, and Δ is the penetration depth of the mode energy into the metal caps of the cavity. From these general equations, dispersion relations relating cavity dimensions and eigenenergies can be found. In Fig. 5.4, the dispersion relation for various cavities is plotted for different modes of cylindrical cavities. Different modes, owing to differing amounts of energy present in the metal, have different effective skin depths that provide a good approximation to finding the eigenenergies of cylindrical cavities with different radii and heights.
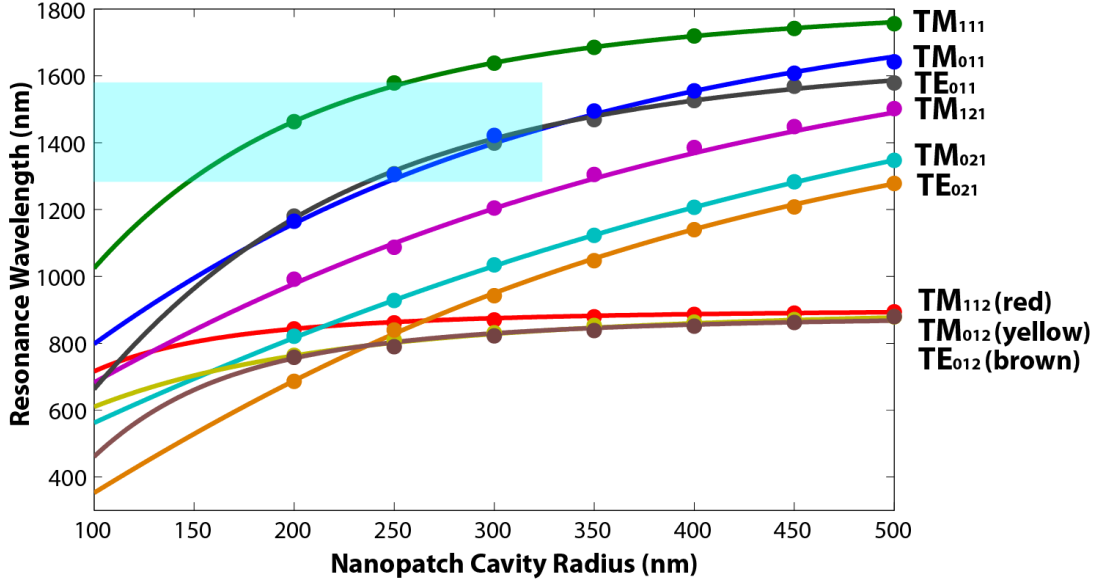
Figure 5.4. The theoretical (solid line) and simulated (points) dispersion of various eigenmodes of cylindrical cavities is shown. Good agreement is obtained between theory and simulation once effective skin depths are accounted. The shaded blue area represents the parameter space observed experimentally (see below).

Rectangular nanopatch cavities can also be analyzed using the solution for the Helmholtz equation in rectangular coordinates:

$$E_{x,y,z}(x,y,z) = \sum_{m=0}^{\infty}\sum_{p=0}^{\infty}(\alpha_m e^{mx} + \beta_m e^{-mx})(c_n e^{ny} + d_n e^{ny})\times$$
$$(f_{mn}e^{i\sqrt{k^2+m^2+n^2}} + g_{mn}e^{i\sqrt{k^2=m^2=n^2}})$$

where $k^2 = \omega\mu\epsilon$, and m and n are mode numbers and eigenvalues associated with the x and y directions, respectively.

Rectangular cavities behave similarly to cylindrical cavities, except that the eigenenergies are obtained using the Helmholtz equation in Cartesian coordinates. The modes of rectangular cavities can be labeled as TM_{abc}, where a, b, and c represent mode numbers associated

with the length (l), width (w), and height (h) of the cavity, respectively (Fig. 5.1b). The TM mode has an electric field profile:

$$E_z = E_0 \cos(a\pi x/l) \cos(c\pi z/h)$$

$$E_x = E_o \frac{ac\pi^2}{hl\beta^2} sin(a\pi x/l) \sin(c\pi z/h)$$

and eigenvalues:

$$\lambda_{TM} = \frac{2\pi\sqrt{\epsilon}}{\sqrt{\left(\frac{a\pi}{l}\right)^2 + \left(\frac{b\pi}{w}\right)^2 + \left(\frac{c\pi}{h}\right)^2}}$$

where $\beta^2 = \mu\epsilon\omega_{a0c}^2 - (c\pi/h)^2$ and only x-polarized mode profiles are shown for simplicity. Magnetic modes (TE) also exist in rectangular patch geometries, however, only the fundamental TM mode of such cavities was studied. Rectangular cavities can be especially interesting given that anisotropic devices can be used to control the polarization of light that is emitted by a TM mode. Rectangular cavities can also be used to resonantly pump nanopatch cavities [93]. Since nanopatch cavities are subwavelength, pumping schemes require the structure to be resonant at the pump wavelength for efficient transfer of energy. The rectangular cavity can be designed with anisotropy, so that one polarization has a cavity resonance at the desired emission wavelength, and the other polarization has a strong resonance at the pump frequency. Resonant pumping schemes can drastically reduce pump-induced heating by making the cavity couple more efficiently to the excitation source, and anisotropic rectangular patch cavities can be tuned to accomplish such goals.

5.1.2   Simulation of Nanopatch Cavities

Cylindrical nanopatch cavities capped by two parallel metal planes were simulated by FEM (COMSOL Multiphysics) and FDTD (MEEP; Lumerical FDTD Solutions) numerical Maxwell equation solvers. The axial symmetry of the cavity geometry in cylindrical coordinates can be exploited to reduce an inherently three-dimensional electromagnetic problem into a computationally simple two-dimensional one [94, 95]. Gold was modeled by using an experimentally found frequency-dependent complex dielectric constant at room temperature [52]. I further characterized the complex permittivity of our evaporated gold films using ellipsometry (GESP broadband variable angle ellipsometer, Sopra) from 200 to 800 nm wavelength at room temperature, and the data agreed very well with the values published in the literature. Titanium layers are neglected in our simulation. Frequency dependent refractive indices were used for both InP and $In_{0.4}Ga_{0.6}As_{0.85}P_{0.15}$ materials with slight adjustment by a maximum value of $\Delta n = -0.1$ from the nominal equilibrium values to include carrier band-filling effects. The refractive index of TiO_2 was set to 2.4. Although this value is uncertain and depends on the atomic layer deposition quality, the sensitivity of TiO_2 index variation is minimal since most of the electromagnetic field is confined to the semiconductor region.

FEM simulation utilized a two-dimensional axially symmetric eigenvalue solver to identify eigenmodes in each azimuthal number [94]. The boundary condition at zero radius was set to
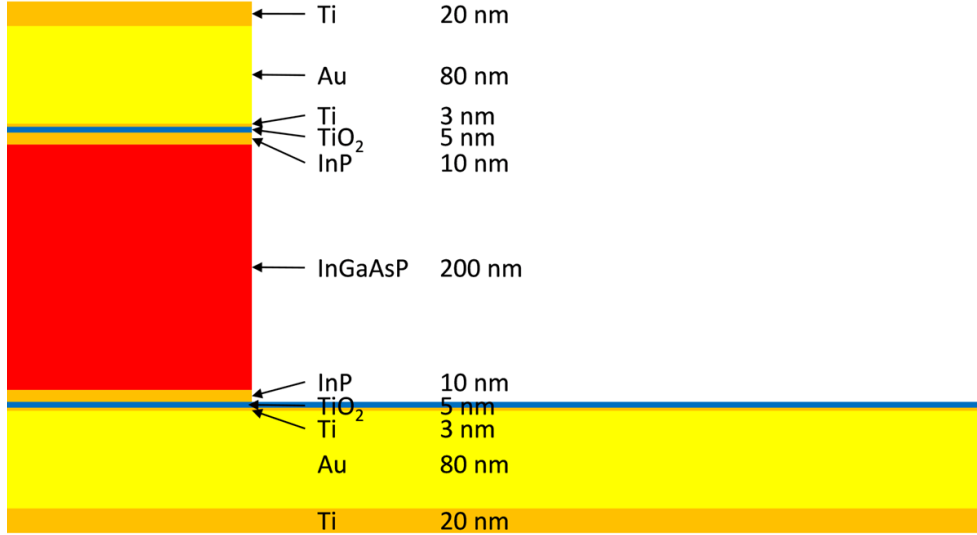
Figure 5.5. The simulated layer structure. Because of axial symmetry, only half cross-section is shown.

null, and the remaining boundaries were set to match the impedance of the outgoing radiation of the cavity mode. These boundary conditions allow radiation to dissipate without spurious reflections. The InGaAsP layer thickness was 200 nm, the InP caps were 10 nm thick each, and the TiO$_2$ films are 5 nm thick on each side. There is a 80 nm thick gold ground plane terminating at the simulation boundary (Fig. 5.5).

I chose the nanopatch dimensions such that the two most fundamental modes were discovered to be within the gain spectrum of InGaAsP. For example, when the radius is 250 nm, the electric (TM_{111}) and magnetic dipole (TE_{011}) modes were found at 1533 nm and 1360 nm, respectively, which are in good agreement with experimental observations (Fig. 5.14a). More specifically, for the electric dipole mode with the resonant wavelength of $\lambda_{TM} = 1420$ nm ($r = 203$ nm), the gold permittivity used was $\epsilon_{Au} = -120 - 13.5i$, the InGaAsP index was $\epsilon_{InGaAsP} = 11.83$, and the InP index was $\epsilon_{InP} = 9.67$. For the magnetic dipole mode ($\lambda_{TE} = 1380$ nm, $r = 265$ nm), $\epsilon_{Au} = -86 - 9.3i$, $\epsilon_{InGaAsP} = 3.58$, and $\epsilon_{InP} = 3.18$. The mode profiles for the first two modes (the TM_{111} and the TE_{011} resonances) are shown in Fig. 5.6.

I also determined the effective mode volume of the cavity using FEM simulations. Depending on the azimuthal mode number, m, the effective mode volume V_{eff} must be calcu-
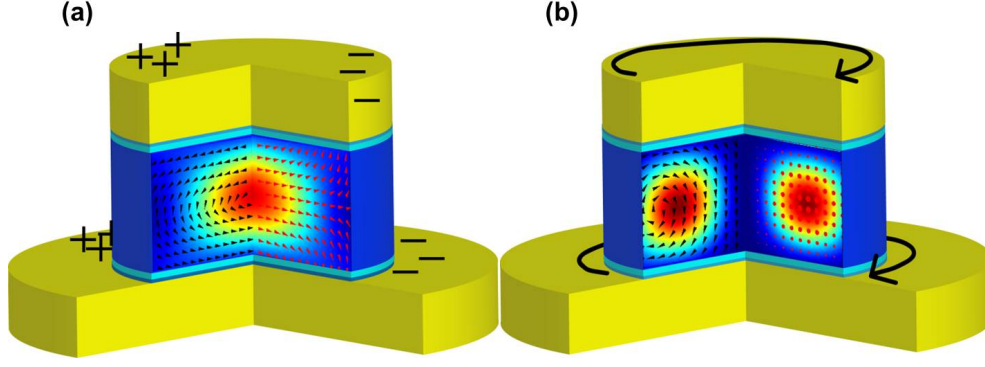
Figure 5.6. (a, b) Computed mode profiles for the two lowest order modes: the electrical dipole mode (TM_{111}, a) and the second-order magnetic dipole mode (TE_{011}, b). The surface color at the cross-section represents the electrical energy density, and the arrows show the direction of the electric (red) and magnetic (black) field. The nanopatch radius and height are $r = 250\ nm$ and $h = 230\ nm$, respectively. The effective modal volumes are $0.54(\lambda_{TM}/2n_{eff})^3$ and $2.99(\lambda_{TE}/2n_{eff})^3$, where n_{eff} is the effective refractive index of the dielectric layers. In the metal layers, free charges (a) and currents (b) arise to satisfy the boundary condition at the metal-dielectric interfaces.

lated differently as follows:

$$
\begin{aligned}
V_{eff} &= \frac{\int \frac{\partial \omega \epsilon(r,\phi,z)}{\partial \omega} E^2(r,\phi,z)dV}{\max\left(\epsilon(r,\phi,z)E^2(r,\phi,z)\right)} \\
&= \frac{\int \int \frac{\partial \omega \epsilon(r,\phi,z)}{\partial \omega} E^2(r,z)rdrdz \int_0^{2\pi} \cos^2(m\phi)d\phi}{\max\left(\epsilon(r,\phi,z)E^2(r,\phi,z)\right)} \\
&= \frac{2\pi \int \int \frac{\partial \omega \epsilon(r,\phi,z)}{\partial \omega} E^2(r,z)rdrdz}{\max\left(\epsilon(r,\phi,z)E^2(r,\phi,z)\right)}, m = 0 \\
&= \frac{\pi \int \int \frac{\partial \omega \epsilon(r,\phi,z)}{\partial \omega} E^2(r,z)rdrdz}{\max\left(\epsilon(r,\phi,z)E^2(r,\phi,z)\right)}, m \geq 1
\end{aligned}
$$

where the azimuthal dependence of each mode is taken into consideration as a $\cos(m\phi)$ dependence. Since not all dipole emitters are located in the electric field maximum, an alternate definition of the modal volume can be obtained by replacing the maximum electric energy density in the denominator with the average energy density over the gain volume [38]. When V_{gain} is the gain volume, the average modal volume, V_{ave}, is given by:

$$
V_{ave} = \frac{\int \frac{\partial \omega \epsilon(r,\phi,z)}{\partial \omega} E^2(r,\phi,z)dV}{\frac{1}{V_{gain}} \int_{gain} \epsilon(r,\phi,z)E^2(r,\phi,z)dV}
$$

However, since carrier diffusion within the material will allow carriers to migrate to regions of high spontaneous recombination rates, the true mode volume for the Purcell factor calculation will most likely fall between the conventional effective modal volume, V_{eff}, and the averaged modal volume, V_{ave} [38].

The effective mode volumes, V_{eff}, for the electric and magnetic dipole modes, estimated from simulations, are $0.54(\lambda_{TM}/2n_{eff})^3$ and $2.99(\lambda_{TE}/2n_{eff})^3$, respectively, where n_{eff} is the effective refractive index of the laser cavity. All of the electric field within the whole simulation volume was considered, and the electromagnetic energy contained in the metal layers was taken into account by using the relation $\epsilon_{metal} = d(\omega\epsilon)/d\omega$. The effective modal volume of the TE_{011}-like magnetic dipole mode is comparable to that of other previously reported monopole whispering gallery modes in the near-infrared region [96], although the nanopatchs physical size is much smaller. We also found that the normalized modal volumes do not vary much with the cavity size and corresponding resonance wavelength. The average modal volume for the fundamental mode was found to be $V_{ave} = 1.45(\lambda/2n)^3$. For the magnetic dipole mode, the effective and average modal volume were $V_{eff} = 2.99(\lambda/2n)^3$ and $V_{ave} = 7.44(\lambda/2n)^3$, respectively.

The optical confinement factor of a cavity mode is given by:

$$\Gamma = \frac{\int_{gain} \frac{\partial\omega\epsilon(r,\phi,z)}{\partial\omega} E^2(r,\phi,z)dV}{\int_{cavity} \frac{\partial\omega\epsilon(r,\phi,z)}{\partial\omega} E^2(r,\phi,z)dV}$$

and was also obtained from FEM simulation results through numerical integration. The optical confinement factor for the electrical and magnetic dipole modes are 0.84 and 0.89, respectively.

The quality factor of each eigenmode was also simulated using finite difference time domain simulations (MEEP). Different cavities were simulated with silver and gold as the metal layers. Fig. 5.7 shows electric and magnetic energy densities for various modes of cylindrical cavities. Generally, the TM modes have field lines that terminate in metal, causing large metal absorption. These modes can be more clearly understood as charge distributions in the metal that create certain mode configurations. TE modes are magnetic in nature, and have only azimuthal electric fields.

The energy loss of metallodielectric cavities is dominated by radiation and metallic loss so the total cavity quality factor can be decomposed as $Q_{tot}^{-1} = Q_{rad}^{-1} + Q_{loss}^{-1}$. The radiation quality factor, Q_{rad}, can be found by setting the imaginary part of the metal permittivity to be zero and thereby removing the resistive metallic loss. A perfectly matched layer was used to absorb all radiation from the cavity [97]. I found that the total quality factor of the electric dipole mode was $Q_{tot,TM} = 65$, while $Q_{rad,TM} \sim 1600$. Therefore, losses in this mode were dominated mainly by energy dissipation in the metal layers. For the TE_{011} mode, I the quality factors to be $Q_{tot,TE} = 80$ and $Q_{rad,TE} = 205$, indicating more efficient radiation from the cavity.

For other higher order modes, the total ($Q_{tot,Ag}$, $Q_{tot,Au}$), radiation (Q_{rad}), and loss ($Q_{abs,Ag}$, $Q_{abs,Au}$) quality factors were calculated for each metal. The confinement factor Γ and normalized electromagnetic mode volume $V_n = V_{mode}/(\lambda_0/n)^3$ (where $V_{mode} = \int \epsilon(\vec{r})|\vec{E}(\vec{r})|^2 d3r / \max(\epsilon(\vec{r})|\vec{E}(\vec{r})|^2)$) were also found for each eigenmode. A summary of the above figures of merit is shown in table 5.1 for cylindrical cavity eigenmodes.

Finally, I used Lumerical FDTD software to find the far field radiation pattern of the TM_{111} and the TE_{011} modes. The two modes were excited with point dipole sources with a
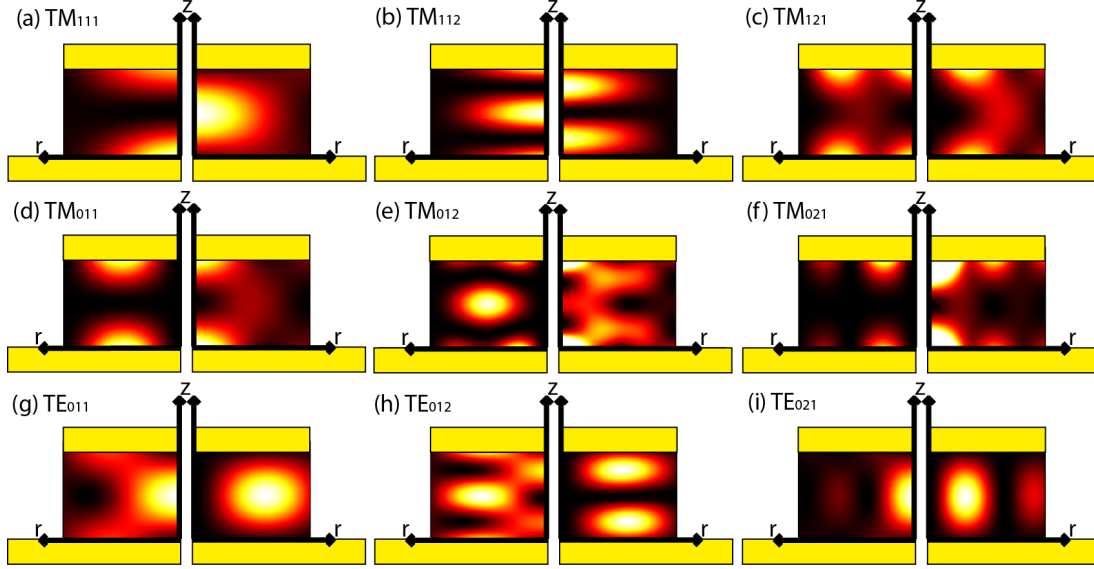
Figure 5.7. Magnetic (left) and electric (right) energy densities of various eigenmodes of cylindrical nanopatch cavities are shown. The first row shows modes with odd parity ($m = 1$), the second and third rows shows modes with no angular dependence ($m = 0$). The first two rows show TM modes while the third row shows TE modes. Each mode profile is labeled according to the mode it represents.

finite bandwidth from $\lambda = 1100\ nm$ to $\lambda = 1700\ nm$. The TM_{111} mode, which transforms like an electric dipole, can be excited from a point source in the exact middle of the active region. The TE_{011} mode, which has no azimuthal dependence, can be excited with four dipoles located at the edge of the semiconductor active region with azimuthal polarization. The simulation volume was a 2 μm^3 cubical volume with the cavity located at the bottom center of the simulation box. PML boundary conditions were used to eliminate spurious reflections [97]. The small volume where the cavity was located was finely meshed with a mesh size of 5 nm. The simulation was run for 200 fs, and the source was active for the first $40fs$ of the simulation. Although the field in the cavity had not decayed significantly by the end of the simulation time due to a high cavity quality factor, the simulation was stopped to shorten simulation run time. Early termination of the simulation did not affect the results obtained, since only far-field data was desired from the simulation. Finally, to get rid of artifacts in the frequency domain data due to the excitation source, apodization was used to eliminate the source fields from data analysis using a soft step function reaching an amplitude of 1 after the source fields had decayed.

Far field calculations were made using exact near-to-far field transformations using field equivalence principles. A closed box of six field monitors was placed around the cavity to capture the near field of the cavity mode. The apodized tangential surface electric and surface magnetic fields were used as radiation sources to determine the radiation pattern of the cavity. The far field pattern was found using a numerical implementation of the

Table 5.1. Summary of pertinent cavity parameters for various eigenmodes of a cylindrical nanopatches

	TM_{111}	TM_{112}	TM_{121}	TM_{021}	TM_{012}	TE_{011}	TE_{012}
$Q_{tot,Ag}$	250	350	116	155	460	143	240
$Q_{tot,Au}$	65	120	61	62	128	80	128
Q_{rad}	1600	500	167	298	3000	205	325
$Q_{abs,Ag}$	295	100	380	323	540	473	917
$Q_{abs,Au}$	68	150	96	78	133	131	211
Γ	0.84	0.93	0.62	0.70	0.90	0.89	0.95
V_n	0.54	1.17	1.35	1.55	6.4	2.99	7.0
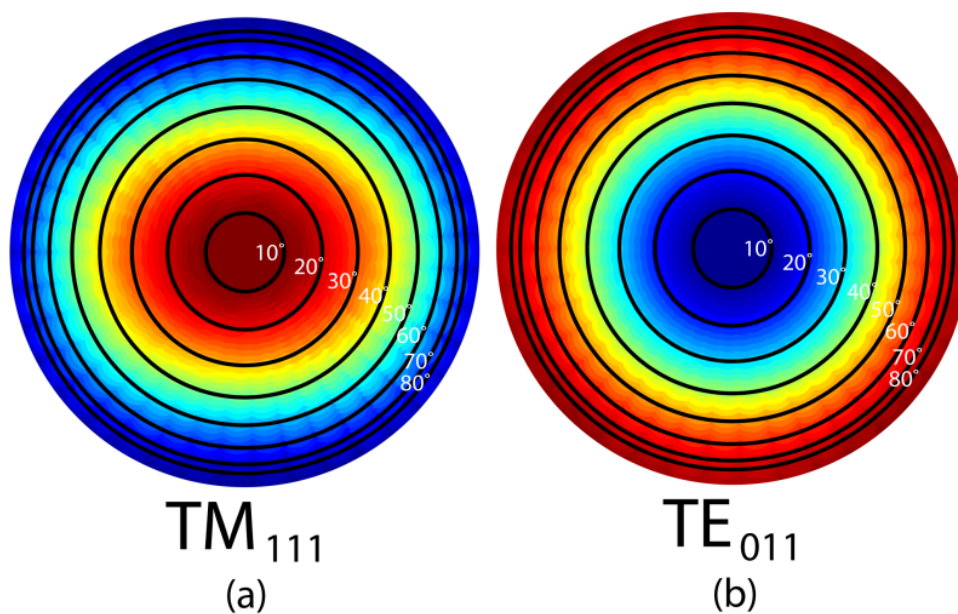
Figure 5.8. Far field radiation patterns calculated from FDTD simulations. The intensity of the radiation is normalized so that red (blue) indicates maximum (minimum) radiation intensity. The concentric black circles represent iso-angle contours of the radiation pattern in the top hemisphere of the nanopatch cavity. The TM_{111} mode (a) has surface normal radiation and the TE_{011} mode (b) has surface parallel radiation. Depending on application, one mode can be selected to either emit normally or couple into planar optical circuits.

Stratton-Chu formula without physical source currents or charge:

$$\vec{E}(\vec{r}) = \frac{1}{i\omega\epsilon_0}\nabla \times \left(\nabla \times \int_S G(\hat{n} \times \vec{H})ds\right) + \nabla \times \int_S G(\hat{n} \times \vec{E})ds$$

where $\vec{E}$ and $\vec{H}$ are evaluated on the surface of a closed box near the cavity and G is the Greens function for the homogeneous Helmholtz equation. The far field pattern was evaluated at a radius of 1.5 millimeters away from the cavity (Fig. 5.8). The TM_{111} mode is linearly polarized in the horizontal direction, consistent with a cylindrical mode with an azimuthal mode number $m = 1$. The TE_{011} mode is azimuthally polarized, as confirmed by experimental observation (see below).

5.2   Fabrication Procedure

Metallodielectric nanocavities present a unique fabrication challenge. At the nanoscale, surface recombination in semiconductors becomes a dominant recombination mechanism, reducing the efficiency of lasers. Furthermore, the integration of metal with semiconductor structures presents even more interesting challenges since the metal provides another path for carriers to recombine. Thus, these cavities must be properly engineered and made to reduce these deleterious effects and maximize the efficiency of any laser device.

Mindful of the effects of surface recombination on nanocavity laser performance, it is important to find material systems that have intrinsically low surface recombination velocities. Working in the near-infrared wavelength range, the obvious choice for such a material system is the $In_xGa_{1-x}As_yP_{1-y}$ quaternary material system with a surface recombination velocity of $v_s = 2 \times 10^4 \ cms^{-1}$ (roughly two orders of magnitude slower than GaAs systems)[83]. Finally, $In_xGa_{1-x}As_yP_{1-y}$ can have high energy barriers to confine carriers and prevent them from thermalizing into the metal layers surrounding the semiconductor.

The nanolasers were fabricated using a process that is intrinsically compatible with integration onto silicon substrates for applications in optical interconnect technology. In summary, oxide and metal are evaporated onto the epitaxial layer, the substrate is then flipped upside down and bonded to another carrier. Mechanical grinding and wet etching techniques are used to remove the backside, the sample is patterned using electron-beam lithography and liftoff, and finally etched using reactive ion etching (Fig. 5.9).

First, an epitaxial wafer was prepared with an n-InP substrate, a 50 nm $In_{0.53}Ga_{0.47}As$ etch stop layer (lattice matched), a 10 nm u-InP barrier layer, a 200 nm $In_{0.53}Ga_{0.47}As$ active layer, and a final 10 nm u-InP barrier layer grown by MOCVD techniques (Landmark Corporation). It is important to note that this wafer can easily be modified to incorporate electrical injection of carriers by properly doping the two 10 nm InP barrier layers.

Next, I cleaned the substrate with organic solvents, dipped it in 49% hydrofluoric acid for five seconds, and then rinsed it in water to remove the native oxide. Immediately after, the sample was placed into a load-lock to deposit 5 nm of titanium dioxide. The titanium dioxide serves as a dielectric (although it is a large-bandgap semiconductor) to prevent carriers from thermalizing into the metal layer (see Fig. 5.10). The titatium dioxide was deposited using atomic layer deposition (ALD) in a Picosun Sunale R150 reactor with titanium tetraisopropoxide and water precursors. The growth temperature for the oxide was 275°C. The thickness of this dielectric can have significant impacts on device performance.
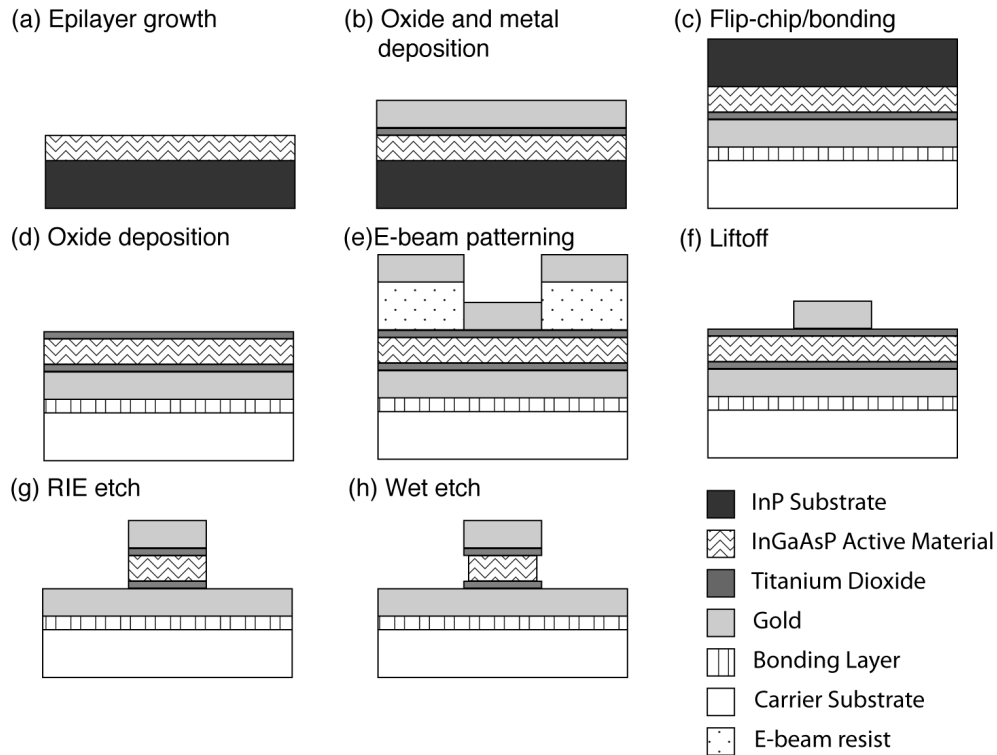
Figure 5.9. Side view of a typical fabrication flow for creating nanopatch cavity lasers.

If the oxide is too thick, the confinement factor of the eigenmode is reduced and more gain is required to initiate lasing. If the dielectric is too thin, then carriers can tunnel through the dielectric, degrading photoluminescence and the lasers efficiency. After careful study into optimum dielectric design, 5 nm of titanium oxide was chosen to maximize the mode confinement factor, although efficiency is reduced. I show the dependence of semiconductor photoluminescence on oxide thickness in Fig. 5.10.

After oxide deposition, I evaporated metal onto the substrate. Titanium (3 nm) followed by gold (80 nm) was deposited onto the semiconductor using electron beam lithography. The rates of evaporation were kept low (less than 1 Å/s) and the substrate was never allowed to heat up past 75°C. The chamber pressure was around 5×10^{-6} Torr during evaporation. The titanium layer serves as a very thin adhesion layer, and no measurable effects on nanolaser performance were detected from its use.

The substrate was then flipped and bonded to a carrier wafer. Initially, I cleaned a glass slide very carefully and placed a small drop of NOA-81 UV-curable epoxy onto the semiconductor substrate (on the metal side). The glass slide was placed on top of the substrate so that a thin layer of epoxy was sandwiched by the glass slide and semiconductor substrate. All air bubbles were removed from the interface. The sample was then placed under a UV light to cure.

Once the epoxy was cured, the chip was mounted on a manual lapping machine, and mechanically grinded on sandpaper until only 50 microns of the original substrate was left. Then
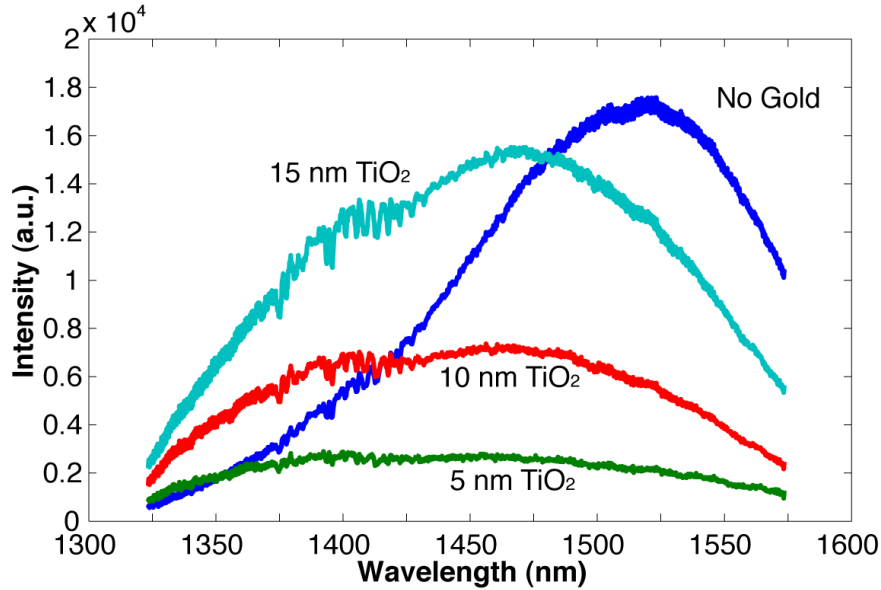
Figure 5.10. The dependence of photoluminescence (PL) from a 220 nm thick epitaxial layer of InGaAsP with varying thicknesses of titanium dioxide between semiconductor and gold. The data were taken after step (d) in the fabrication process shown in Fig. 5.9 at room temperature under pulsed (100 ns, 20 kHz repetition rate) and high-power pumping conditions. The reason for the anomalous PL present at 1400 nm was not studied, although FabryPerot resonances in the thin film structure that was probed could cause such enhancement. The PL degrades as the oxide thickness decreases, signifying that carriers are tunneling into the metal from the semiconductor. At 15 nm of TiO$_2$, the peak PL reaches nearly the same intensity as a semiconductor layer without any metal present.

the sample was cleaned with acetone and placed into a 1:1 HCl:H$_3$PO$_4$ acid solution at 50°C. The etching rate of this solution was approximately 5 microns per minute. After the entire substrate was removed, the sample was washed in deionized water and dried. The etch stop layer (made out of In$_{0.53}$Ga$_{0.47}$As) was subsequently removed using a 1:1:10 H$_2$SO$_4$:H$_2$O$_2$:H$_2$O etch for 3 seconds. The sample was the rinsed in water, and placed immediately into a load-lock chamber in preparation for deposition of another 5 nm of titanium dioxide. Finally, I deosited the TiO$_2$ at 150°C using the same procedure outlined above. Lower temperatures were used to deposit the second dielectric layer to prevent metal/semiconductor diffusion.

After oxide deposition, electron-beam sensitive resist was spun onto the substrate. Copolymer methyl methacrylate (MMA, 9% in ethyl lactate, Microchem Corp.) was spun onto the substrate at 5000 rpm for 1 minute. I then baked the sample at 180°C for 1.5 minutes. After cooling, polymethyl methacrylate (PMMA, 2% dissolved in anisole, Microchem Corp.) was spun onto the sample for 45 seconds at 2500 rpm. The sample was then baked again for 2 minutes at 150°C. This bilayer resist paradigm was used to make subsequent liftoff steps more robust. It is also important to note that this lithography step can be easily accomplished using conventional optical lithography since the features are larger than 200 nm in most cases.

Subsequently, I exposed he resistby electron-beam lithography (Crestec CABL-9510CC) with a 50 kV beam. The dose given to the resist was between 300-700 $\mu C/cm^2$. The optimal dose was identified to be around 450 $\mu C/cm^2$. After exposure, the sample was developed in 1:3 MIBK:IPA developer at room temperature for 1 minute. The sample was sonicated during the developing process for 5 seconds to improve the resulting exposed pattern. The sample was rinsed in IPA and dried using a nitrogen gun.
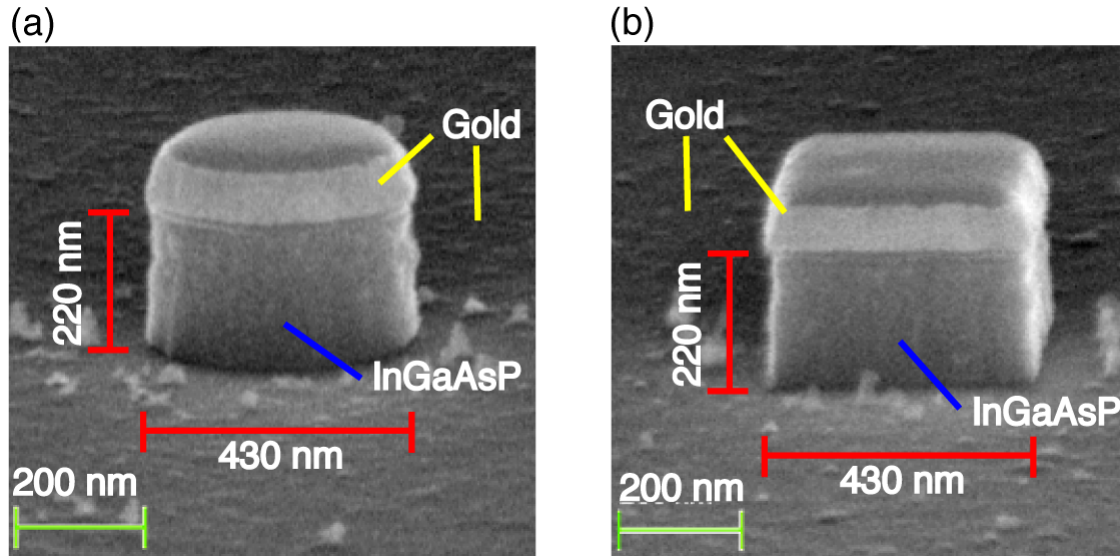
Figure 5.11. Scanning electron micrographs of fabricated nanopatch lasers after reactive ion etching. Perspective views (65° tilt) of cylindrical and rectangular nanopatches are seen in (a) and (b), respectively.

I transferred the electron beam pattern to the substrate using liftoff. Metal was evaporated on the substrate using electron-beam evaporation using the exact same technique as described above. I used titanium (3 nm) as an adhesion layer, followed by 80 nm of gold, followed by 20 nm of titanium again as a etch mask for subsequent etching steps. After metal evaporation, the sample was placed in acetone at room temperature for about 30 minutes to liftoff unpatterned metal. The sample was agitated at the end using sonication for roughly 5 seconds. The substrate was then rinsed with IPA and dried.

To etch the semiconductor, I used reactive ion etching for an anisotropic dry etch to define a single nanolaser device (with titanium/gold/titanium acting as a etching mask). The semiconductor was etched using hydrogen and methane gases. A custom-built plasma-thermal parallel plate plasma etcher (RIE) was first cleaned using oxygen plasma for 1 hour. Around 15% methane in hydrogen at roughly 35 milliTorr of etching pressure and a self-bias of 500 V resulted in an etch rate of roughly 20 nm/min with ~50mW/cm^2 of RF power. After dry etching the substrate, the sample was wet etched to remove the resulting damage associated with reactive ion etching. First, I placed the sample in 30% hydrogen peroxide and rinsed thoroughly in water. Then, I placed the sample in 49% hydrofluoric acid to remove the oxidized semiconductor. One such cycle removed roughly 10-15 nm of semiconductor from the sidewalls. This process was repeated three times to effectively clean the sidewalls of the devices [85].

5.3 Experimental Verification of Lasing

To reduce metal loss and non-radiative recombination and increase the semiconductor optical gain, we performed our laser characterization at low temperature (78K). The fabricated sample was mounted in a low temperature cryostat cooled by liquid nitrogen, and optically pumped from the top by a 1060 nm semiconductor diode laser with a 100 ns pulse width and a 5 kHz repetition rate (0.05% duty cycle) using a microscope objective with a 0.7 numerical aperture. The excitation pulse width of 100 ns was chosen to be much larger than the spontaneous emission and carrier lifetimes, which are on the order of one nanosecond, to obtain quasi-static equilibrium during the pumping time. Low duty cycle pulses are used to minimize possible thermal effects. However, thermal gradients in time most likely affected the emission characteristics of each lasing mode, broadening the measured linewidth from its actual value. This problem was exacerbated by inefficient pumping of the cavity from the top of the nanopatch cavity. The diameter of the focused pump beam is approximately 2 μm. The photoluminescence emission spectra at various optical excitation powers and positions were captured by the same objective used to pump the laser, and analyzed by an infrared spectrometer. The dependence of the spectrally-integrated laser power as a function of the excitation power was obtained from the spectra data. For polarization-resolved near-field radiation pattern measurements, a high-sensitivity InGaAs near-infrared camera was placed at the image plane of the objective, and a broadband linear polarizer in front of the camera selected a single polarization. A zero-order quarter-wave plate was also used to identify the polarization state of the near-field radiation.

Figure 5.12 shows the resonant wavelength evolution and lasing spectra of the cylindrical and rectangular nanopatch cavities with various radii and lengths, respectively. I clearly observed the cavity resonance dispersion of the two lowest order modes (Fig. 5.14a), and it agrees well with the analytic model (Eq. (5.1), (5.2), solid line) and numerical simulations based on finite-difference time-domain (FDTD, dashed line). The mode-dependent penetration depths were adjusted to obtain the best fit with the experimental observations ($\Delta_{TM_{111}} = 13\ nm$ and $\Delta_{TE_{011}} = 8\ nm$). According to our simulation results, the exact shape of sidewall also does not play a significant role in the mode frequency as the electromagnetic field is concentrated in the middle of the semiconductor structure.

We observed single-mode lasing with > 20 dB side-mode suppression for most cavity radii (Fig. 5.15). Small nanopatch cavities ($r < 215\ nm$) lase in the electric dipole mode, while larger cavities lase dominantly in the magnetic dipole mode. Cavities with intermediate sizes exhibit significant side mode emission because the gain spectrum overlaps with both modes ($r = 223$ nm in Fig. 5.14). Although higher order modes are also observed at energies greater than the magnetic dipole mode in large-diameter cavities, no laser action is seen because their quality factors are too low in accord with predictions from numerical simulations.

Polarization-resolved near-field imaging reveals that the electric dipole mode is linearly polarized with a surface-normal radiation pattern, whereas the magnetic dipole mode is azimuthally polarized and has a ring-shaped radiation pattern within the objectives numerical aperture (Fig. 5.17). In the far field regime, the electric dipole mode primarily radiates
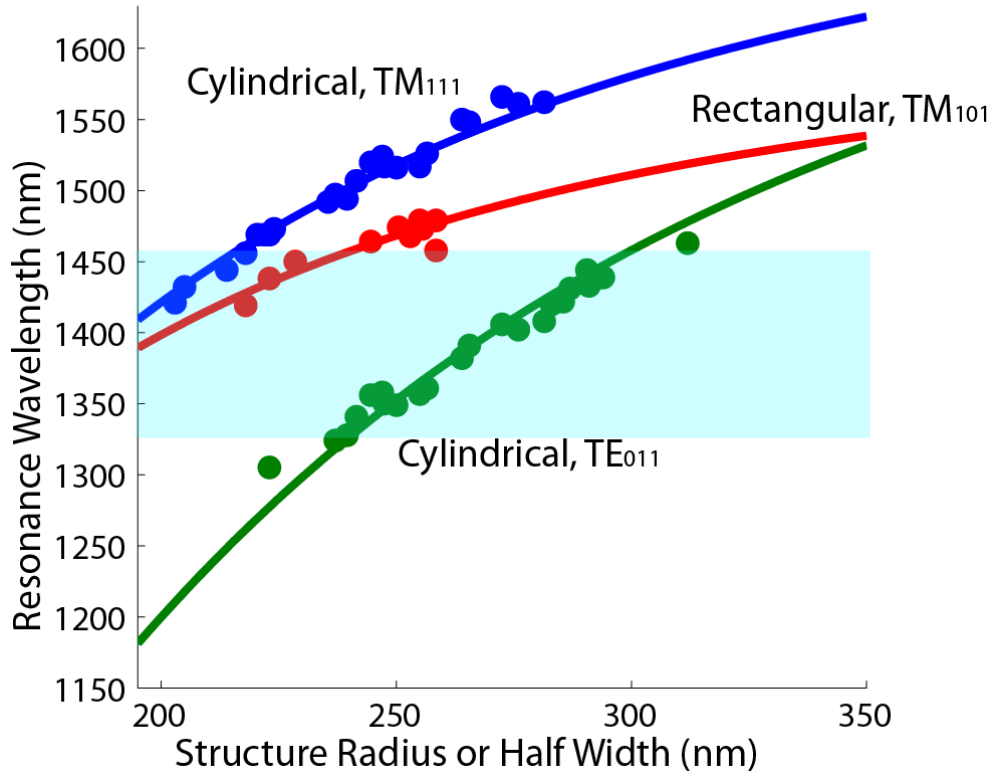
Figure 5.12. The dependence of cavity geometry on resonance wavelength is shown. For cylindrical (rectangular) cavities, the horizontal axis represents cavity radius (half-width). The blue shaded region indicates the gain bandwidth of the semiconductor where lasing is observed. Dots represent experimental data.

surface normal, and the magnetic dipole mode radiates in-plane with the device, making it more suitable for integration with planar lightwave circuit technologies.

The laser emission spectra were measured at various optical pumping levels for two representative circular nanopatch lasers which mainly support the electrical (TM$_{111}$, $r = 203$ nm) and magnetic (TE_{011}, $r = 265$ nm) dipole modes. Figures 5.15a and 5.15b show examples of such measurements. A small fraction of optical pumping energy from the surface normal direction is transferred to the gain medium mainly by scattering near the cavity structure. Since most of pumping energy is reflected by the patch and ground plane, it is difficult to accurately estimate the actual absorbed pump power at the gain material. We therefore use the total optical pump power incident on the sample in Figs. 5.15 and 5.18. We estimate that only a small fraction of pump power is coupled to the subwavelength-scale nanopatch resonator structure ($\lambda_{pump} = 1060$ nm), and the actual absorbed pump power is much lower. The optical pumping efficiency can be increased by making the cavity resonant with the pump light [21].

The cavity quality factors for the electric and magnetic dipole modes are experimentally estimated to be 132 and 168, respectively, from the emission spectra well below the laser
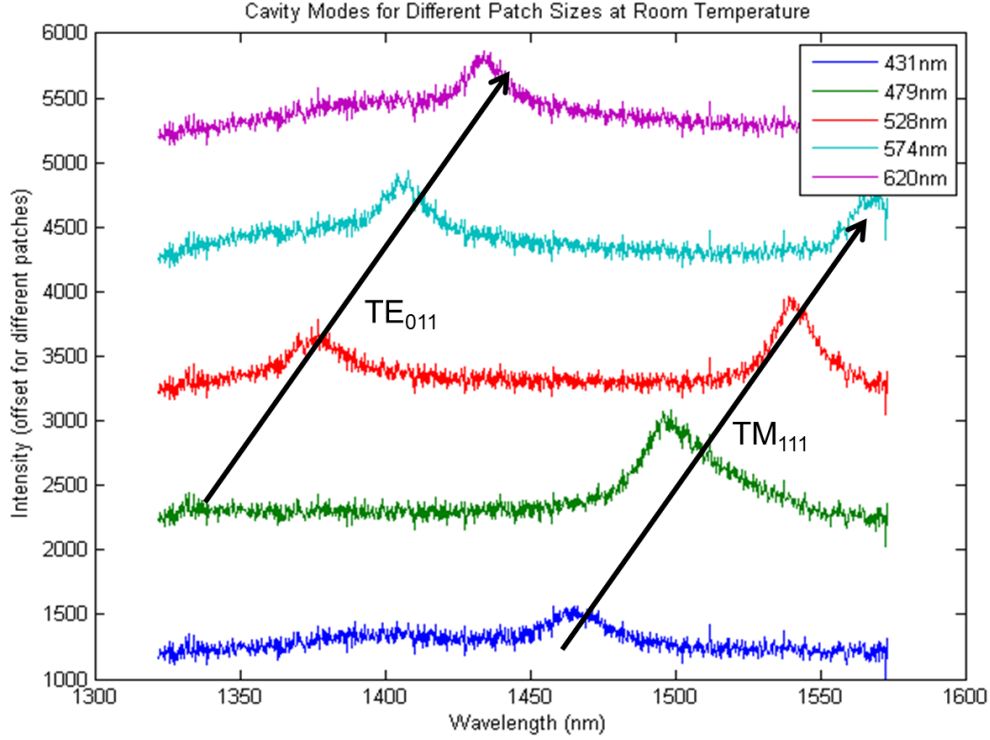
Figure 5.13. The photoluminescence spectra for nanopatches with various diameters obtained with continuous wave optical pumping at room temperature. Both the TM_{111} and TE_{011} modes are observed.
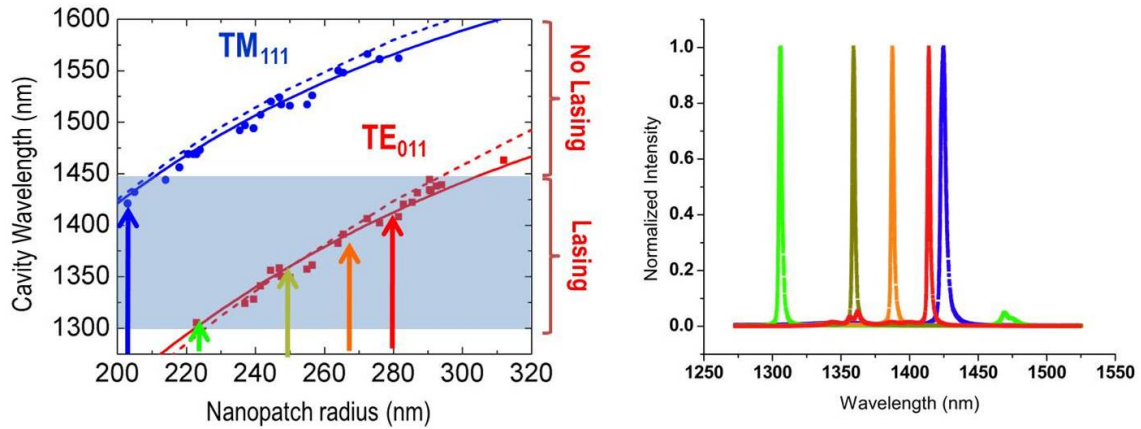
Figure 5.14. (a) Resonance wavelengths of cylindrical nanopatch cavities with different radii at 77 K. The points represent measurement results, the dashed lines represent numerical modeling, and the solid lines are the theoretical dispersion curves for electrical (TM_{111}, penetration depth $\Delta_{TM_{111}} = 13\ nm$, blue) and magnetic ($TE_{011}$, $\Delta_{TE_{011}} = 8\ nm$, red) dipole mode from the perfect conductor model. The colored region shows the gain spectra full width at half maximum. (b) Laser emission spectra for different radii nanopatch lasers. The colors correspond to the arrows in (a).

94
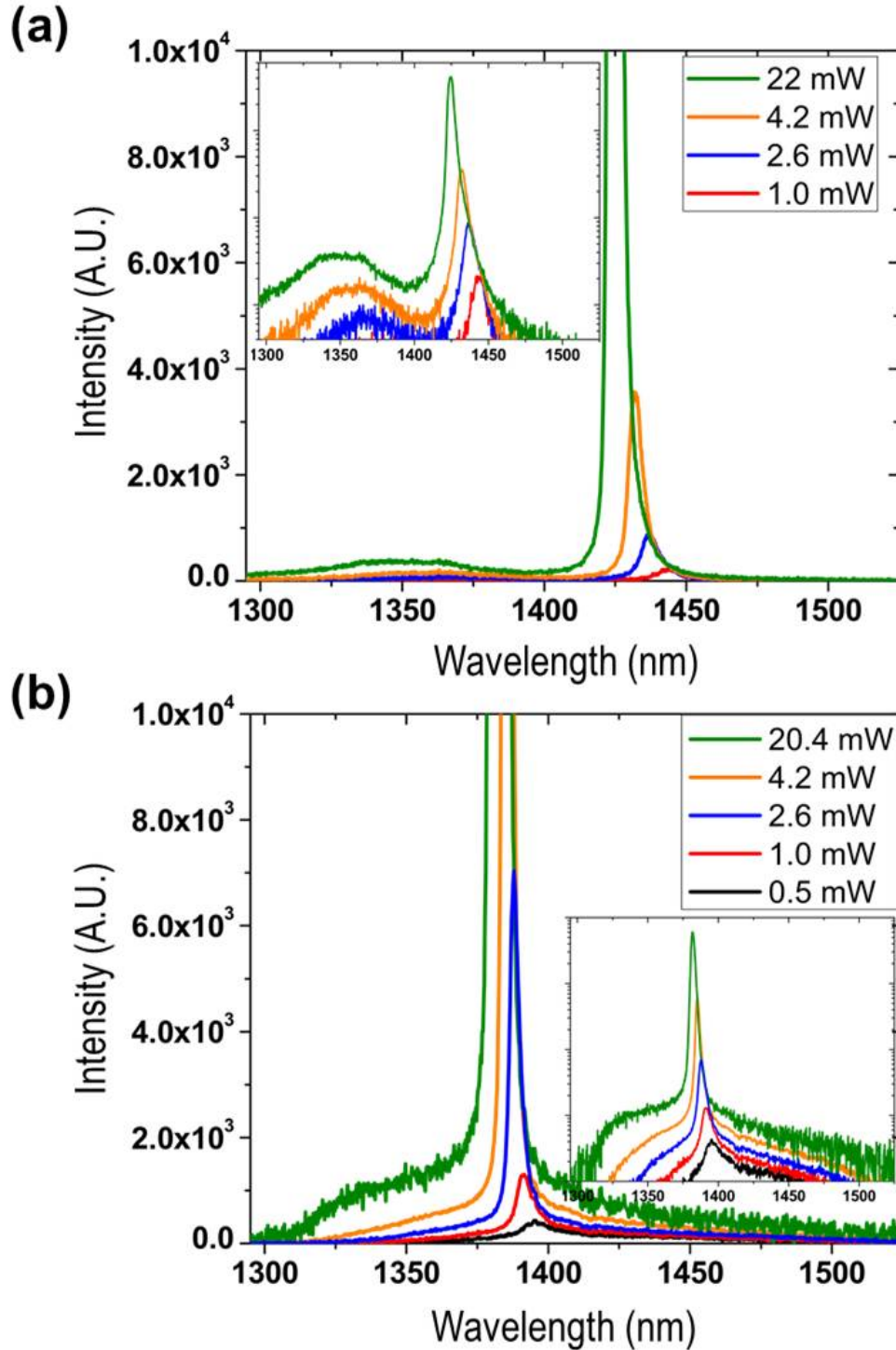
Figure 5.15. Evolution of the emission spectra with increasing peak pump power for nanopatch lasers with radius of (a) 203 and (b) 265 nm. The 203 nm nanopatch cavity lases in electric dipole mode while the 265 nm cavity lases in magnetic dipole mode.
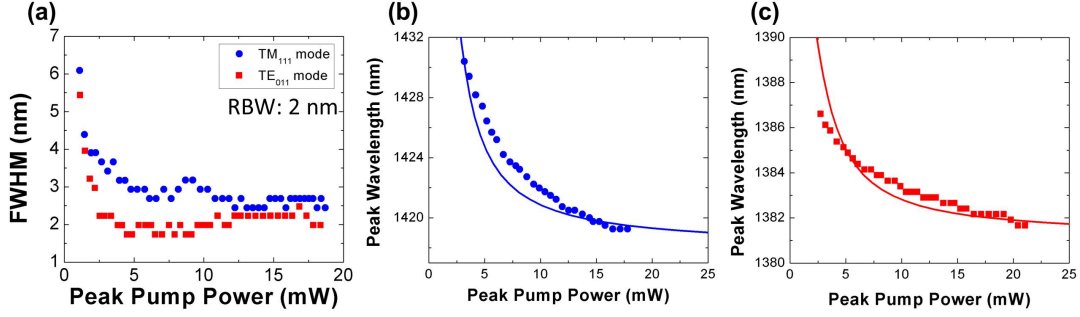
Figure 5.16. (a) The linewidth of both operating modes in the cylindrical nanopatch as a function of pumping power. (b,c) The wavelenth shift of the laser wavelength as a function of pump power for the TM_{111} (b) and TE_{111} (c) modes.
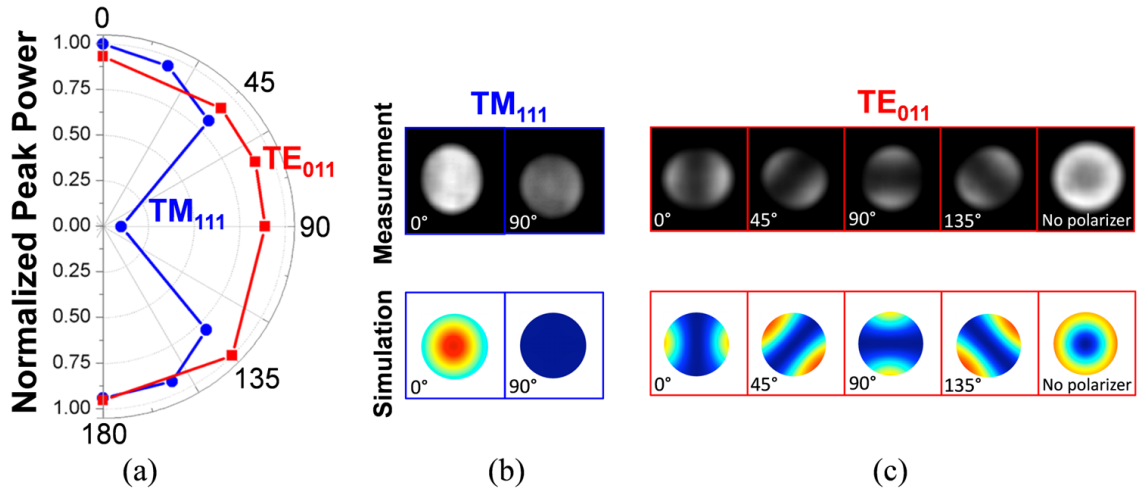
Figure 5.17. (a) Normalized peak power with respect to the linear polarization angle for the electrical (blue, circles) and magnetic (red, squares) dipole modes. The measured near-field radiation patterns with various polarization angles shown in (b) and (c) confirm that the first and second-order modes are linearly and azimuthally polarized, respectively (grayscale images in the upper row). They also agree well with the FDTD simulations (color images in the lower row).

threshold. FDTD numerical simulations based on room-temperature metal loss predict quality factors of 65 and 80, which is approximately half of the experimental values. We believe that this discrepancy can be explained by the reduction in resistive heating in the metal layers at low temperature [10]. The cavity quality factors measured at room temperature match well with simulation (Fig. 5.13).

With such small mode volumes, the spontaneous emission from the gain medium is usually modified through the Purcell effect. Our optical cavity linewidth is broader than the homogeneous linewidth of the bulk gain material at typical pump levels, which is about a few milli-electron-volt at low temperature. The Purcell factor for a particular polarization is given by $F = (2/\pi^2)Q/(V_{eff}/(\lambda/2n_{eff})^3)$. From the experimental quality factors (Q)
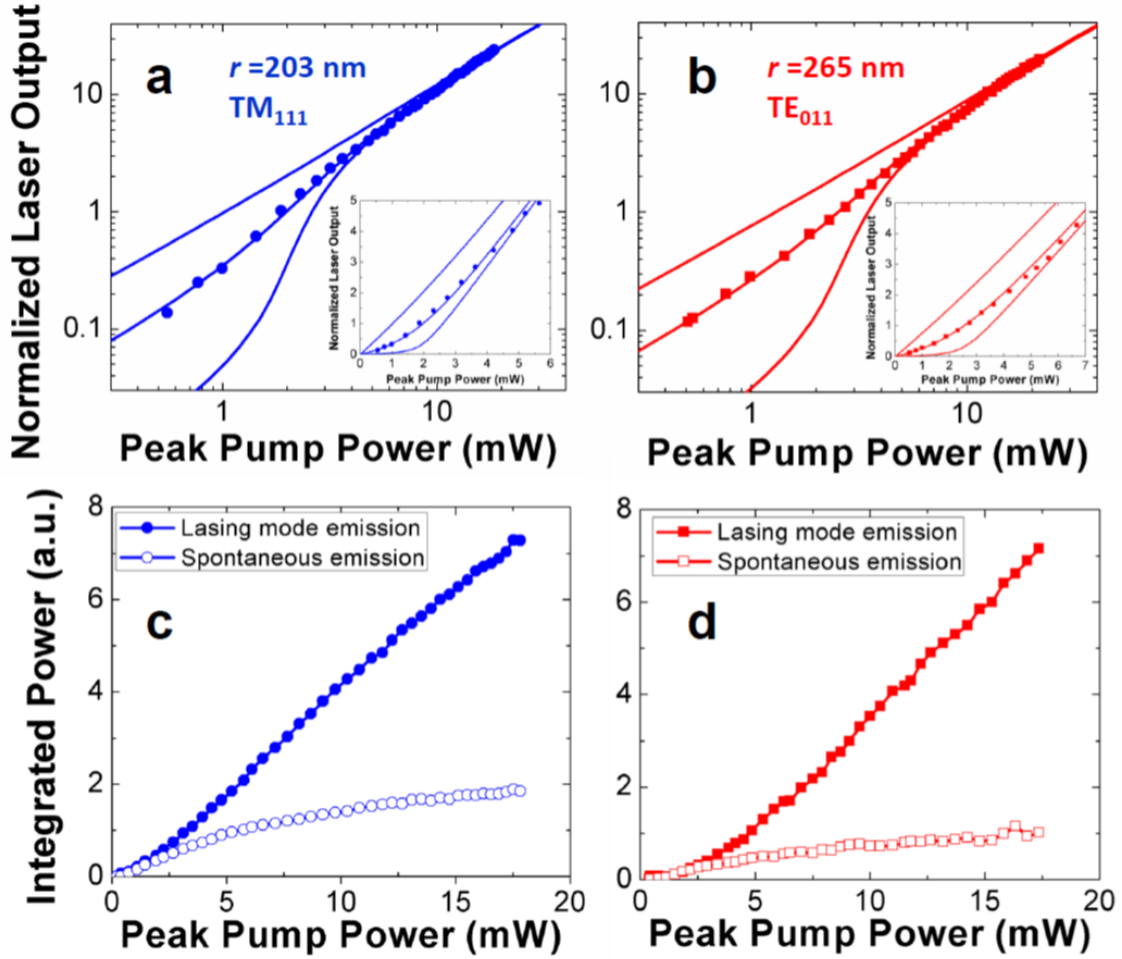
Figure 5.18. Output intensity characteristics of the nanopatch lasers. Output intensity-versus-pump characteristics of the semiconductor nanopatch lasers with radius of (a, c) 203 and (b, d) 265 nm. Stimulated and spontaneous emission components are separately shown in (c, d), while total output powers are plotted in (a, b). The solid lines in (a, b) are simulations obtained from the laser rate equation with the Purcell factor, F, and spontaneous emission coupling factor, β. Output intensity curves for $F\beta = 0.1$ and 10 are also shown for comparison. The insets in (a, b) show the linear-scale plots near the laser threshold. The vertical scales are normalized by the laser output powers at threshold pump levels predicted by the rate equation models. The parameters used for the electric and magnetic dipole modes are $F = 49.5$, $\beta = 0.022$ and $F = 11.4$, $\beta = 0.105$, respectively.

and calculated modal volumes $(V_{eff}/(\lambda/2n_{eff})^3)$, the Purcell factors for the electrical and magnetic dipole modes are calculated to be 49.5 ($_{TM} = 1420\ nm$) and 11.4 ($_{TE} = 1380\ nm$), respectively.

To evaluate the spontaneous emission coupling factor, β, of the nanopatch lasers with respect to their eigenmodes, the experimental luminescence data are compared with theoretical

curves obtained from the following rate equations:

$$\frac{dN}{dt} = P - g(N)S - \frac{1-\beta}{\tau_{sp}}N - \frac{F\beta}{\tau_{sp}}N - \frac{v_s S_a}{V_a}N \tag{5.3}$$

$$\frac{dS}{dt} = \Gamma g(N)S - \frac{S}{\tau_{ph}} + \frac{\Gamma F\beta}{\tau_{sp}}N \tag{5.4}$$

where again N and S are the carrier and photon densities, P is the pumping rate, N_0 is the transparent carrier density, and Γ is the optical confinement factor. S_a and V_a are the exposed surface area and volume of the gain region, respectively ($S_a = 2\pi r h$, $V_a = \pi r^2 h$). Steady-state solutions are used to obtain the fitting curves in Fig. 5.18. The spontaneous emission lifetime is assumed to be $\tau_{sp} = 1.5\ ns$, and the laser mode has faster spontaneous emission rate accelerated by the Purcell factor, F. We only considered surface recombination as a non-radiative recombination source because Auger recombination is negligible at low temperature. When assuming a surface recombination velocity of $v_s = 2 \times 10^4\ cm/s$, the non-radiative recombination lifetime is $\sim$one nanosecond with the given cavity radius ($r = 200 \sim 300$ nm). The photon lifetime is important in determining the laser threshold and is assumed to be proportional to the cavity quality factor ($\tau_{ph} = Q/(2\pi f)$, where Q and f are the cavity quality factor and resonance frequency, respectively). Since the carrier concentration, N, is not much larger than the transparent carrier density, N_0, we assumed a linear model for optical gain $g = cG(N - N_0)/n_g = 1.09 \times 10^{-5}(N - 4 \times 10^{17})\ s^{-1}$, where c, n_g, and G represent the light velocity in vacuum, the group refractive index of the cavity, and the linear differential gain coefficient, respectively.

The small effective mode volume and the good optical mode confinement in the gain material result in relatively large β and strong photon-cavity interactions. As a result, the integrated laser emission power behavior near threshold is very gradual, but the light output slope changes are still noticeable as shown in the insets of Fig. 5.18a and 5.18b. The theoretical fitting curves have the $F\beta$ product of 1.1 and 1.2 for the electrical and magnetic dipole modes, which corresponds to the β factors of 0.022 and 0.105, respectively. For comparison, light output curves with two extreme $F\beta$ product values (0.1 and 10) are also shown. The magnetic dipole mode is nondegenerate, and the spontaneous emission couples into a single optical mode, resulting in larger spontaneous emission coupling compared to the degenerate electric dipole mode [33]. The laser wavelength of the electric dipole mode is also detuned from the peak wavelength of the spontaneous emission ($\sim$1350 nm, shown in Fig. 5.15a, which limits the relative amount of spontaneous emission coupled to the cavity mode [33]. Figures 5.18c and 5.18d show that the stimulated emission increases rapidly over spontaneous emissions after threshold. Uncoupled spontaneous emission is softly clamped after threshold, confirming that $F\beta$ is large, and spontaneous emission plays an important role in these nanolasers, especially when the quality factor of the cavity is low [98].

The threshold optical gains for the electric and magnetic dipole modes are approximately 695 and 460 cm^{-1}, respectively, according to the rate equation model in Eq. (5.4). The optical gain coefficient at the laser threshold is inversely proportional to the optical confinement factor and the cavity quality factor, which can be improved by using silver [39, 99] and by optimizing the cavity design and mode profiles [100]. Our numerical simulations predict that the quality factors obtainable using silver nanopatch cavity structures at room temperature

are better than our experimentally estimated quality factors based on gold-based cavities operating at low temperature.

I also observed lasing action in rectangular nanopatches. Two non-degenerate modes with electric-dipole-like mode profiles can be seen if the cavity is anisotropic so that the length is different from the width of the cavity. These devices also have vertical radiation emission. As the anisotropy between the length and width is reduced, the orthogonal modes eventually become degenerate as seen in Fig. 5.19. Between the two modes, the higher energy mode always lases since higher gain can be achieved at higher energies due to a larger density of states. I plot the mode spacing versus anisotropy ratio in Fig. 5.19f. There is an overall red shift in cavity resonances only because the cavities probed had larger dimensions at lower anisotropy. The spectra recorded in Fig. 5.19 are slightly above lasing threshold so that both modes can be seen clearly. At larger pumping powers, the higher energy mode becomes the dominant mode, and spontaneous emission becomes clamped.
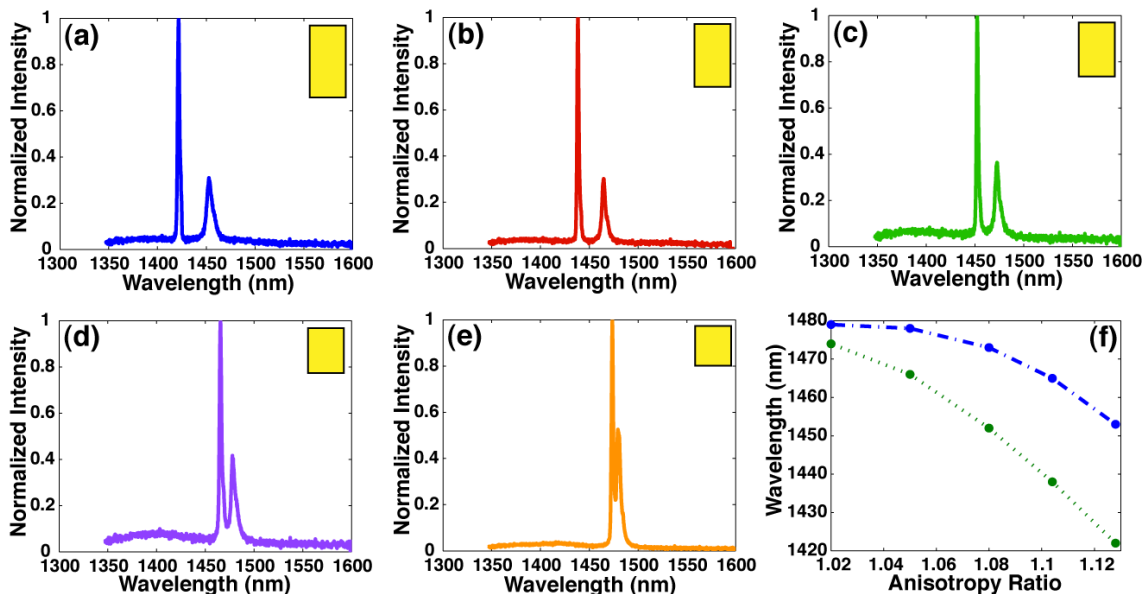
Figure 5.19. Nearly lasing spectra for rectangular patches with different anisotropy ratios are shown. The anisotropy ratio is reduced in order from (a) to (e). The yellow rectangles in the corner if each graph signify the top view of each rectangular nanopatch cavity, where the anisotropy has been exaggerated for clarity. The mode separation and wavelength versus anisotropy ratio is seen in (f).

To verify that the two rectangular cavity modes seen in Fig. 5.19 were electric-dipole-like, the polarization dependence of the two modes was studied. The two modes under study are the TM_{011} and the TM_{101} modes, which have orthogonal polarizations. They should also be linearly polarized, since the radiation can be thought of as coming from two electric dipoles in the metal layers of the cavity structure. In Fig. 5.20, I probed an anisotropic rectangular nanopatch with a linear polarizer below laser threshold. As the polarizer is rotated through 180 degrees, only one of the two modes is seen if the polarization is horizontal or vertical to the rectangle (Fig. 5.20a and 5.20c, respectively). At diagonal polarizations, both modes appear (Fig. 5.20b and refrectpold). Thus, each mode is strongly linearly polarized. Since

these modes are the fundamental moderate quality factor modes of rectangular cavities, they are useful for ultra-small laser designs. Unlike circular nanopatches, however, the polarization of the cavity can be controlled with great precision. Control over polarization in nanocavities can lead to many different applications including display technologies and quantum information processing [8].
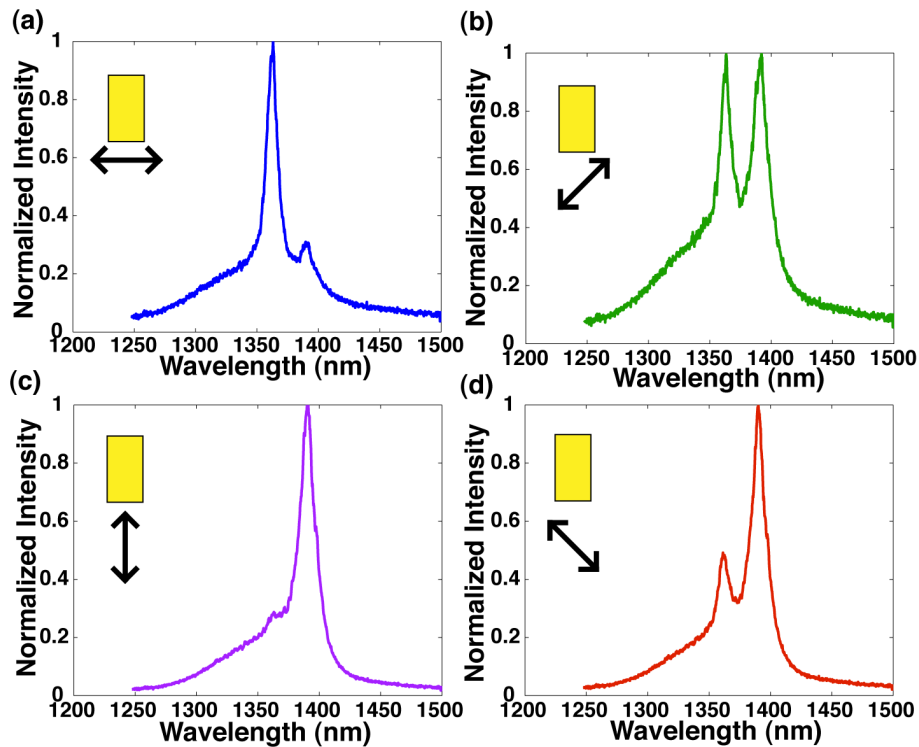
Figure 5.20. The two distinct resonances of an anisotropic rectangular cavity are shown below lasing threshold to have orthogonal polarization. The yellow square represents the geometry of the cavity in the x-y plane. The arrows represent the approximate polarization of the spectrum shown in each viewgraph, therefore graphs (b) and (d) have slightly different peak heights.

Plasmonic effects can be employed to further reduce the effective mode volume and the overall laser dimension especially in the visible wavelength range. However, since the quality factor of a metallic optical cavity is ultimately limited by the material properties of metal regardless of the cavity geometry [101], plasmon-photon mode hybridization or higher gain materials will be necessary to reduce cavity volumes further. Finally, electrically injected lasers based on ultra-thin epitaxial layers is possible with the use of properly engineering ultra-shallow-junctions using monolayer doping of III-V materials [102].

5.4 Towards Electrically-Driven Nanopatch Lasers

The demonstration of laser oscillations in a nanopatch cavity prooved that metal-optics based nanocavities could significantly reduce the total physical volume of lasers. To enable ubiquitous use of these devices, the devices will also need to be electrically driven.

In order to develop electrically driven nanopatch lasers, there are a few requirements to meet: 1) a P-i-N double heterostructure diode, 2) a scheme to contact the p- and n-regions, and 3) good ohmic contacts for each side.

In Fig. 5.21, I show the designed epitaxial layer to build a nanopatch laser with a total semiconductor thickness of 400 nm. The design is meant to target cavity eigenmodes that have an axial mode number of $p = 2$.
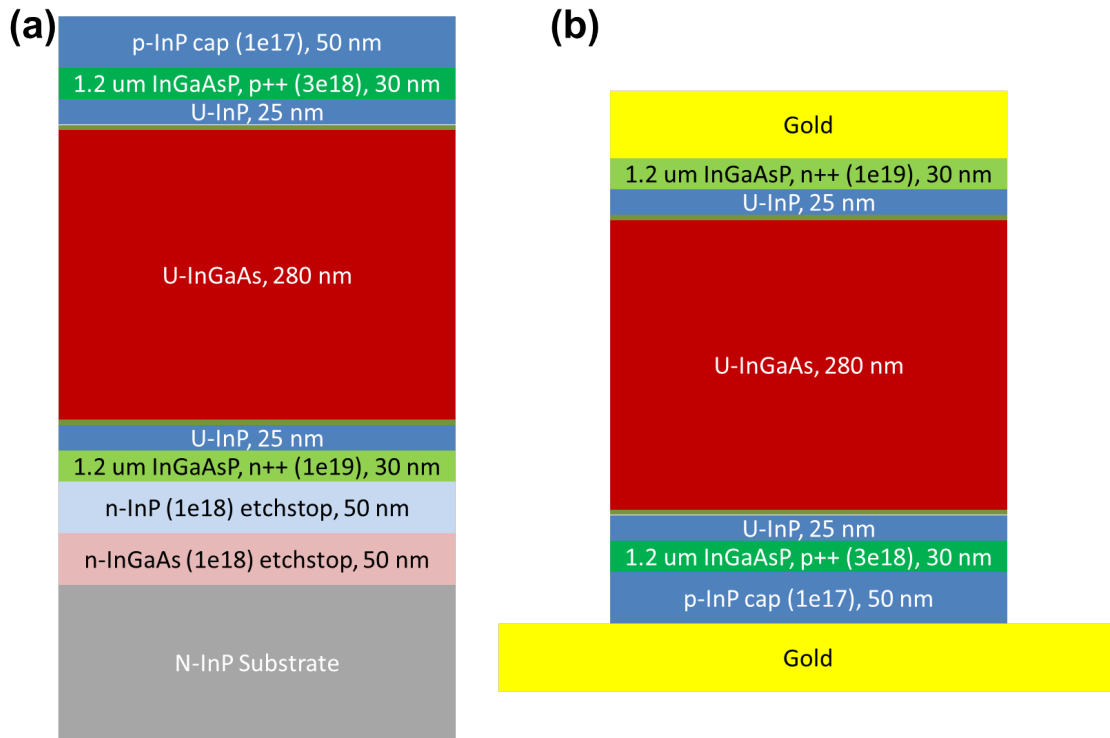
Figure 5.21. (a) The as-grown epitaxial layer design with a InP/InGaAs double heterostructure P-i-N diode. There are 30 nm InGaAsP ($\lambda_g = 1.2$ μm) contacts on each side to enhance the ohmic contact. The contacts are very heavily doped to facilitate low-resistance contacts. (b) The implementation of the grown epitaxial film into a nanopatch laser with a bottom gold ground plane and a top metal patch. The 30 nm contact region is heavily doped to facilitate low resistance ohmic contacts.

The bandstructure of the epilayer growth was also simulated using NextNano band structure simulation software. The software uses semiconductor parameters of all used materials and drift-diffusion equations to find a viable energy band diagram for the double heterostructure diode. In Fig. 5.22, I show the use of purely gold contacts and 30 nm 1.2μm-InGaAsP to contact the InP/InGaAs double heterostructure nanopatch diode. A 30 nm thick semi-

conductor contact layer is necessary to ensure that the contact layers do not become fully depleted do to the differences the work functions of gold and InGaAsP. Fully depleted contact regions would reduce the total built-in voltage of the diode and make it look like a resistor instead of a diode.
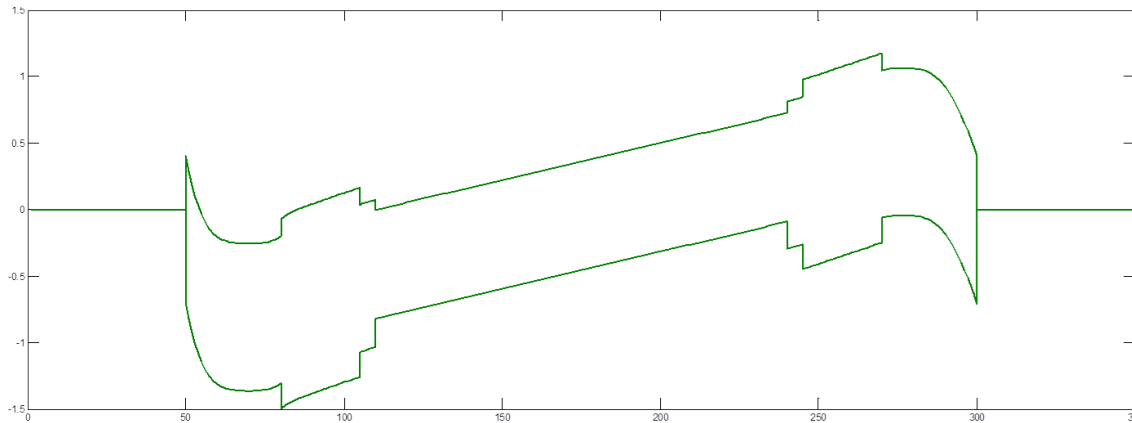
Figure 5.22. The simulated bandstructure of the epitaxial layer shown in Fig. 5.21b. The total thickness of the semiconductor region is 400 nm, gold contacts are used on both sides, and the metal contacting InGaAsP semiconductor regions are heavily doped at 30 nm thick.

After designing the epitaxial layer necessary to inject carriers into the InGaAs active region of the nanopatch cavity, we need to contact both the bottom ground plane metal and the top nanopatch metal without greatly disturbing the optical cavity design. In Fig. 5.23, I show such a contacting scheme. The gold via is used to inject electrons into the top metal nanopatch. The semiconductor underneath the gold via is etched away via wet etching to leave a suspended gold wire.

To be completely sure that the gold wire does not adversely affect the optical cavity's quality factor, I performed FDTD simulations of the entire device geometry. In Fig. 5.24, I summarize and verify that the gold via is minimally perturbing for the cavity. The gold wire is 1.5 μm long with a 80×80 nm cross-section. The nanopatch is 220 nm thick to target optical modes with axial mode number $p = 1$. Simulations with semiconductor thicknesses of 400 nm verify minimal coupling to optical modes with $p = 2$ as well. To judge the effect of the gold wire on the optical cavity, we focus on the quality factor of the TM_{111} mode with and without the wire. In a free standing stucture, $Q_{tot} = 65$ and $Q_{rad} = 1600$. With a gold via, $W_{tot} = 60$, while $Q_{rad} = 430$. Although there is leakage of the optical cavity into the metal via, the total optical quality factor changes by only 10%. Such a change in quality factor is minimal to the end result of having successful laser oscillations.

The development of ohmic contacts for the nanolaser is crucial to successful and efficient operation. Yet, since titanium use is limited in our cavity (to limit electromagnetic optical loss), low resistance contacts are made solely by heavily doping the metal-contacting semiconductor material. In the future, optical cavities that can allow titanium use or alloyed AuGe, AnZn, or AuBe contacts will alleviate this problem of high contact resistance.
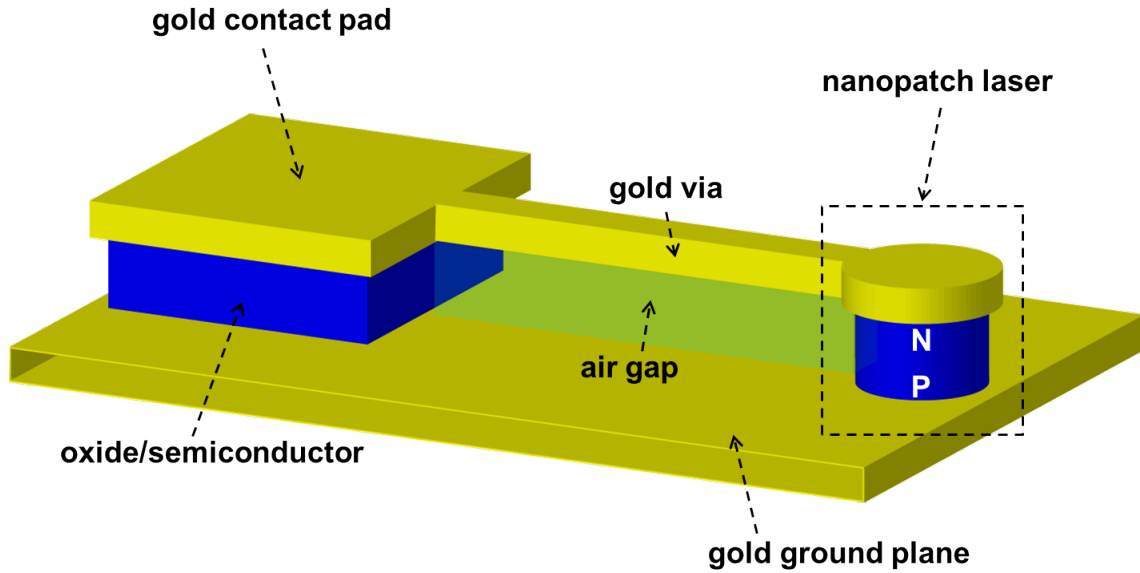
Figure 5.23. A schematic of a electrically contacted nanopatch laser diode. The gold via serves as the n-contact, and the p-contact is just the gold ground plane. The air gap is introduced simply by undercutting the wire area via wet etching.
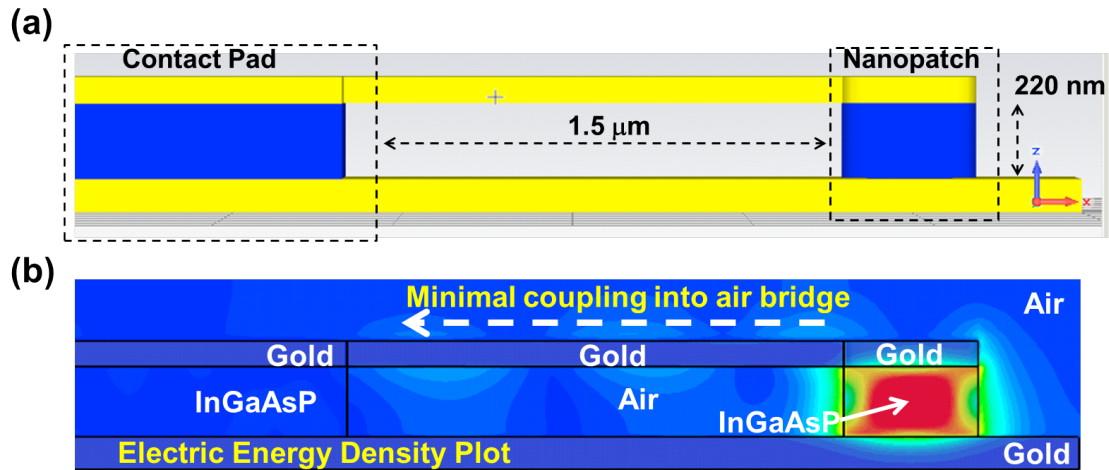
Figure 5.24. (a) A simulation schematic of a nanopatch cavity with a gold wire with 80×80 *nm* cross-section connected from a contact pad to the laser cavity. The wire is 1.5 μm long, and the semiconductor thickness is 220 *nm*. (b) A dB-scale plot of the electrical energy density of the TM_{111} mode of the nanopatch cavity. There is minimal coupling between the optical mode and the gold wire.

To fabricate the electrically driven nanopatch laser, the process flow was changed incrementally from the baseline optically-pumped device process. To bond the epitaxial layer to a carrier substrate (silicon in this case), I used benzocyclobutene (BCB). To use BCB bonding, first the silicon carrier is cleaned, and adhesion promoter AP-3000 is spun on. On top of the adhesion promoter, 1 μm of BCB is applied. On the III-V chip, AP-3000 is

spun onto a titanium layer evaporated after the gold ground plane. The two chips are then bonded in a nitrogen oven following the recipes from [103]. After removing the substrate, I deposited a 20 nm Al_2O_3 oxide layer via ALD. Then, I patterned alignment marks via optical lithography, patterned the nanopatch lasers with vias via electron beam lithography, and finally patterned the top metal contacts via optical lithography. The large metal contact pads were used to wirebond 50 μm gold wire to a leadless ceramic carrier chip. In Fig. 5.25, I present a summary of the fabrication flow. To allow the best ohmic contacts possible, I deoxidized the metal-contacting semiconductor material before evaporating metal on the semiconductor with a solution of 1:10 $HCl:H_2O$ for 30 seconds followed by a 1 minute water rinse. Finally, to remove dry-etch induced damage from the semiconductor sidewalls and undercut the gold via, I employed a 1:1 solution of hydrogen peroxide to a solution of 1:1 wt% citric acid monohydrate and water. The etch rate for the citric acid solution is roughly 1 nm/sec.
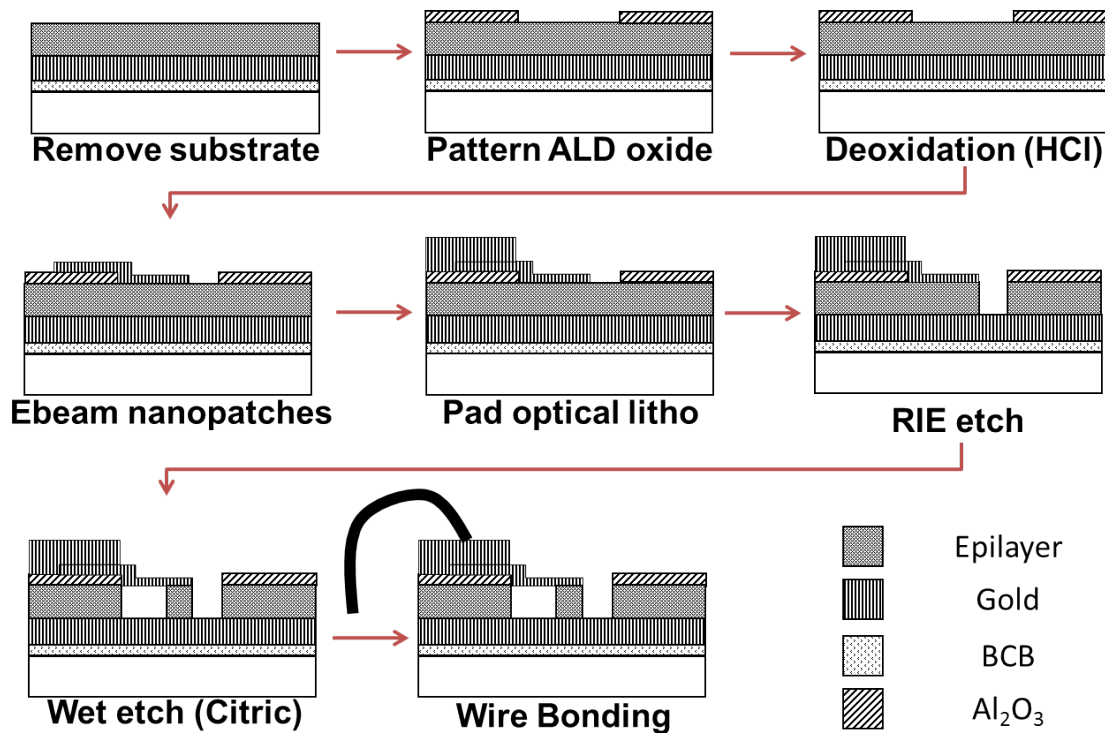
Figure 5.25. The fabrication flow for an electrically injected nanopatch laser. Up to the substrate removal step, the optical and electrical fabrication flows are similar. The top-side patterning is accomplished by optical and electron-beam lithography coupled with electron-beam evaporation of metal to define the top nanopatch and via as well as the wirebonding pads.

The final completed devices are shown in Fig. 5.26. In this particular iteration, the nanopatch laser was patterned after the wirebonding pads were evaporated.

To characterize the electrically driven nanopatch devices, the devices were first tested via optical pumping to verify that the optical cavity was not destroyed by the introduction of the gold wire. In Fig. 5.27, we summarize the results of the optical pump verification.
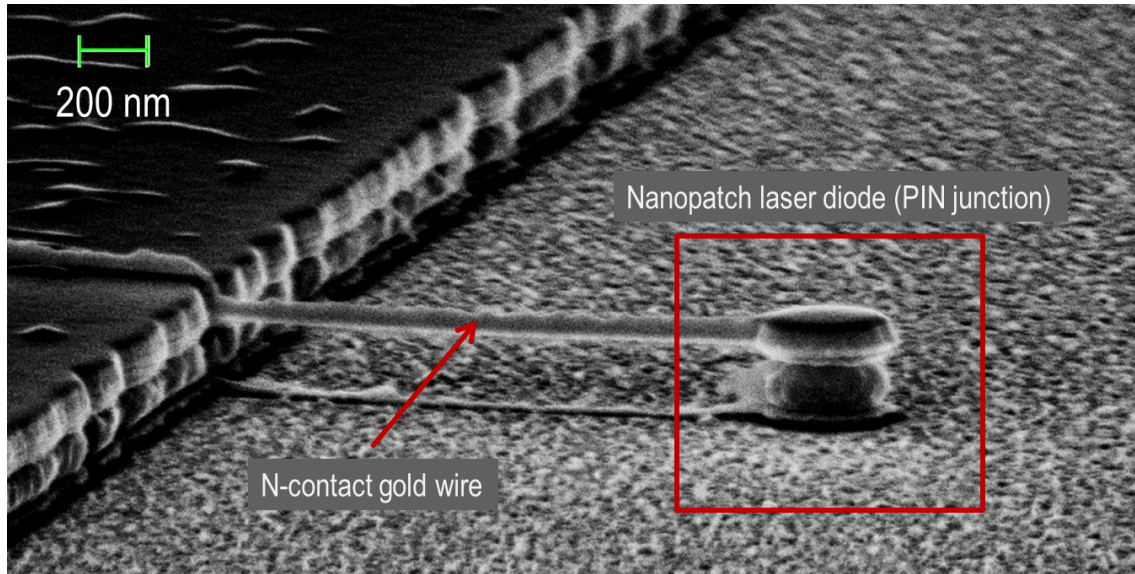
Figure 5.26. A scanning electron micrograph of a completed electrically driven nanopatch laser diode. The radius of the nanopatch is $r = 220\ nm$.

A nanopatch laser with radius $r = 230\ nm$ is connected to a 10 μm probe contact pad. The device was cooled to 77K and pumped with a pulsed laser ($\lambda_{pump} = 1064\ nm$, 50 ns pulses, 1% duty cycle, variable power). In Fig. 5.27a, I show a PL intensity map of the one nanopatch device connected to a metal probe contact pad. Spontaneous emission is observed from all around the pad area. Lasing is observed when the nanopatch laser itself is pumped. The conclusion, therefore, is that the gold wire does not perturb the optical cavity sufficiently to prevent lasing.
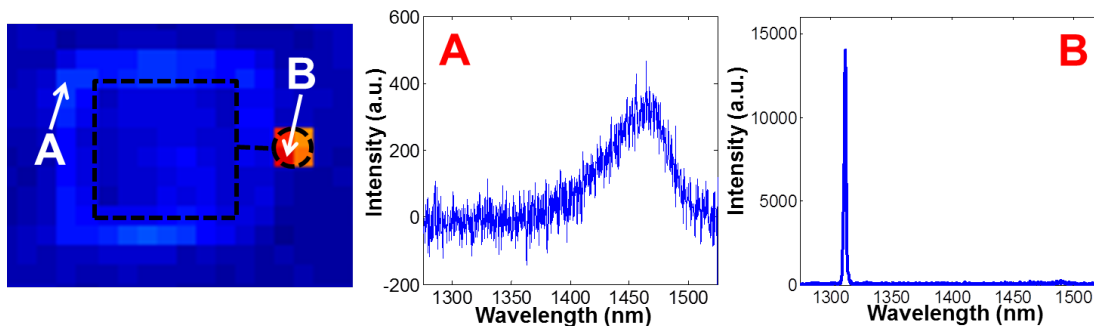
Figure 5.27. A PL intensity map for one nanopatch device connected to a metal probe pad. Spontaneous emission is observed when a $\sim 2\ \mu$m laser spot pumps the contact pad area (A). Laser oscillations are observed when the laser locally pumps the nanopatch device (B).

In order to characterize the electrically pumped photoluminescence of the devices, a pulsed current source was used with pulse widths of 100 ns and 1% duty cycle. Such short pulses, however, were probably mostly reflected due to the lack of proper microwave

frequency design to properly impedance match all of the circuit elements. In Fig. 5.28, we show the results of the electrically driven nanopatch diode. No laser oscillations are seen, although spontaneous emission is observed from the nanopatch cavity. A large change in the spontaneous emission characteristics at low and high temperatures (Fig. 5.28) show that spontaneous emission is amplified by the cavity at low temperatures, but no laser oscillations are seen. At higher temperatures, the spontaneous emission redshifts and total gain of the semiconductor is reduced via resistive heating.
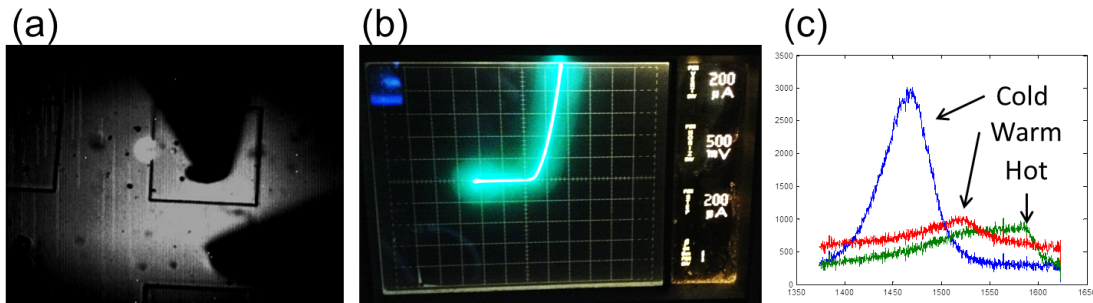
Figure 5.28. (a) A infrarad CCD image of spontaneous emission from a nanopatch cavity via electroluminescence. (b) The I-V diode characteristics of a nanopatch diode under quasi-continuous current injection (via an analog curve tracer with 60 Hz refresh rate). (c) The spontaneous emission seen from a nanopatch diode at 77K. As more current is introduced into the diode, the device warms up via resistance heating, and the PL redshifts and drops in magnitude.

Even under pulsed electrical operation, the nanopatch laser diode dissipates too much heat to reach lasing conditions. Yet, because the optical cavity has been shown to exist even with a gold wire perturbation, laser operation is achievable. In the future, further engineering of the ohmic contacts may be enough to induce lasing in the nanopatch cavity. Otherwise, higher quality factor cavities, such as those seen in Chapter 3, may be the ultimate solution to implement metal-optics nanolaser cavities.

Chapter 6

Conclusion

In this dissertation, I first began by exploring various materials and their electromagnetic interactions that allow nanolaser technology to exist. Then, I outlined some basic design criteria for these devices. I found the design is heavily dependent on the performance of metals and gain materials. From a systems-level point of view, I also found that nanolasers necessarily had to be small in order to be useful in ultra-low power on-chip optical interconnect technology.

The nanoarch optical resonator was then shown to be a viable plasmon-based nanocavity with extremeley small subwavelength electromagnetic and physical volumes. Unfortunately, the amount of ohmic loss in the metal precluded its use for nanolaser technology with III-V semiconductor materials. By relaxing the size constraints, a metal-optics-based waveguide-coupled nanocavity showed considerable promise for future integrated photonics. With nanocavities that reached quality factors of 1000, metal-optics allowed us to reduce the footprint of active photonics and still maintain hope for room-temperature electrically driven-operation.

Although the nanoarch resonator is currently too lossy with current metals, I demonstrated the plasmonic crystal defect nanolaser that confined surface plasmons to a very small area. With a demonstration of a coherent light source, plasmonic crystal technology has the potential to become a platform for integrated nanophotonics. Such integrated circuits could be able to sense minute chemicals using Surface-Enhanced Raman Spectroscopy (SERS), provide nonlinear all-optical switching, etc. much more efficiently than traditional PICs. Yet, challenges still remain in developing plasmonic circuits. Like all metal-based optics, metal loss must be mitigated. New research with low-loss metals and high-gain materials is now needed to enable this (and much other) technology in photonics. Yet, integrated plasmonics may yet be worth the price.

Finally, I have fabricated and characterized subwavelength-scale nanopatch semiconductor lasers at near infrared wavelengths. Utilizing pure metal-optics, both the effective mode volume and physical size of the nanopatch lasers are kept at subwavelength-scales because of

tight optical confinement from metallodielectric resonators. Although compact optical mode volumes are important for obtaining strong light-matter interactions, practically useful laser structures must be physically compact and lend themselves easily to integration with VLSI technology. Small laser volumes are a necessary aspect of any solution to the pressing challenge of solving the "tyranny of interconnects." Contrary to common belief, the presence of metal can improve the quality factor of subwavelength optical resonators by suppressing radiation into free-space. I believe that the nanopatch semiconductor laser can be a strong contender for the integration of optical components with nanoscale electronic devices because they are compact, they are based inherently on waferbonding techniques, and they use conductive metal structures for light confinement and electrical carrier injection in an ultra-small footprint.

For all of the progess that has been made, nanolaser design is still in its infancy. On the ond hand, progress has been, and will assuredly be, made in standardizing the way that devices can integrate onto a single, unified platform. The true questions in the field ultimately boil down to whether or not a practical nanolaser can be built that operates at room temperature and is electrically driven. To answer these questions, nanolaser engineers will have to better understand the devices at the material level. Can we produce low-loss metals using new nanomaterials such as carbon nanotubes? How can we utilize high-gain semiconductors that maintain inversion for long periods of time? I am sure that we will have encouraging answers in the very near future.

Bibliography

[1] J. Bardeen, "Three-Electrode circuit element," (1950). U.S. Classification: 330/250.

[2] M. Planck, "On the theory of the energy distribution law of the normal spectrum," Verh. Deut. Phys. Ges **2**, 237245 (1900).

[3] A. Einstein, "On a heuristic point of view about the creation and conversion of light," Annalen der Physik **17**, 132148 (1905).

[4] G. F. Amelio, "Experimental verification of the charge coupled device concept," **49**, 593–600 (1970).

[5] R. S. Ohl and R. S. Ohl, "Light-Sensitive electric device," (1946). U.S. Classification: 136/261.

[6] G. G. Stokes, "On the change of refrangibility of light," Philosophical Transactions of the Royal Society of London **142**, 463562 (1852).

[7] S. C. Raman, *Molecular diffraction of light* (University of Calcutta, 1922).

[8] C. H. Bennett, G. Brassard *et al.*, "Quantum cryptography: Public key distribution and coin tossing," in "Proceedings of IEEE International Conference on Computers, Systems and Signal Processing," , vol. 175 (1984), vol. 175.

[9] R. P. Feynman, "Simulating physics with computers," International journal of theoretical physics **21**, 467488 (1982).

[10] P. A. Franken, A. E. Hill, C. W. Peters, and G. Weinreich, "Generation of optical harmonics," Physical Review Letters **7**, 118119 (1961).

[11] P. Lebedev, "Untersuchungen ber die druckkrfte des lichtes," Annalen der Physik **311**, 433458 (1901).

[12] S. E. Miller, "Improved relations describing directional control in electromagnetic wave guidance," Bell Syst. Tech. J **48**, 21612188 (1969).

[13] Infinera, "Photonic integrated circtuis: A technology and application primer," .

[14] G. E. Moore *et al.*, "Cramming more components onto integrated circuits," Proceedings of the IEEE **86**, 8285 (1998).

[15] D. Miller, "Device requirements for optical interconnects to silicon chips," Proceedings of the IEEE **97**, 1166–1185 (2009).

[16] T. H. Maiman, "Stimulated optical radiation in ruby," Nature **187**, 493–494 (1960).

[17] Z. I. Alferov, "Nobel lecture: The double heterostructure concept and its applications in physics, electronics, and technology," Reviews of Modern Physics **73**, 767 (2001).

[18] F. J. Garcia-Vidal and E. Moreno, "Applied physics: Lasers go nano," Nature **461**, 604–605 (2009).

[19] M. Nomura, N. Kumagai, S. Iwamoto, Y. Ota, and Y. Arakawa, "Laser oscillation in a strongly coupled single-quantum-dot-nanocavity system," Nat Phys **6**, 279–283 (2010).

[20] J. P. Reithmaier, G. Sk, A. Lffler, C. Hofmann, S. Kuhn, S. Reitzenstein, L. V. Keldysh, V. D. Kulakovskii, T. L. Reinecke, and A. Forchel, "Strong coupling in a single quantum dotsemiconductor microcavity system," Nature **432**, 197–200 (2004).

[21] J. M. Gerard, B. Sermage, B. Gayral, B. Legrand, E. Costard, and V. Thierry-Mieg, "Enhanced spontaneous emission by quantum boxes in a monolithic optical microcavity," Physical Review Letters **81**, 1110 (1998).

[22] Y. Nakayama, P. J. Pauzauskie, A. Radenovic, R. M. Onorato, R. J. Saykally, J. Liphardt, and P. Yang, "Tunable nanowire nonlinear optical probe," Nature **447**, 1098–1101 (2007).

[23] S. A. Asher, V. L. Alexeev, A. V. Goponenko, A. C. Sharma, I. K. Lednev, C. S. Wilcox, and D. N. Finegold, "Photonic crystal carbohydrate sensors: low ionic strength sugar sensing," Journal of the American Chemical Society **125**, 3322–3329 (2003).

[24] M. Loncar, A. Scherer, and Y. Qiu, "Photonic crystal laser sources for chemical detection," Applied Physics Letters **82**, 4648 (2003).

[25] P. Alivisatos, "The use of nanocrystals in biological detection," Nature Biotechnology **22**, 47–52 (2003).

[26] R. W. Boyd and J. E. Heebner, "Sensitive disk resonator photonic biosensor," Applied Optics **40**, 5742–5747 (2001).

[27] W. A. Challener, C. Peng, A. V. Itagi, D. Karns, W. Peng, Y. Peng, X. M. Yang, X. Zhu, N. J. Gokemeijer, Y. T. Hsia *et al.*, "Heat-assisted magnetic recording by a near-field transducer with efficient optical energy transfer," Nat Photon **3**, 220224 (2009).

[28] J. D. Meindl, "Interconnect opportunities for gigascale integration," .

[29] E. K. Lau, A. Lakhani, R. S. Tucker, and M. C. Wu, "Enhanced modulation bandwidth of nanocavity light emitting devices," Optics Express **17**, 7790–7799 (2009).

[30] K. Iga, F. Koyama, and S. Kinoshita, "Surface emitting semiconductor lasers," IEEE Journal of Quantum Electronics **24**, 18451855 (1988).

[31] J. L. Jewell, J. P. Harbison, A. Scherer, Y. H. Lee, and L. T. Florez, "Vertical-cavity surface-emitting lasers: design, growth, fabrication, characterization," IEEE Journal of Quantum Electronics **27**, 13321346 (1991).

[32] S. L. McCall, A. F. J. Levi, R. E. Slusher, S. J. Pearton, and R. A. Logan, "Whispering-gallery mode microdisk lasers," Applied Physics Letters **60**, 289 (1992).

[33] T. Baba and D. Sano, "Low-threshold lasing and purcell effect in microdisk lasers at room temperature," IEEE Journal of Selected Topics in Quantum Electronics **9**, 1340–1346 (2003).

[34] O. Painter, R. K. Lee, A. Scherer, A. Yariv, J. D. O'Brien, P. D. Dapkus, and I. Kim, "Two-Dimensional photonic Band-Gap defect mode laser," Science **284**, 1819–1821 (1999).

[35] M. Nomura, S. Iwamoto, K. Watanabe, N. Kumagai, Y. Nakata, S. Ishida, and Y. Arakawa, "Room temperature continuous-wave lasing in photonic crystal nanocavity," Optics Express **14**, 6308–6315 (2006).

[36] H. Park, S. Kim, S. Kwon, Y. Ju, J. Yang, J. Baek, S. Kim, and Y. Lee, "Electrically driven Single-Cell photonic crystal laser," Science **305**, 1444–1447 (2004).

[37] B. Ellis, T. Sarmiento, M. Mayer, B. Zhang, J. Harris, E. Haller, and J. Vuckovic, "Electrically pumped photonic crystal nanocavity light sources using a laterally doped p-i-n junction," Applied Physics Letters **96**, 181,103–181,103–3 (2010).

[38] M. T. Hill, Y. Oei, B. Smalbrugge, Y. Zhu, T. de Vries, P. J. van Veldhoven, F. W. M. van Otten, T. J. Eijkemans, J. P. Turkiewicz, H. de Waardt, E. J. Geluk, S. Kwon, Y. Lee, R. Notzel, and M. K. Smit, "Lasing in metallic-coated nanocavities," Nat Photon **1**, 589–594 (2007).

[39] M. T. Hill, M. Marell, E. S. P. Leong, B. Smalbrugge, Y. Zhu, M. Sun, P. J. van Veldhoven, E. J. Geluk, F. Karouta, Y. Oei, R. Notzel, C. Ning, and M. K. Smit, "Lasing in metal-insulator-metal sub-wavelength plasmonic waveguides," Optics Express **17**, 11,107–11,112 (2009).

[40] M. A. Noginov, G. Zhu, A. M. Belgrave, R. Bakker, V. M. Shalaev, E. E. Narimanov, S. Stout, E. Herz, T. Suteewong, and U. Wiesner, "Demonstration of a spaser-based nanolaser," Nature **460**, 1110–1112 (2009).

[41] R. F. Oulton, V. J. Sorger, T. Zentgraf, R. Ma, C. Gladden, L. Dai, G. Bartal, and X. Zhang, "Plasmon lasers at deep subwavelength scale," Nature **461**, 629–632 (2009).

[42] S. Kwon, J. Kang, C. Seassal, S. Kim, P. Regreny, Y. Lee, C. M. Lieber, and H. Park, "Subwavelength plasmonic lasing from a semiconductor nanodisk with silver nanopan cavity," Nano Letters **10**, 3679–3683 (2010).

[43] R. Ma, R. F. Oulton, V. J. Sorger, G. Bartal, and X. Zhang, "Room-temperature sub-diffraction-limited plasmon laser by total internal reflection," Nat Mater **10**, 110–113 (2011).

[44] A. M. Lakhani, K. Yu, and M. C. Wu, "Lasing in subwavelength semiconductor nanopatches," Semiconductor Science and Technology **26**, 014,013 (2011).

[45] K. Yu, A. Lakhani, and M. C. Wu, "Subwavelength metal-optic semiconductor nanopatch lasers," Optics Express **18**, 8790–8799 (2010).

[46] M. P. Nezhad, A. Simic, O. Bondarenko, B. Slutsky, A. Mizrahi, L. Feng, V. Lomakin, and Y. Fainman, "Room-temperature subwavelength metallo-dielectric lasers," Nat Photon **4**, 395–399 (2010).

[47] A. M. Lakhani, M.-k. Kim, E. K. Lau, and M. C. Wu, "Plasmonic crystal defect nanolaser," Optics Express **19**, 18,237–18,245 (2011).

[48] C. Lu, S. Chang, S. L. Chuang, T. D. Germann, and D. Bimberg, "Metal-cavity surface-emitting microlaser at room temperature," Applied Physics Letters **96**, 251,101 (2010).

[49] K. Ding, Z. Liu, L. Yin, M. Hill, M. Marell, P. van Veldhoven, R. Netzel, and C. Ning, "Room-temperature continuous wave lasing in deep-subwavelength metallic cavities under electrical injection," Physical Review B **85** (2012).

[50] M. Khajavikhan, A. Simic, M. Katz, J. H. Lee, B. Slutsky, A. Mizrahi, V. Lomakin, and Y. Fainman, "Thresholdless nanoscale coaxial lasers," Nature **482**, 204–207 (2012).

[51] M. Kim, S. H. Lee, M. Choi, B. Ahn, N. Park, Y. Lee, and B. Min, "Low-loss surface-plasmonic nanobeam cavities," Optics Express **18**, 11,089–11,096 (2010).

[52] P. B. Johnson and R. W. Christy, "Optical constants of the noble metals," Physical Review B **6**, 4370–4379.

[53] D. F. Palik and D. Edwards, "Handbook of optical constants of solids," Academic Press, New York, 1997) vol **2**, 597 (1985).

[54] M. Staffaroni, J. Conway, S. Vedantam, J. Tang, and E. Yablonovitch, "Circuit analysis in metal-optics," Photonics and Nanostructures-Fundamentals and Applications (2011).

[55] G. Sun, "The intersubband approach to si-based lasers," (2010).

[56] A. Einstein, "On the quantum theory of radiation," Phys. Z **18**, 121128 (1917).

[57] J. Franck and E. G. Dymond, "Elementary processes of photochemical reactions," Trans. Faraday Soc. **21**, 536542 (1926).

[58] "Fluorescence fundamentals | life technologies," http://www.invitrogen.com.

[59] M. L. Cohen and T. K. Bergstresser, "Band structures and pseudopotential form factors for fourteen semiconductors of the diamond and zinc-blende structures," Physical Review **141**, 789796 (1966).

[60] S. Adachi, "Optical dispersion relations for GaP, GaAs, GaSb, InP, InAs, InSb, AlxGa1xAs, and In1xGaxAsyP1y," Journal of Applied Physics **66**, 6030–6040 (1989).

[61] S. Adachi and T. Taguchi, "Optical properties of ZnSe," Physical Review B **43**, 9569–9577 (1991).

[62] S. Adachi, "Optical dispersion relations for si and ge," Journal of Applied Physics **66**, 3224–3231 (1989).

[63] T. Kawashima, H. Yoshikawa, S. Adachi, S. Fuke, and K. Ohtsuka, "Optical properties of hexagonal GaN," Journal of Applied Physics **82**, 3528–3535 (1997).

[64] S. Ninomiya and S. Adachi, "Optical properties of cubic and hexagonal CdSe," Journal of Applied Physics **78**, 4681–4689 (1995).

[65] S. Ninomiya and S. Adachi, "Optical properties of wurtzite CdS," Journal of Applied Physics **78**, 1183–1190 (1995).

[66] J. Conway, *Efficient Optical Coupling to the Nanoscale* (University of California, Los Angeles, 2006).

[67] E. M. Purcell, "Spontaneous emission probabilities at radio frequencies," Physical Review **69**, 681 (1946).

[68] T. Baba, "Photonic crystals and microdisk cavities based on GaInAsP-InP system," IEEE journal of selected topics in quantum electronics **3**, 808830 (1997).

[69] M. Kim, A. M. Lakhani, and M. C. Wu, "Efficient waveguide-coupling of metal-clad nanolaser cavities," Optics Express **19**, 23,504–23,512 (2011).

[70] A. Sarychev, G. Shvets, and V. Shalaev, "Magnetic plasmon resonance," Physical Review E **73** (2006). WOS:000236467700097.

[71] H. T. Miyazaki and Y. Kurokawa, "Controlled plasmon resonance in closed metal/insulator/metal nanocavities," Applied Physics Letters **89**, 211,126 (2006).

[72] "Standing waves and resonance - transmission lines," http://www.opamp-electronics.com/tutorials/standing_waves_and_resonance_2_14_06.htm.

[73] L. E. Kinsler and A. R. Frey, *Fundamentals of acoustics* (Wiley, 1950).

[74] G. Roelkens, L. Liu, D. Liang, R. Jones, A. Fang, B. Koch, and J. Bowers, "III-V/silicon photonics for on-chip and intra-chip optical interconnects," Laser & Photonics Reviews **4**, 751779 (2010).

[75] A. W. Fang, H. Park, O. Cohen, R. Jones, M. J. Paniccia, and J. E. Bowers, "Electrically pumped hybrid AlGaInAs-silicon evanescent laser," Opt. Express **14**, 92039210 (2006).

[76] J. Van Campenhout, P. Rojo Romeo, P. Regreny, C. Seassal, D. Van Thourhout, S. Verstuyft, L. Di Cioccio, J. M. Fedeli, C. Lagahe, and R. Baets, "Electrically pumped InP-based microdisk lasers integrated with a nanophotonic silicon-on-insulator waveguide circuit," Optics Express **15**, 67446749 (2007).

[77] D. Liang, M. Fiorentino, T. Okumura, H. H. Chang, D. T. Spencer, Y. H. Kuo, A. W. Fang, D. Dai, R. G. Beausoleil, and J. E. Bowers, "Electrically-pumped compact hybrid silicon microring lasers for optical interconnects," Optics Express **17**, 20,35520,364 (2009).

[78] J. A. Dionne, L. A. Sweatlock, M. T. Sheldon, A. P. Alivisatos, and H. A. Atwater, "Silicon-Based plasmonics for On-Chip photonics," IEEE Journal of Selected Topics in Quantum Electronics **16**, 295306 (2010).

[79] C. Seassal, C. Monat, J. Mouette, E. Touraille, B. Bakir, H. Hattori, J. Leclercq, X. Letartre, P. Rojo-Romeo, and P. Viktorovitch, "InP bonded membrane photonics components and circuits: toward 2.5 dimensional micro-nano-photonics," Selected Topics in Quantum Electronics, IEEE Journal of **11**, 395 – 407 (2005).

[80] E. Yablonovitch, "Inhibited spontaneous emission in solid-state physics and electronics," Physical review letters **58**, 20592062 (1987).

[81] T. Okamoto, F. HDhili, and S. Kawata, "Towards plasmonic band gap laser," Applied Physics Letters **85**, 3968 (2004).

[82] C. Jeppesen, N. A. Mortensen, and A. Kristensen, "The effect of ti and ITO adhesion layers on gold split-ring resonators," Applied Physics Letters **97**, 263,103 (2010).

[83] M. Boroditsky, I. Gontijo, M. Jackson, R. Vrijen, E. Yablonovitch, T. Krauss, C. C. Cheng, A. Scherer, R. Bhat, and M. Krames, "Surface recombination measurements on IIIV candidate materials for nanostructure light-emitting diodes," Journal of Applied Physics **87**, 3497 (2000).

[84] W. Henschel, Y. M. Georgiev, and H. Kurz, "Study of a high contrast process for hydrogen silsesquioxane as a negative tone electron beam resist," Journal of Vacuum Science & Technology B: Microelectronics and Nanometer Structures **21**, 2018 (2003).

[85] G. C. DeSalvo, C. A. Bozada, J. L. Ebel, D. C. Look, J. P. Barrette, C. L. A. Cerny, R. W. Dettmer, J. K. Gillespie, C. K. Havasy, T. J. Jenkins, K. Nakano, C. I. Pettiford, T. K. Quach, J. S. Sewell, and G. D. Via, "Wet chemical digital etching of GaAs at room temperature," Journal of The Electrochemical Society **143**, 3652–3656 (1996).

[86] D. Pozar, "Radiation and scattering from a microstrip patch on a uniaxial substrate," Antennas and Propagation, IEEE Transactions on **35**, 613 – 621 (1987).

[87] K. Carver and J. Mink, "Microstrip antenna technology," IEEE TRANSACTIONS ON ANTENNAS AND PROPAGATION **29**, 2–24 (1981).

[88] C. Manolatou and F. Rana, "Subwavelength nanopatch cavities for semiconductor plasmon lasers," IEEE J. Quantum Electron **44**, 435447 (2008).

[89] S. B. Cohn, "Microwave bandpass filters containing high-Q dielectric resonators," Microwave Theory and Techniques, IEEE Transactions on **16**, 218227 (1968).

[90] D. Kajfez and P. Guillon, "Dielectric resonators," (1986).

[91] J. Zenneck, "ber die fortpflanzung ebener elektromagnetischer wellen lngs einer ebenen leiterflche und ihre beziehung zur drahtlosen telegraphie," Annalen der Physik **328**, 846866 (1907).

[92] A. Sommerfeld, "ber die ausbreitung der wellen in der drahtlosen telegraphie," Annalen der Physik **333**, 665736 (1909).

[93] Z. H. Zhu, H. Liu, S. M. Wang, T. Li, J. X. Cao, W. M. Ye, X. D. Yuan, and S. N. Zhu, "Optically pumped nanolaser based on two magnetic plasmon resonance modes," Applied Physics Letters **94**, 103,106 (2009).

[94] M. Oxborrow, "Traceable 2-d finite-element simulation of the whispering-gallery modes of axisymmetric electromagnetic resonators," IEEE Transactions on Microwave Theory and Techniques **55**, 1209 (2007).

[95] A. Farjadpour, D. Roundy, A. Rodriguez, M. Ibanescu, P. Bermel, J. D. Joannopoulos, S. G. Johnson, and G. W. Burr, "Improving accuracy by subpixel smoothing in the finite-difference time domain," Optics letters **31**, 29722974 (2006).

[96] K. Nozaki, S. Kita, and T. Baba, "Room temperature continuous wave operation and controlled spontaneous emission in ultrasmall photonic crystal nanolaser," Optics Express **15**, 7506–7514 (2007).

[97] J. P. Berenger, "A perfectly matched layer for the absorption of electromagnetic waves," Journal of computational physics **114**, 185200 (1994).

[98] H. Y. Ryu, M. Notomi, E. Kuramoti, and T. Segawa, "Large spontaneous emission factor ([greater-than] 0.1) in the photonic crystal monopole-mode laser," Applied Physics Letters **84**, 1067–1069 (2004).

[99] B. Min, E. Ostby, V. Sorger, E. Ulin-Avila, L. Yang, X. Zhang, and K. Vahala, "High-Q surface-plasmon-polariton whispering-gallery microcavity," Nature **457**, 455–458 (2009).

[100] A. Mizrahi, V. Lomakin, B. A. Slutsky, M. P. Nezhad, L. Feng, and Y. Fainman, "Low threshold gain metal coated laser nanoresonators," Optics letters **33**, 12611263 (2008).

[101] F. Wang and Y. R. Shen, "General properties of local plasmons in metal nanostructures," Physical Review Letters **97** (2006).

[102] J. C. Ho, A. C. Ford, Y. Chueh, P. W. Leu, O. Ergen, K. Takei, G. Smith, P. Majhi, J. Bennett, and A. Javey, "Nanoscale doping of InAs via sulfur monolayers," Applied Physics Letters **95**, 072,108–3 (2009).

[103] cyclotene, "CYCLOTENE advanced electronics resins - product literature," http://www.dow.com/cyclotene/resource/prodlit.htm.